BOUNDARY LAYER FLOWS INDUCED BY THE MOTION OF ROUGH SURFACES

JASON FERGUSON

Doctor of Philosophy in Engineering & Physical Sciences

ASTON UNIVERSITY

December 2024

Abstract

We consider the linear stability of steady boundary layer flows induced by the translation of a moving wavy surface of infinite length. The wavy surface has a sinusoidal profile and is considered here as a model for surface roughness. Previous studies have used similar surface roughness models when analysing roughness effects on three-dimensional axisymmetric boundary-layer flows. In these instances, surface roughness has been shown to stabilise convective modes of instability. The motivation for this study is to ascertain if qualitatively similar results are predicted for two-dimensional boundary-layer flows where Tollmien–Schlichting waves are the dominant mode of instability. Combining results from two separate numerical analyses with a large Reynolds number asymptotic analysis we show that these types of flow configurations are indeed stabilised by the presence of surface roughness. We validate our numerical analyses by employing an alternative approach, where the modified mean flow is determined by solving the Reynolds-averaged boundary layer equations. Once again, our results demonstrate that these types of flow configurations are stabilised by the presence of surface roughness.

Key words: Newtonian, boundary-layer, rough surface flow, linear instability

Acknowledgements

I would first like to express my gratitude to Dr. Paul Griffiths for his invaluable advice, guidance, and continuous support throughout my studies. I am deeply indebted to him for giving me the opportunity to pursue my PhD. I also extend my thanks to Dr. Philip Trevelyan for his advice and guidance during the final stages of my research. Additionally, I wish to acknowledge Dr. Sharon Stephen for the many insightful discussions related to this work, as well as Dr. Liam Escott and Mr. Niall Hanevy for their valuable insights and support throughout my studies.

I am deeply grateful for the unwavering support of my parents, and especially my grandad, whose encouragement has been instrumental in helping me reach where I am today. Finally, I want to express my heartfelt thanks to my partner, Vanessa Hull, whose presence made my years as a PhD student so much more enjoyable.

Contents

Chapter 1

Introduction

1.1 Motivation

The aim of this study is to add to the growing body of literature focusing on small amplitude roughness effects in steady boundary layer flows. Our focus will be on the development of Tollmien-Schlichting (TS) waves in two-dimensional flows with the goal being to establish if and how periodic roughness affects the known mechanisms for the onset of linear instability. The long-held view that surface roughness *always* acts to increase skin-friction drag has been shown to be a misnomer (Carpenter (1997); Choi (2006)) and, as such, researchers in recent years have invested a great deal of effort into the determination of roughness-based drag reduction strategies. Indeed, there is a growing community of researchers exploring the utilisation of surface roughness to reduce the high shear stresses encountered in turbulent boundary layers (see, for example, Cardillo *et al.* (2013), and Wu & Piomelli (2018)). However, the focus of this study is on the role surface roughness plays in the laminar to turbulent transition process. With this objective in mind, we will analyse the linear stability of a boundary layer flow generated by the motion of a rough surface.

1.2 Basic Flow Solutions

The boundary layer, first hypothesized by Prandtl (1905), is a thin region adjacent to a surface where fluid (like air or water) is in contact with the surface and exhibits distinctive flow behaviour due to viscosity. The interaction between the surface and the fluid induces a no-slip boundary condition where the velocity is zero at the surface. The flow velocity then monotonically increases above the surface until it returns to the bulk flow velocity. The thin layer consisting of fluid whose velocity has not yet returned to the bulk flow velocity is called the boundary layer. By using an order of magnitude analysis Prandtl was able to simplify the Navier-Stokes equations to what are now known as the boundary layer equations. Blasius (1907) examined the boundary layer that forms on a semi-infinite plate which is held parallel to a constant unidirectional flow. He was able to solve the boundary layer equations and obtained a self-similar solution. He was able to convert the governing partial differential equations into a third-order ordinary differential equation which is referred to as the 'Blasius equation'.

The boundary layer that develops on a continuously moving surface—such as a flat belt, conveyor, or extruding sheet—was first investigated by Sakiadis in his pioneering work (Sakiadis (1961*a*), Sakiadis (1961*b*)). This flow configuration, now widely known as 'Sakiadis flow', has numerous practical applications, including the aerodynamic extrusion of plastic sheets and the cooling of an infinitely extending metallic plate in a cooling bath. A schematic representation of this flow is provided in Figure 1 of Sakiadis (1961*b*), illustrating a continuously moving plane sheet emerging from a slot and advancing steadily through a quiescent fluid. Due to viscosity, Sakiadis demonstrated that the boundary layer thickness increases along the direction of motion. Additionally, the velocity component perpendicular to the plate is negative, indicating fluid entrainment from the surrounding medium into the boundary layer. By applying an appropriate transformation to the governing boundary-layer equations, Sakiadis derived the classical Blasius (1907) equation. However, the boundary conditions in Sakiadis flow differ fundamentally from those in Blasius flow. In the former, an infinitely extending surface emerges from a slot and moves at a constant velocity through a stationary fluid, whereas in the latter, a fixed surface is subjected to an oncoming unidirectional stream. This fundamental distinction prevents the two flows from being mathematically transformed into one another, as further demonstrated by Abdelhafez (1985). Moreover, Sakiadis showed that the skin friction coefficient for a continuously moving surface is approximately 30% higher than that in Blasius flow, underscoring the unique characteristics of this boundary-layer phenomenon. In fact, Sakiadis explicitly highlights the key differences between these two flow configurations in his works (Sakiadis (1961*a*), Sakiadis (1961*b*)). In this thesis, we focus on the boundary layer that develops on an infinitely extending moving surface, with particular attention to the effects of surface roughness.

Tsou *et al.* (1967) later extended the work of Sakiadis (1961*b*) by conducting both an analytical and experimental study of the velocity and temperature fields for the flow that forms on a continuously moving surface. The authors were able to derive the basic flow solutions for the boundary layer that formed on a continuous moving surface which agreed with the results presented by Sakiadis (1961*b*). Tsou *et al.* (1967) also obtained solutions for the temperature distribution by solving the boundary layer energy equations and considered two cases. In the first instance, the authors considered a uniform wall temperature and observed a sharp decrease in the thermal boundary layer thickness with increasing Prandtl number, where the Prandtl number is defined as the ratio of momentum diffusivity to thermal diffusivity. They also determined the thermal boundary layer to be thinner than the velocity boundary layer when the Prandtl number was large. For the second case, Tsou *et al.* (1967) considered a uniform wall heat flux and obtained similar results.

In the experimental work conducted by Tsou *et al.* (1967), measurements of the laminar velocity field were obtained (see Figure 1.1). These measurements showed good agreement with their analytical predictions. Consequently, Tsou *et al.* (1967) were able to verify Sakiadis' theoretical results experimentally and demonstrate that this type of flow is physically realiz-

F. K. TSOU, E. M. SPARROW and R. J. GOLDSTEIN

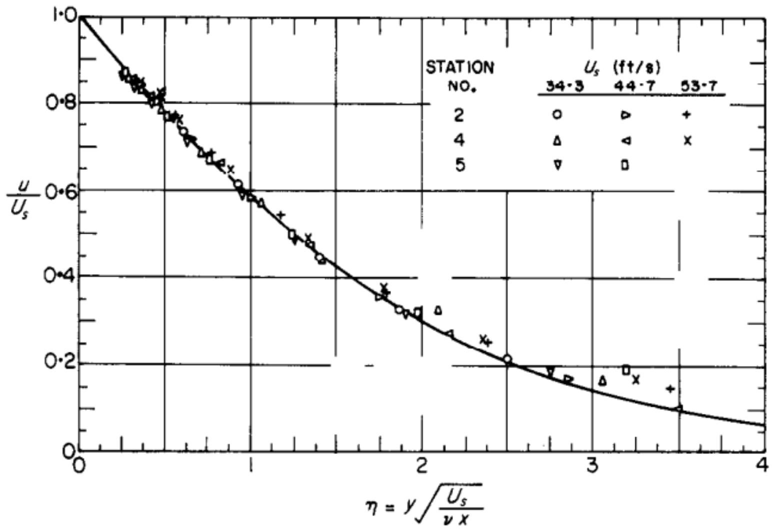

FIG. 6. Comparison of experimental and analytical laminar velocity profiles.

Figure 1.1: Experimental results for the continuous moving surface taken from Tsou *et al.* (1967)

.

able. More recently, Hattori (2023) conducted numerical simulations of the boundary layer that forms over a continuously moving surface using OpenFOAM. Their results showed strong agreement with the theoretical predictions of Sakiadis (1961*b*), except near the leading edge, where the boundary layer approximation is no longer valid. This discrepancy arises because the boundary layer approximation assumes the presence of a thin viscous layer near the moving surface, where viscosity is significant. However, at the leading edge—where the semi-infinite sheet first emerges from the slot—the flow has not yet had sufficient time or distance to develop into a thin boundary layer. In fact, when deriving the boundary layer equations, Prandtl (1905) assumed that the streamwise velocity component is significantly greater than the velocity component perpendicular to the surface. However, as demonstrated by Hattori (2023), both velocity components are of comparable magnitude near the leading edge, violating a fundamental assumption of boundary layer theory. Despite this, Hattori (2023) showed that at a suitable distance downstream from the leading edge, results from direct numerical simulations closely align with theoretical predictions, confirming the validity of the boundary layer approximation in the fully developed region.

In addition to these studies, Erickson *et al.* (1966) studied both the heat and mass transfer on a continuous moving surface with the addition of injection and investigated the thermal and concentration boundary layers in the case of constant temperature and concentration at the surface. The authors obtained numerical solutions for the boundary layer momentum, energy, and diffusion equations across a wide range of injection rates. These solutions were evaluated for Prandtl and Schmidt numbers of 1, 10, and 100, where the Schmidt number represents the ratio of momentum diffusivity to mass diffusivity. The authors observed a decrease in the thermal boundary layer thickness with increasing Prandtl number, consistent with the findings of Tsou *et al.* (1967). For a Prandtl number of unity, they demonstrated that the thermal boundary layer coincides with the momentum boundary layer. However, for Prandtl numbers greater than 1, the thermal boundary layer was found to be contained within the momentum boundary layer. Erickson *et al.* (1966) demonstrated that for small injection rates, both the local heat transfer coefficient and the local mass transfer coefficient increase with increasing Prandtl or Schmidt numbers. However, for large injection rates, the trend reverses, showing a rapid decrease in these coefficients with increasing Prandtl or Schmidt numbers.

Soundalgekar & Ramana Murty (1980) investigated heat transfer in the flow past a continuously moving surface with a variable temperature profile, where the temperature varies with the streamwise coordinate as Ax^n. Here, A is a constant, and x is the distance from the leading edge of the plate. By applying an appropriate transformation to the governing equations, they derived similarity solutions. Their analysis concluded that increasing the Prandtl number or the exponent n results in an increase in the Nusselt number. The Nusselt number, a dimensionless measure, represents the ratio of convective to conductive heat transfer across the boundary layer.

Soundalgekar & Murty (1989) extended this investigation by examining the effects of viscous dissipation on heat transfer over a continuously moving surface. They derived self-similar solutions and solved the resulting equations numerically. Their findings indicated that increased viscous dissipation leads to a rise in the fluid temperature and a corresponding decrease in the rate of heat transfer. Several other studies have further increased the complexity of this problem by incorporating the effects of variable viscosity (see Pop *et al.* (1992), Soundalgekar *et al.* (2004), Elbashbeshy & Bazid (2004)) and radiation effects as per Ishak *et al.* (2011).

The determination of basic flow states induced by the translation of a moving wavy surface has been considered a number of times. Of particular note is the study of Rees & Pop (1995) who focus their attention on heated wavy surfaces, determining the streamwise development of both the skin friction and local rate of heat transfer. Their results were determined using a suitably adapted Keller-Box scheme. The authors analysed two cases: one with a constant wall temperature (CWT) and the other with a prescribed constant heat flux (CHF). Rees & Pop (1995) found that an increase in wave amplitude results in a decrease in both the skin friction coefficient and the Nusselt number for both CWT and CHF conditions. Additionally, the skin friction was observed to vary periodically in space. They also observed that both the local rate of heat transfer and wall temperature increase with rising wave amplitude. Furthermore, these quantities exhibit a periodic component that decays over time. In the constant wall temperature (CWT) case, the decay is slow, while in the constant heat flux (CHF) case, the decay occurs more rapidly.

Hossain & Pop (1996) studied the boundary layer flow over a moving wavy surface in the presence of an electrically conducting fluid subjected to a constant transverse magnetic field. Their investigation focused on the combined effects of surface waviness and magnetohydrodynamics (MHD) on the flow and heat transfer characteristics. The authors conducted a similar analysis to that of Rees & Pop (1995). However, the governing equations in their study differed due to the presence of an electrically conducting fluid influenced by a constant transverse magnetic field. Focusing on a Prandtl number of 0.7, they obtained both the velocity and temperature profiles using an implicit finite-difference method coupled with the Keller-box elimination technique.

The authors analysed the effect of the magnetic field parameter—a dimensionless measure of the strength of the applied transverse magnetic field, where higher values indicate stronger magnetic effects—at two streamwise locations: the trough and the crest positions. Since the behaviour of the profiles at these locations is similar, results were presented for both positions to illustrate the overall trends. It was observed that both the velocity and temperature profiles increase with an increase in the magnetic field parameter M. However, for small wave amplitudes and in the absence of a magnetic field, the velocity and temperature profiles at both the trough and crest positions are nearly identical. But for larger wave amplitudes, such as $a = 0.5$, there is a significant difference in the velocity and temperature profiles between the trough and crest positions when $M = 0$. Additionally, as the wave amplitude increases, the velocity profiles decrease due to the enhanced undulations of the wavy surface, which introduce greater surface resistance and disrupt the smooth flow of the fluid. These undulations cause an increase in drag effectively slowing down the fluid motion near the surface. In contrast, the temperature profiles increase because the disturbed flow promotes greater mixing and thermal convection, enhancing the heat transfer process. The authors proceeded by presenting the variations of the wave amplitude, the magnetic field parameter, and the streamwise coordinate for both the skin friction coefficient and the local Nusselt number. They observed that these quantities exhibit periodic variation along the streamwise direction. Additionally, the skin friction coefficient was found to be less than or equal to that of a flat plate, which can be attributed to the effects of the surface waviness and the presence of the magnetic field.

The boundary layer that forms on a continuous moving wavy surface has also been investigated in the context of entropy generation as per Mehmood *et al.* (2019*a*). This study shows how factors such as surface waviness, fluid viscosity, heat transfer, and the presence of a magnetic field influence the rate of entropy production within the boundary layer. Entropy generation is crucial for assessing the thermodynamic efficiency of such systems, where surface irregularities and external forces like magnetic fields can affect irreversibilities due to heat transfer and fluid friction.

1.3 Linear Stability

The purpose of this research is to investigate the stability characteristics of a continuously moving surface with the addition of surface roughness. Our findings aim to enhance the broader understanding of hydrodynamic stability in Newtonian fluids, especially in situations where surface irregularities affect flow behaviour and stability. The theory of hydrodynamic stability is a fundamental area of fluid mechanics, with classical problems first identified by Reynolds, Rayleigh, Kelvin, and Helmholtz toward the end of the 19th century. These classical problems are extensively covered in various introductory textbooks; for example, Drazin & Reid (2004).

Hydrodynamic stability theory predicts if and when a specific flow configuration will transition from a laminar to a turbulent state. It also describes how the flow evolves through the transition region, providing insight into the mechanisms that trigger instability and the subsequent development of turbulence. In most applications, laminar flows are preferable because they result in less energy loss due to friction. In contrast, turbulent flows lead to greater energy consumption, reduced efficiency, and higher operational costs. However, turbulence can be beneficial in specific engineering systems, such as combustion processes. In these cases, turbulence enhances the mixing of fuel and air, which increases the reaction rate per unit volume, thereby improving the efficiency and performance of combustors.

The first person to study the stability of fluid flow was Reynolds (1883). He conducted a series of experiments involving fluid flow through pipes to investigate this phenomenon. Reynolds analysed the behaviour of dye streaks in the fluid as it flowed through three different pipes at varying velocities. This allowed him to identify the conditions under which the flow transitioned from laminar to turbulent, laying the foundation for the theory of hydrodynamic stability. In the case of laminar flow, Reynolds observed that the dye streaks extended in a straight line through the tube, indicating smooth and orderly fluid motion. In the second case, corresponding to turbulent flow, the dye mixed chaotically with the fluid. To study this turbulent scenario in greater detail, Reynolds used an electric spark to illuminate the fluid, revealing the dye as a mass of curls and eddies during the transition to turbulence. This visualization provided key insights into the chaotic nature of turbulent flow and the process of transition from laminar to turbulent states.

Through these experiments, Reynolds demonstrated that the stability characteristics of fluid flow depend on three key quantities: V, the velocity of the fluid; r, the radius of the pipe; and ν, the kinematic viscosity of the fluid. His most significant finding was that laminar flow began to break down when the ratio Vr/ν exceeded a certain threshold. This ratio is now known as the Reynolds number Re, a dimensionless quantity that characterises the nature of the flow. 'Reynolds' work introduced the concept of a critical Reynolds number Re_{crit}, representing the threshold beyond which the flow transitions from a laminar to a turbulent state. Stability analysis can be broadly categorised into various types, including linear or non-linear analysis, and local or global analysis. To fully understand the stability characteristics of a particular flow configuration, it is essential to consider all these methods.

Linear Stability Analysis (LSA) is typically the first approach used and serves as a starting point for understanding the stability of complex flows. Linear theory predicts the behaviour of small disturbances, while weakly non-linear theory extends this by predicting the subsequent stages of disturbance evolution when the growth rates are small but not infinitesimal.

In local analyses, disturbances are separated into Fourier-type traveling waves, allowing for the examination of instability mechanisms at specific locations within the flow. In contrast, global analyses involves time-dependent simulations of the full Navier-Stokes equations, capturing the overall flow behaviour and interactions between disturbances throughout the entire domain. This combined approach provides a comprehensive understanding of the flow stability and the transition to turbulence. To analyse the stability characteristics of a continuously moving wavy surface, we perform a linear stability analysis. In this method, we examine the evolution of small perturbations superimposed on a two-dimensional parallel basic flow. This approach allows us to determine how these small disturbances grow or decay, providing insight into the stability characteristics of the flow configuration and identifying conditions that may lead to instability and transition to turbulence.

The parallel-flow approximation has been widely used in theoretical studies of flow stability. This approximation assumes that the basic flow profile does not change in the streamwise direction, simplifying the analysis by reducing the complexity of the governing equations. While it may not capture all aspects of real-world flow configurations, the parallel-flow approximation provides valuable insights into the fundamental mechanisms of an instability and serves as a useful starting point for understanding the transition from laminar to turbulent flow. Tollmien (1930) and Schlichting (1933) utilised the parallel-flow approximation to analyse the Blasius boundary layer. In this context, the boundary layer flow can be considered an effective approximation of parallel flow because the variation of the main flow in the streamwise direction is much smaller than its variation in the wall-normal direction. Using this approach, the partial differential equations governing small disturbances to the basic flow can be simplified to an ordinary differential equation. This reduction is achieved by assuming a normal mode solution in the form of traveling waves, known as Tollmien-Schlichting (TS) waves. These waves represent the primary instability mechanism in boundary layer flows, playing a crucial role in the transition from laminar to turbulent flow.

The resulting ordinary differential equation derived from the parallel-flow approximation is known as the Orr-Sommerfeld equation, independently attributed to Orr (1907) and Sommerfield (1908). The Orr-Sommerfeld equation is central to the theory of flow stability because analysing its eigenvalues for a given Reynolds number provides critical insights into the linear stability properties of the flow. Specifically, the nature of the eigenvalues helps determine whether small disturbances will grow or decay, indicating whether the flow remains stable or transitions toward turbulence.

Tollmien (1930) and Schlichting (1933) used the parallel-flow approximation along with approximate solutions of the Orr-Sommerfeld equation to theoretically establish the linear stability characteristics of the Blasius boundary layer. They demonstrated that the flow becomes linearly unstable above a critical Reynolds number of $Re_{\text{crit}} = 520$. The experimental work of Schubauer & Skramstad (1948) provided empirical evidence supporting the theoretical predictions made by Tollmien and Schlichting. Their experiments confirmed the existence of an instability and the transition to turbulence at Reynolds numbers consistent with the theoretical findings.

The first to investigate the linear stability of the boundary layer formed on a continuous moving surface were Tsou *et al.* (1966). In this pioneering study the authors showed these flows are susceptible to Tollmien–Schlichting (TS) waves but that the onset of linear instability occurs at a much higher Reynolds number when compared to, for example a traditional Blasius boundary layer. Tsou *et al.* (1966) argue that these findings are connected with the fact that the transverse velocity in the main flow is inward for the continuous surface problem and outward for the Blasius boundary layer. It is believed that the effect of the inflow is to move the disturbances nearer to the wall where they are more readily damped. Using a similar approach to that of Tsou *et al.* (1966), Watanabe *et al.* (1995) analysed the linear stability of an electrically conducting fluid in the presence of a transverse magnetic field. Their study demonstrated that an increase in the magnetic parameter leads to an increase in the critical Reynolds number. This indicates that the magnetic field has a stabilising effect on the flow, delaying the onset of instability and the transition from laminar to turbulent flow.

The linear stability characteristics of boundary layer flows induced by the translation of a rough surface have not been systematically analysed. To that end, the focus of this thesis will be to consider the linear stability characteristics of boundary layer flows induced by the translation of a rough surface. The study of this two-dimensional flow is similar in some sense, to the three-dimensional rotating disk flow studies conducted by Cooper *et al.* (2015) and Garrett *et al.* (2016). Having said that the convective mode of instability that dominates in these rotational flows is different in nature to the TS waves that one expects to encounter in flat plate boundary layer flows. Although the linear stability characteristics of boundary layer flows induced by the translation of rough surfaces have not been systematically analysed, a number of previous studies have reported on the linear stability associated with boundary-layer flows that are generated by an external free stream interacting with a fixed plate.

Levchenko & Solov'ev (1972) predicted that small amplitude surface waviness reduces the critical Reynolds number for the onset of linear instability when compared to the Blasius boundary layer result. In order to arrive at this conclusion the authors employed a 'frozen flow' methodology whereby snapshots of the spatially periodic flow were analysed using an approach adopted from Floquet theory. We will employ similar approaches in this thesis in order to analyse our base flows which we find also to vary periodically in space. The findings of Levchenko & Solov'ev (1972) were then qualitatively supported by the experimental study of Kachanov *et al.* (1974) who showed that the growth of the TS waves increases with increasing surface waviness.

In addition to these studies Lessen & Gangwani (1976) applied a suitable averaging procedure, over one streamwise wavelength of a small amplitude roughness profile, to show, using parallel flow theory, that these types of periodic roughness profiles do indeed result in a prediction for the destabilisation of boundary layer flows generated by an oncoming free stream. Applying similar methods to that of Lessen & Gangwani (1976), Gaster (2016) observed increased amplification rates of the T-S waves with increasing levels of roughness.

These findings of boundary layer destabilisation due to surface roughness effects are in direct contrast to the results presented by Cooper *et al.* (2015) and Garrett *et al.* (2016). In these studies the authors show how the type I mode, a mode associated with convective instability is significantly stabilised in the presence of small amplitude surface waviness. Cooper *et al.* (2015) arrive at this conclusion having applied, to the calculation of the base flow quantities only, partial slip boundary conditions at the wall to mimic the effects of surface roughness. These findings were then supported by the results presented by Garrett *et al.* (2016) who, having directly accounted for the surface variation in the derivation of their governing equations, then go on to employ an averaging technique, not to dissimilar to that of Lessen & Gangwani (1976), to analyse the linear stability characteristics of these flow profiles. More recently Thomas *et al.* (2023) revisited the problem first considered by Cooper *et al.* (2015). In this study the authors presented an argument for the adoption of the partial slip boundary conditions to be applied to the calculation of both base flow and perturbation quantities. The conclusion that periodic small amplitude roughness proves to be a stabilising feature remains the case when one considers isotropic roughness (a combination of partial-slip in both the radial and azimuthal directions). However, the predicted boundary layer stabilisation was significantly reduced when compared to the findings of Cooper *et al.* (2015). Furthermore, in the presence of purely radial partial-slip, the type I mode is instead predicted to be destabilised, a result opposed to the original findings of Garrett *et al.* (2016). In addition to these studies Morgan & Davies (2020*a*) and Morgan *et al.* (2021*a*) studied the control of stationary convective instabilities in the rotating disk boundary layer via a time-periodic modulation of the disk rotation rate by employing a technique not to dissimilar to that of Levchenko & Solov'ev (1972). The nature of this problem led the authors to arrive at base flow solutions that were periodic in time. The standard practice when one determines base flow solutions in this form is to conduct a Floquet analysis in order to determine the linear stability characteristics of the system. Morgan *et al.* (2021*a*) do this successfully, and, importantly for our study, show that the results owing from such an analysis can be very well approximated by a quasi-steady approach. In essence, they find that by conducting a standard LSA at numerous instances in time over one periodic cycle of the base flow, the equivalent Floquet theory result can be almost exactly reproduced simply by taking an average of these distinct eigenvalue calculations. The relationship between the quasi-steady approach and Floquet theory is well explained by Luo & Wu (2010) in their study of the Stokes layer. This approach is sometimes referred to as a 'frozen flow' analysis as one essentially freezes the flow in time, removing the time dependence from the problem, allowing for steady LSA approaches to be employed. Motivated by the above findings our aim is to add to the growing body of literature focusing on small amplitude roughness effects in steady boundary layer flows.

1.4 Thesis Outline

The objective of this thesis is to analyse how sinusoidal surface roughness influences the onset of linear instability for a specific class of boundary-layer flows, those induced by translation. By using both numerical and asymptotic approaches, we aim to determine if surface roughness could be exploited for flow control purposes.

In Chapter 2, we formulate the problem by accounting for variations in the wall's surface. We proceed by introducing a set of transformations that leads to a parabolic partial differential equation. Finally, we derive a Keller-Box scheme which allows us to solve the resulting PDE numerically. In Chapter 3 we derive the basic flow solutions and analyse the results in the context of other studies that have considered sinusoidal wall profiles. We start by considering the translation of a smooth surface before proceeding to analyse the effect surface waviness has on the basic flow. By exploiting the parabolic nature of the governing equations and utilising the Keller-Box method we find that the basic flow is periodic in space provided we are sufficiently far enough downstream of the leading edge. A suitable averaging procedure is adopted that removes all dependence of the streamwise coordinate. Finally, we verify our Keller-Box solutions by adopting a suitable similarity approach.

In Chapter 4 we analyse the linear stability of the averaged flow solutions numerically via two different means. In the first instance, we adopt the standard Orr-Sommerfeld approach twinned with an integral energy analysis. For the second approach, we conduct what we term a ‘quasi-spatial’ linear stability analysis and compare the two methodologies. In Chapter 5 we attempt to verify our numerical solutions by conducting a large Reynolds number analysis and solve the resulting eigenrelation for flows of this type. In Chapter 6 we conclude by seeking an alternative method for analysing the onset of linear instability for boundary layer flows induced by the translation of a wavy surface. By solving the steady Orr-Sommerfeld equation subject to inhomogeneous boundary conditions, we use the information obtained from the solution to evaluate the Reynolds stress, which in turn modifies the mean flow. We proceed by adopting the Orr-Sommerfeld approach to analyse the growth rates for two specific cases. First we consider the boundary-layer induced by an external oncoming flow and we conclude the chapter by considering the flow induced by a translating surface. In Chapter 7, we summarise our findings and propose extensions to our analysis that incorporate surface roughness, offering a closer representation of surfaces encountered in natural environments or industrial applications. We conclude by exploring alternative methods for analysing the onset of linear instability. Finally, we briefly discuss potential modifications to the problem, including the incorporation of an external oncoming flow or a reverse free stream.

Chapter 2

The Governing Equations

In this chapter we formulate the problem and describe the governing equations that describe boundary layer flows over non-flat surfaces. We start by considering the two-dimensional continuity and Navier-Stokes momentum equations. To account for the variation in the wall's surface we make use of Prandtl's transposition theorem, for details, see Yao (1988). Essentially a change of coordinate system is introduced which leads to a more complex form of the two-dimensional continuity and Navier-Stokes momentum equations. The problem is then non-dimensionalised and we introduce the boundary layer scalings which leads to the equations that govern boundary layer flows over non-flat surfaces. Lastly we apply a further transformation that leads to a parabolic partial differential equation that we solve numerically using a Keller-Box scheme. However, as we will show in Section §3.4, these solutions can been determined via a suitable similarity solution approach.

2.1 Problem Formulation

To derive the governing boundary layer equations, we follow a similar analysis to that outlined by Hanevy *et al.* (2024). We begin by considering the flow of an incompressible Newtonian fluid, over an impermeable, semi-infinite continuous moving wavy surface in an otherwise quiescent fluid in the absence of body forces. The flow is governed by the continuity and the two-dimensional Navier-Stokes momentum equations

$$\frac{\partial u^*}{\partial x^*}+\frac{\partial v^*}{\partial y^*}=0, \tag{2.1.1a}$$
$$\frac{\partial u^*}{\partial t^*}+u^*\frac{\partial u^*}{\partial x^*}+v^*\frac{\partial u^*}{\partial y^*}=-\frac{1}{\rho^*}\frac{\partial p^*}{\partial x^*}+\nu^*\left(\frac{\partial^2 u^*}{\partial x^{*2}}+\frac{\partial^2 u^*}{\partial y^{*2}}\right), \tag{2.1.1b}$$
$$\frac{\partial v^*}{\partial t^*}+u^*\frac{\partial v^*}{\partial x^*}+v^*\frac{\partial v^*}{\partial y^*}=-\frac{1}{\rho^*}\frac{\partial p^*}{\partial y^*}+\nu^*\left(\frac{\partial^2 v^*}{\partial x^{*2}}+\frac{\partial^2 v^*}{\partial y^{*2}}\right), \tag{2.1.1c}$$

where * indicates a dimensional quantity, time is denoted by t^*, the fluid density is ρ^*, the pressure is p^*, the kinematic viscosity is ν^*, and u^*, and v^* are the velocity components in the streamwise (x^*) and wall-normal (y^*) directions, respectively.

System (2.1.1) is solved subject to the wall conditions $(u^*,v^*)\cdot\hat{\mathbf{n}}=0$, and $(u^*,v^*)\cdot\hat{\mathbf{t}}=U_w^*$, where $\hat{\mathbf{n}}$ and $\hat{\mathbf{t}}$ are the unit normal and tangent vectors to the wavy surface, respectively, and U_w^* is the dimensional wall speed.

To describe the steady flow over a surface exhibiting variable curvature, it proves useful to introduce the following transformation

$$X^*=x^*, \tag{2.1.2a}$$
$$Y^*=y^*-s^*(x^*), \tag{2.1.2b}$$

where Y^* represents the vertical distance above the variable surface at a given streamwise location x^*. In this study, in a similar fashion to Garrett *et al.* (2016), we consider the variation of the rough surface to be described as follows

$$s^*(x^*)=A^*\cos\left(\frac{2\pi x^*}{\gamma^*}\right), \tag{2.1.3}$$

where the quantity A^* represents the amplitude of the wavy surface, and γ^* is the wavelength of

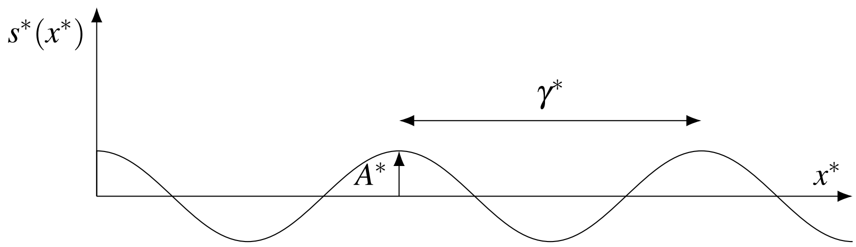

Figure 2.1: Schematic diagram depicting the variation of the periodic rough surface, $s^*(x^*)$, as a function of the streamwise coordinate.

the surface variation, this profile is depicted schematically in Figure 2.1.

For a single valued surface of height s^*, the unit normal $\hat{\mathbf{n}}$, is uniquely defined by $\hat{\mathbf{n}} = \mathbf{n}/|\mathbf{n}|$ where

$$\mathbf{n} = \nabla Y^* = (-(s^*)'_{X^*}, 1), \tag{2.1.4}$$

where the $'$ indicates differentiation with respect to the subscript variable. The unit tangent vector $\hat{\mathbf{t}}$ is given by $\hat{\mathbf{t}} = \mathbf{t}/|\mathbf{t}|$ where $\mathbf{t} = (1, (s^*)'_{X^*})$. Using (2.1.2) we obtain the following differential operators

$$\begin{aligned}
\frac{\partial}{\partial x^*} &= \frac{\partial}{\partial X^*} - (s^*)'_{X^*}\frac{\partial}{\partial Y^*},\\
\frac{\partial^2}{\partial x^{*2}} &= \frac{\partial^2}{\partial X^{*2}} - (s^*)''_{X^*X^*}\frac{\partial}{\partial Y^*} - 2(s^*)'_{X^*}\frac{\partial^2}{\partial X^*\partial Y^*} + [(s^*)'_{X^*}]^2\frac{\partial^2}{\partial Y^{*2}},\\
\frac{\partial}{\partial y^*} &= \frac{\partial}{\partial Y^*},\\
\frac{\partial^2}{\partial y^{*2}} &= \frac{\partial^2}{\partial Y^{*2}}.
\end{aligned}$$

Applying the differential operators to (2.1.1) yields the following

$$\frac{\partial u^*}{\partial X^*} - (s^*)'_{X^*}\frac{\partial u^*}{\partial Y^*} + \frac{\partial v^*}{\partial Y^*} = 0, \tag{2.1.6a}$$

$$u^*\frac{\partial u^*}{\partial X^*} - u^*(s^*)'_{X^*}\frac{\partial u^*}{\partial Y^*} + v^*\frac{\partial u^*}{\partial Y^*} = -\frac{1}{\rho^*}\frac{\partial p^*}{\partial X^*} + (s^*)'_{X^*}\frac{1}{\rho^*}\frac{\partial p^*}{\partial Y^*}$$

$$+\nu^*\left[\frac{\partial^2 u^*}{\partial X^{*2}} - (s^*)''_{X^*X^*}\frac{\partial u^*}{\partial Y^*} - 2(s^*)'_{X^*}\frac{\partial^2 u^*}{\partial X^*\partial Y^*} + [(s^*)'_{X^*}]^2\frac{\partial^2 u^*}{\partial Y^{*2}} + \frac{\partial^2 u^*}{\partial Y^{*2}}\right], \tag{2.1.6b}$$

$$u^*\frac{\partial v^*}{\partial X^*} - u^*(s^*)'_{X^*}\frac{\partial v^*}{\partial Y^*} + v^*\frac{\partial v^*}{\partial Y^*} = -\frac{1}{\rho^*}\frac{\partial p^*}{\partial Y^*}$$

$$+\nu^*\left[\frac{\partial^2 v^*}{\partial X^{*2}} - (s^*)''_{X^*X^*}\frac{\partial v^*}{\partial Y^*} - 2(s^*)'_{X^*}\frac{\partial^2 v^*}{\partial X^*\partial Y^*} + [(s^*)'_{X^*}]^2\frac{\partial^2 v^*}{\partial Y^{*2}} + \frac{\partial^2 v^*}{\partial Y^{*2}}\right]. \tag{2.1.6c}$$

In the X^*-Y^* coordinate system, the velocity components $(\tilde{u}^*, \tilde{v}^*)$ are expressed as

$$\begin{bmatrix}\tilde{u}^*\\ \tilde{v}^*\end{bmatrix} = \underbrace{\begin{bmatrix}1 & 0\\ -(s^*)'_{X^*} & 1\end{bmatrix}}_{J^*}\begin{bmatrix}u^*\\ v^*\end{bmatrix} = \begin{bmatrix}u^*\\ -(s^*)'_{X^*}u^* + v^*\end{bmatrix},$$

where J^* is the Jacobian of the transformation which is given by

$$J^* = \frac{\partial(X^*, Y^*)}{\partial(x^*, y^*)} = \begin{bmatrix}X^*_{x^*} & X^*_{y^*}\\ Y^*_{x^*} & Y^*_{y^*}\end{bmatrix}.$$

Therefore we obtain the following transformed velocity components

$$\tilde{u}^* = u^*, \tag{2.1.7a}$$

$$\tilde{v}^* = v^* - (s^*)'_X u^*. \tag{2.1.7b}$$

In what follows and to simplify the notation we drop the tilde on $\tilde{u}^*$ and use u^*. Given the above, we obtain the following set of governing equations

$$\frac{\partial u^*}{\partial X^*} + \frac{\partial \tilde{v}^*}{\partial Y^*} = 0, \tag{2.1.8a}$$

$$u^*\frac{\partial u^*}{\partial X^*} + \tilde{v}^*\frac{\partial u^*}{\partial Y^*} = -\frac{1}{\rho^*}\frac{\partial p^*}{\partial X^*} + \frac{(s^*)'_{X^*}}{\rho^*}\frac{\partial p^*}{\partial Y^*} + \nu^*\mathscr{L}_1^* u^*, \tag{2.1.8b}$$

$$(s^*)'_{X^*}\left(u^*\frac{\partial u^*}{\partial X^*} + \tilde{v}^*\frac{\partial u^*}{\partial Y^*}\right) + u^*\frac{\partial \tilde{v}^*}{\partial X^*} + \tilde{v}^*\frac{\partial \tilde{v}^*}{\partial Y^*} = -\frac{1}{\rho^*}\frac{\partial p^*}{\partial Y^*}$$

$$-u^{*2}(s^*)''_{X^*X^*} + \nu^*\mathscr{L}_1^*\tilde{v}^* + \nu^*(s^*)'\mathscr{L}_1^*u^* + \nu^*\mathscr{L}_2^*u^*, \tag{2.1.8c}$$

where we have introduced the following differential operators

$$\mathscr{L}_1^* = \frac{\partial^2}{\partial X^{*2}} - (s^*)''_{X^*X^*}\frac{\partial}{\partial Y^*} - 2(s^*)'_{X^*}\frac{\partial^2}{\partial X^*\partial Y^*} + (1+(s^*)'^2_{X^*})\frac{\partial}{\partial Y^{*2}},$$
$$\mathscr{L}_2^* = 2(s^*)''_{X^*X^*}\left(\frac{\partial}{\partial X^*} - (s^*)'_{X^*}\frac{\partial}{\partial Y^*}\right) + (s^*)'''_{X^*X^*X^*}.$$

Multiplying (2.1.8b) by $(s^*)'_{X^*}$ and subtracting it from (2.1.8c) yields

$$\frac{\partial u^*}{\partial X^*} + \frac{\partial \tilde{v}^*}{\partial Y^*} = 0,$$
$$u^*\frac{\partial u^*}{\partial X^*} + \tilde{v}^*\frac{\partial u^*}{\partial Y^*} = -\frac{1}{\rho^*}\frac{\partial p^*}{\partial X^*} + \nu^*\mathscr{L}_1^*u^* + \frac{(s^*)'_X}{\rho^*}\frac{\partial p^*}{\partial Y^*},$$
$$u^*\frac{\partial \tilde{v}^*}{\partial X^*} + \tilde{v}^*\frac{\partial \tilde{v}^*}{\partial Y^*} + (s^*)''_{X^*X^*}u^{*2} = -\frac{(1+(s^*)'^2_{X^*})}{\rho^*}\frac{\partial p^*}{\partial Y^*} + \nu^*\mathscr{L}_1^*\tilde{v}^* + \frac{(s^*)'_{X^*}}{\rho^*}\frac{\partial p^*}{\partial X^*} + \nu^*\mathscr{L}_2^*u^*.$$

The problem is non-dimensionalised by introducing the following scalings

$$(X,Y,s) = \frac{(X^*,Y^*,s^*)}{L^*}, \quad (u,\tilde{v}) = \frac{(u^*,\tilde{v}^*)}{U_w^*}, \quad p = \frac{p^*}{\rho^* U_w^{*2}}, \tag{2.1.11}$$

where L^* is a characteristic length-scale. Since we are considering a semi-infinite continuous moving wavy surface we set the non-dimensionalising length scale L^* equal to the wavelength of the roughness γ^*. To arrive at the boundary layer equations we introduce the following boundary layer scalings $\hat{Y} = Re^{\frac{1}{2}}Y$, and $v = Re^{\frac{1}{2}}\tilde{v}$, where the Reynolds number is defined as such $Re = U_w^*L^*/\nu^*$. The non-dimensional version of the equations are given as follows

$$\frac{\partial u}{\partial X} + \frac{\partial v}{\partial \hat{Y}} = 0, \tag{2.1.12a}$$

$$u\frac{\partial u}{\partial X} + v\frac{\partial u}{\partial \hat{Y}} = s'_X Re^{\frac{1}{2}}\frac{\partial p}{\partial \hat{Y}} - \frac{\partial p}{\partial X} + \sigma^2\frac{\partial^2 u}{\partial \hat{Y}^2}$$
$$-\frac{1}{Re^{\frac{1}{2}}}\left(s''_{XX}\frac{\partial u}{\partial \hat{Y}} + 2s'_X\frac{\partial^2 u}{\partial X \partial \hat{Y}}\right) + \frac{1}{Re}\frac{\partial^2 u}{\partial X^2}, \tag{2.1.12b}$$

$$\frac{1}{Re}\left(u\frac{\partial v}{\partial X} + v\frac{\partial v}{\partial \hat{Y}}\right) + \frac{s''_{XX}u^2}{Re^{\frac{1}{2}}} = \frac{s'_X}{Re^{\frac{1}{2}}}\frac{\partial p}{\partial X} - \sigma^2\frac{\partial p}{\partial \hat{Y}} + \frac{\sigma^2}{Re}\frac{\partial^2 v}{\partial \hat{Y}^2}$$
$$-\frac{1}{Re^{\frac{3}{2}}}\left(s''_{XX}\frac{\partial v}{\partial \hat{Y}} + 2s'_X\frac{\partial^2 v}{\partial X \partial \hat{Y}}\right) + \frac{1}{Re^2}\frac{\partial^2 v}{\partial X^2} + \frac{1}{Re}\left[2s''_{XX}\left(\frac{1}{Re^{\frac{1}{2}}}\frac{\partial u}{\partial X} - s'_X\frac{\partial u}{\partial \hat{Y}}\right) + \frac{s'''_{XXX}u}{Re^{\frac{1}{2}}}\right], \tag{2.1.12c}$$

where $\sigma^2 = (1 + (s')^2_X)$. We note that the function σ is directly related to the curvature of the surface, $\kappa = (s'_X)^{-1}\sigma^{-2}\sigma'_X$. To determine the leading order balance we introduce the following

$$u(X,\hat{Y}) = u_0(X,\hat{Y}) + Re^{-\frac{1}{2}}u_1(X,\hat{Y}) + \cdots$$
$$v(X,\hat{Y}) = v_0(X,\hat{Y}) + Re^{-\frac{1}{2}}v_1(X,\hat{Y}) + \cdots$$
$$p(X,\hat{Y}) = p_0(X) + Re^{-\frac{1}{2}}p_1(X,\hat{Y}) + \cdots$$

For boundary layer flows, as $Re \to \infty$, the $\mathcal{O}(1)$ term in equation (2.1.12c) yields

$$\frac{\partial p_0}{\partial \hat{Y}} = 0.$$

Therefore to leading order the pressure is a function of X alone. The $\mathcal{O}(1)$ terms in equation (2.1.12b) yields

$$u_0\frac{\partial u_0}{\partial X} + v_0\frac{\partial u_0}{\partial \hat{Y}} = -\frac{\partial p_0}{\partial X} + s'_X\frac{\partial p_1}{\partial \hat{Y}} + \sigma^2\frac{\partial^2 u_0}{\partial \hat{Y}^2}. \tag{2.1.13}$$

Now the $\mathcal{O}(Re^{-\frac{1}{2}})$ terms in equation (2.1.12c) yields

$$s''_{XX}u_0^2 = s'_X\frac{\partial p_0}{\partial X} - \sigma^2\frac{\partial p_1}{\partial \hat{Y}}.$$

Rearranging this for $\frac{\partial p_1}{\partial \hat{Y}}$, yields

$$\frac{\partial p_1}{\partial \hat{Y}} = \frac{1}{\sigma^2}\left(s'_X \frac{\partial p_0}{\partial X} - s''_{XX} u_0^2\right). \tag{2.1.14}$$

Substitution of (2.1.14) into (2.1.13) allows us to obtain the leading order governing equations, namely

$$\frac{\partial u_0}{\partial X} + \frac{\partial v_0}{\partial \hat{Y}} = 0, \tag{2.1.15a}$$

$$u_0 \frac{\partial u_0}{\partial X} + v_0 \frac{\partial u_0}{\partial \hat{Y}} + \frac{\sigma'_X}{\sigma} u_0^2 = -\frac{1}{\sigma^2}\frac{\mathrm{d}p_0}{\mathrm{d}X} + \sigma^2 \frac{\partial^2 u_0}{\partial \hat{Y}^2}. \tag{2.1.15b}$$

We now match the flow within the boundary-layer to the far-field flow, which, for this problem, is stationary. Therefore as $\hat{Y} \to \infty$, $u_0 \to 0$ therefore

$$-\frac{1}{\sigma^2}\frac{\mathrm{d}p_0}{\mathrm{d}X} = 0,$$

which implies that p_0 is constant and (2.1.15) reduces to

$$\frac{\partial u_0}{\partial X} + \frac{\partial v_0}{\partial \hat{Y}} = 0, \tag{2.1.16a}$$

$$u_0 \frac{\partial u_0}{\partial X} + v_0 \frac{\partial u_0}{\partial \hat{Y}} + \frac{\sigma'_X}{\sigma} u_0^2 = \sigma^2 \frac{\partial^2 u_0}{\partial \hat{Y}^2}. \tag{2.1.16b}$$

This set of PDEs has been derived by others, i.e., Hanevy *et al.* (2024). The non-dimensional variation of the surface height is given by

$$s(X) = a\cos(2\pi X). \tag{2.1.17}$$

Since we have defined the non-dimensionalising length-scale L^* as the wavelength of the surface roughness γ^*, and to maintain consistency with the analysis of Yoon *et al.* (2007), the dimensionless parameter $a = A^*/\gamma^*$ is referred to as the roughness parameter. As noted by other studies that have made use of sinusoidal wall profiles to model surface roughness, the roughness parameter must be kept small in order for the boundary-layer approximation to remain valid and to ensure that flow separation does not occur. In their experimental study over a rotating disk, Le Palec *et al.* (1990) argue that this theory is limited to the cases when the amplitude/wavelength ratio is much less than one $(a \leq 0.2)$. These experimental findings were verified theoretically by Mehmood *et al.* (2019*b*) with results being presented for cases when $a \leq 0.1$. Given these results, amongst others in the literature (see, for example, Yoon *et al.* (2007) and Garrett *et al.* (2016)), we will restrict our analysis to consider only cases where the ratio of the amplitude to the wavelength is less than or equal to one-fifth. System (2.1.16) is solved subject to the wall conditions

$$(u_0, v_0 + s'_X u_0) \cdot \hat{\mathbf{t}} = 1, \tag{2.1.18a}$$

$$(u_0, v_0 + s'_X u_0) \cdot \hat{\mathbf{n}} = 0, \tag{2.1.18b}$$

where $\hat{\mathbf{t}} = (1/\sigma, s'_X/\sigma)$, is the unit tangent vector to the wavy surface and $\hat{\mathbf{n}} = (-s'_X/\sigma, 1/\sigma)$, is the unit normal vector to the wavy surface. Combining the above conditions, and matching the boundary-layer flow with the inviscid flow above, we arrive at the following conditions that system (2.1.16) must be solved subject to

$$u_0(\hat{Y} = 0) = \frac{1}{\sigma}, \tag{2.1.19a}$$

$$v_0(\hat{Y} = 0) = 0, \tag{2.1.19b}$$

$$u_0(\hat{Y} \to \infty) \to 0. \tag{2.1.19c}$$

If the methods described above are applied to analyse the effects of surface roughness on boundary layer flows induced by an external free stream, the resulting boundary conditions will differ.

To ensure proper matching between the boundary-layer flow and the far-field flow, it is necessary to examine the inviscid flow outside the boundary layer, taking the wavy surface into account, to determine the correct matching conditions. Additionally, p_0 will no longer remain constant; refer to Appendix B for more details.

In what follows we will introduce a pseudo-similarity approach in order to solve (2.1.16) subject to (2.1.19). However, before we introduce our approach we revisit a similar analysis conducted by Rees & Pop (1995). In their study, focusing on boundary layer flow and heat transfer on a continuous moving wavy surface, Rees & Pop (1995) introduce a pseudo-similarity variable (based on the notation used here) of the following form: $\eta = \hat{Y}/(\sigma\sqrt{X})$. Having done so, they reduce the system of PDEs that govern the calculation of the boundary-layer flow using a streamfunction approach twinned with the introduction of this pseudo-similarity variable. The approach is entirely valid and, after having applied a suitable numerical scheme to solve the governing equation, yields insightful results. We choose not to adopt the same pseudo-similarity transformation here for the reason being that this form of η is dependent on the function σ. As such, as the value of the roughness parameter a varies, the pseudo-similarity variable itself varies, given that σ is directly dependent on the value of the roughness parameter. It is, therefore, difficult to draw conclusions with regards to how the boundary-layer flow is changing with increased levels of surface roughness when the variable the flow is dependent upon (the pseudo-similarity variable) is itself changing. This argument motivates us to consider the following transformation

$$\xi = X, \tag{2.1.20a}$$

$$\eta = \frac{\hat{Y}}{\sqrt{X}}, \tag{2.1.20b}$$

where $\psi = \sqrt{X} f(\xi, \eta)$, is not explicitly dependent on σ. Introducing the streamfunction

$$u_0 = \frac{\partial \psi}{\partial \hat{Y}}, \quad v_0 = -\frac{\partial \psi}{\partial X}, \tag{2.1.21}$$

the continuity equation is automatically satisfied and the momentum equation is now given by

$$\frac{\partial \psi}{\partial \hat{Y}} \frac{\partial^2 \psi}{\partial X \partial \hat{Y}} - \frac{\partial \psi}{\partial X} \frac{\partial^2 \psi}{\partial \hat{Y}^2} + \frac{\sigma'_X}{\sigma} \left[\left(\frac{\partial \psi}{\partial \hat{Y}} \right)^2 \right] = \sigma^2 \frac{\partial^3 \psi}{\partial \hat{Y}^3}. \tag{2.1.22}$$

Although the concept of the stream function originates from potential flow theory—where the flow is assumed to be inviscid, incompressible, and irrotational—its application extends beyond these idealised conditions. In potential theory, the stream function simplifies analysis by ensuring mass conservation and allowing the flow to be described without accounting for viscous effects. However, in boundary layer theory, where viscosity and shear stresses become significant near solid surfaces, the stream function remains valuable but serves a different purpose. It effectively describes the flow within the boundary layer, capturing viscous effects while still satisfying the incompressibility condition. While it could be referred to as a pseudo-stream function due to the breakdown of irrotational assumptions, we follow the standard convention of referring to it simply as the stream function. This approach aligns with the seminal work of Blasius (1907), who was the first to formally apply the stream function in boundary layer theory, providing an analytical solution for laminar flow over a flat plate—a result that remains foundational in modern fluid mechanics. Using the transformation given by (2.1.20) we obtain the following differential operators

$$\frac{\partial}{\partial \hat{Y}} = \xi^{-\frac{1}{2}} \frac{\partial}{\partial \eta}, \tag{2.1.23a}$$

$$\frac{\partial^2}{\partial \hat{Y}^2} = \xi^{-1} \frac{\partial^2}{\partial \eta^2}, \tag{2.1.23b}$$

$$\frac{\partial}{\partial X} = \frac{\partial}{\partial \xi} - \frac{\eta}{2\xi} \frac{\partial}{\partial \eta}. \tag{2.1.23c}$$

Given the definition of ψ we have that

$$\frac{\partial \psi}{\partial \hat{Y}} = \frac{\partial f}{\partial \eta}, \tag{2.1.24a}$$

$$\frac{\partial^2 \psi}{\partial \hat{Y}^2} = \xi^{-\frac{1}{2}} \frac{\partial^2 f}{\partial \eta^2}, \tag{2.1.24b}$$

$$\frac{\partial^3 \psi}{\partial \hat{Y}^3} = \xi^{-1} \frac{\partial^3 f}{\partial \eta^3}, \tag{2.1.24c}$$

$$\frac{\partial \psi}{\partial X} = \frac{1}{2}\xi^{-\frac{1}{2}} f + \xi^{\frac{1}{2}} \frac{\partial f}{\partial \xi} - \frac{\eta}{2}\xi^{-\frac{1}{2}} \frac{\partial f}{\partial \eta}, \tag{2.1.24d}$$

$$\frac{\partial^2 \psi}{\partial X \partial \hat{Y}} = \frac{\partial^2 f}{\partial \xi \partial \eta} - \frac{\eta}{2\xi} \frac{\partial^2 f}{\partial \eta^2}. \tag{2.1.24e}$$

Substituting (2.1.24) in to (2.1.22) gives the following governing PDE for f

$$\sigma^2 \frac{\partial^3 f}{\partial \eta^3} + \frac{f}{2} \frac{\partial^2 f}{\partial \eta^2} - \xi \frac{\sigma_\xi'}{\sigma} \left(\frac{\partial f}{\partial \eta} \right)^2 = \xi \left(\frac{\partial f}{\partial \eta} \frac{\partial^2 f}{\partial \xi \partial \eta} - \frac{\partial f}{\partial \xi} \frac{\partial^2 f}{\partial \eta^2} \right). \tag{2.1.25}$$

Note that the equation above differs to the one derived by Rees & Pop (1995) which is a direct consequence of the transformation given by (2.1.20). We can readily see using (2.1.18) and (2.1.21) that $\frac{\partial \psi}{\partial X} = 0$, when $\hat{Y} = 0$, therefore

$$\frac{1}{2}\xi^{-\frac{1}{2}} f + \xi^{\frac{1}{2}} \frac{\partial f}{\partial \xi} = 0,$$

on $\eta = 0$, which we can rewrite as follows

$$\frac{\partial f}{\partial \xi} + \frac{1}{2\xi} f = 0,$$

where the solution is given by $f = C_1 \xi^{-\frac{1}{2}}$ which implies that $C_1 = 0$ since we need f to be finite at $\xi = 0$. Therefore system (2.1.25) is solved subject to

$$f(\xi, \eta = 0) = 0, \tag{2.1.26a}$$

$$\frac{\partial f(\xi,\eta=0)}{\partial \eta} = \frac{1}{\sigma}, \tag{2.1.26b}$$

$$\frac{\partial f(\xi,\eta\to\infty)}{\partial \eta} \to 0. \tag{2.1.26c}$$

The initial flow profile is determined at the location $\xi = 0$ from the following ODE

$$\frac{\mathrm{d}^3 f}{\mathrm{d}\eta^3} + \frac{f}{2\sigma_0^2}\frac{\mathrm{d}^2 f}{\mathrm{d}\eta^2} = 0, \tag{2.1.27}$$

where $\sigma_0 = \sigma(\xi = 0) = 1$. Equation (2.1.27) describes the flow induced by the translation of a smooth, non-rough, surface. The flow configuration was first investigated analytically by Sakiadis (1961*a*) and is often now referred to as 'Sakiadis flow'.

2.2 Local Skin Friction Coefficient

An important physical quantity is the local skin friction which is directly related to the shear stress exerted by the fluid on the surface. It plays a crucial role in determining the drag force experienced by an object and is essential for understanding the behavior of the boundary layer. Accurate knowledge of the local skin friction coefficient helps in predicting flow separation points and optimizing surface designs to reduce drag. The local skin friction coefficient is defined as follows

$$C_f^* = \frac{\tau_w^*|_{y^*=0}}{\frac{1}{2}\rho^* U_w^{*2}}, \tag{2.2.1}$$

where τ_w is given by

$$\tau_w^* = \mu^* \left(\frac{\partial u^*}{\partial y^*} + \frac{\partial v^*}{\partial x^*} \right) \bigg|_{y^*=s^*(x^*)}. \tag{2.2.2}$$

Making use of both (2.1.2) and (2.1.7), we obtain

$$\tau_w^* = \mu^* \left((1-[(s^*)'_{X^*}]^2) \frac{\partial u^*}{\partial Y^*} + \frac{\partial \tilde{v}^*}{\partial X^*} + (s^*)''_{X^*X^*} u^* + (s^*)'_{X^*} \frac{\partial u^*}{\partial X^*} - (s^*)'_{X^*} \frac{\partial \tilde{v}^*}{\partial Y^*} \right) \bigg|_{Y^*=0}.$$

Using the scales given by (2.1.11), and the boundary layer scalings, we obtain the following

$$\frac{\tau_w^*}{\rho^* U_w^{*2}} = 2Re^{-1}\left(Re^{\frac{1}{2}}(1-(s'_X)^2)\frac{\partial u}{\partial \hat{Y}} + Re^{-\frac{1}{2}}\frac{\partial v}{\partial X} + s''_{XX}u + s'_X\frac{\partial u}{\partial X} - s'_X\frac{\partial v}{\partial \hat{Y}}\right),$$

where τ_w^* is evaluated at $\hat{Y}=0$. Multiplying both sides by $Re^{\frac{1}{2}}$ yields

$$Re^{\frac{1}{2}}C_f^* = 2\left((1-(s'_X)^2)\frac{\partial u}{\partial \hat{Y}} + Re^{-1}\frac{\partial v}{\partial X} + Re^{-\frac{1}{2}}s''_{XX}u + Re^{-\frac{1}{2}}s'_X\frac{\partial u}{\partial X} - Re^{-\frac{1}{2}}s'_X\frac{\partial v}{\partial \hat{Y}}\right),$$

Thus to leading order

$$C_f^* \approx 2Re^{-\frac{1}{2}}(1-(s'_X)^2)\frac{\partial u_0}{\partial \hat{Y}}.$$

Making use of the expression (2.1.24b), we have that

$$C_f^* = 2Re_{X^*}^{-\frac{1}{2}}(1-(s'_\xi)^2)f''(\xi,0), \tag{2.2.3}$$

where the local Reynolds number is defined like so $Re_{X^*} = U_w^* X^*/\nu^*$ where we note that $\xi^* = X^* = x^*$, thus $Re_{X^*} = Re_{\xi^*} = Re_{x^*}$. This is the Newtonian equivalent of the non-Newtonian expression derived by Pop & Nakamura (1996). When the surface is flat, the local skin friction coefficient can be expressed as:

$$C_f^* = 2Re_{X^*}^{-\frac{1}{2}}f''(\xi,0), \tag{2.2.4}$$

as shown in Tsou *et al.* (1967). In this case, there is no variation in the streamwise coordinate. In §3.2, we present the variation of $f''(\xi,0)$, which is directly related to the local skin friction coefficient. By analysing this variation, we can gain insights into the behavior of the local skin friction coefficient.

2.3 Numerical Method

In this section we derive the Keller-Box scheme used to solve (2.1.25) subject to (2.1.26) for a range of values of the roughness parameter a. The Keller-Box method has been used to solve a variety of boundary-layer problems, (see for example Rees & Pop (1995)) and the details of these types of schemes are well explained by Keller (1978). In all of our computations a step size of 0.001 is taken in the ξ direction where $0 \leq \xi \leq 1.5$. Further extending the domain in the streamwise direction increases the time it takes to compute the base flow profiles which we will show to be completely periodic in nature. First we define a set of uniformly distributed points in the vertical direction between 0 and η_{max} with the jth point denoted by $\tilde{\eta}_j$. In the present analysis we have used $\eta_{max} = 100$. Then we introduce the mapping

$$\eta_j = \tilde{\eta}_j \exp\left(\frac{\tilde{\eta}_j - \eta_{max}}{\eta_{max}}\right),$$

so that the corresponding jth point η_j form a set of non-uniformly distributed points between 0 and η_{max} which are more concentrated near the wall where the interesting behaviour, with respect to the effects of surface roughness, are most prominent. To simplify the notation we will rewrite (2.1.25) as follows

$$\sigma^2 f'''_{\eta\eta\eta} + \frac{1}{2} f f''_{\eta\eta} - \xi \frac{\sigma'_\xi}{\sigma}(f'_\eta)^2 = \xi(f'_\eta f'_{\xi\eta} - f_\xi f''_{\eta\eta}). \tag{2.3.1}$$

We start by rewriting (2.3.1) as a system of ODES. Let

$$a = f, \tag{2.3.2a}$$

$$b = f'_\eta, \tag{2.3.2b}$$

$$c = f''_{\eta\eta}. \tag{2.3.2c}$$

Therefore

$$a'_\eta - b = 0, \tag{2.3.3a}$$

$$b'_\eta - c = 0, \tag{2.3.3b}$$

$$\sigma^2 c'_\eta + \frac{1}{2}ac - \xi\frac{\sigma'_\xi}{\sigma}b^2 - \xi(bb_\xi - a_\xi c) = 0. \tag{2.3.3c}$$

To initialise the solution we set the initial velocity profile at $\xi = 0$ equal to the similarity solution. We solve for the initial solution using a fourth order Runga Kutta scheme combined with the secant searching method. This initial solution is our initial guess for the profile at $\xi^i = \xi^{i-1} + \Delta\xi$ for $1 \leq i \leq N$. The PDE is evaluated at $(\xi^{i-\frac{1}{2}}, \eta_{j-\frac{1}{2}})$ where i represents the current position in the ξ direction and j represents the current position in the η direction and $\eta_j = \eta_{j-1} + \Delta\eta$ for $1 \leq j \leq N$. The following differences are used and will aid in simplifying notation,

$$\Delta_\eta a^i_j = \frac{1}{2\Delta\eta}(a^i_j + a^{i-1}_j - a^i_{j-1} - a^{i-1}_{j-1}), \tag{2.3.4a}$$

$$\Delta_\xi a^i_j = \frac{1}{2\Delta\xi}(a^i_j - a^{i-1}_j + a^i_{j-1} - a^{i-1}_{j-1}), \tag{2.3.4b}$$

$$a^{i-\frac{1}{2}}_{j-\frac{1}{2}} = \frac{1}{4}(a^i_j + a^{i-1}_j + a^i_{j-1} + a^{i-1}_{j-1}). \tag{2.3.4c}$$

On substituting (2.3.4) into (2.3.3) we obtain the following

$$\Delta_\eta a^i_j - b^{i-\frac{1}{2}}_{j-\frac{1}{2}} = 0, \tag{2.3.5a}$$

$$\Delta_\eta b^i_j - c^{i-\frac{1}{2}}_{j-\frac{1}{2}} = 0, \tag{2.3.5b}$$

$$(\sigma^2)^{i-\frac{1}{2}}\Delta_\eta c^i_j + \frac{1}{2}a^{i-\frac{1}{2}}_{j-\frac{1}{2}}c^{i-\frac{1}{2}}_{j-\frac{1}{2}} - \frac{\sigma'_\xi}{\sigma}\xi^{i-\frac{1}{2}}\left(b^{i-\frac{1}{2}}_{j-\frac{1}{2}}\right)^2 - \xi^{i-\frac{1}{2}}\left(b^{i-\frac{1}{2}}_{j-\frac{1}{2}}\Delta_\xi b^i_j - c^{i-\frac{1}{2}}_{j-\frac{1}{2}}\Delta_\xi a^i_j\right) = 0, \tag{2.3.5c}$$

which is solved subject to the boundary conditions $a^i_1 = 0$, $b^i_1 - 1/\sigma(\xi_i) = 0$, and $b^i_N = 0$. We solve the above using a Newton-Raphson iteration. To do this we let $a^i_j = a^{i(n)}_j + \varepsilon \hat{a}^i_j$ and define the latest guess i.e. the n^{th} iterate where ε denotes a correction to our current guess, assumed to be small. We obtain similar equations for both b and c. Applying the Newton-Raphson iteration to (2.3.5) and neglecting all appearances of powers of ε greater than the first power yields the following

$$\frac{1}{2\Delta\eta}(a^{i(n)}_j + \varepsilon\hat{a}^i_j + a^{i-1}_j - a^{i(n)}_{j-1} - \varepsilon\hat{a}^i_{j-1} - a^{i-1}_{j-1}) - \frac{1}{4}(b^{i(n)}_j + \varepsilon\hat{b}^i_j + b^{i-1}_j + b^{i(n)}_{j-1} + \varepsilon\hat{b}^i_{j-1} + b^{i-1}_{j-1}) = 0.$$

Therefore we have that

$$\frac{1}{\Delta\eta}(\varepsilon\hat{a}^i_j - \varepsilon\hat{a}^i_{j-1}) - \frac{1}{2}(\varepsilon\hat{b}^i_j + \varepsilon\hat{b}^i_{j-1}) = r^i_{1_j},$$

where

$$(r_1)^i_j = -\frac{1}{\Delta\eta}(a^{i(n)}_j + a^{i-1}_j - a^{i(n)}_{j-1} - a^{i-1}_{j-1}) + \frac{1}{2}(b^{i(n)}_j + b^{i-1}_j + b^{i(n)}_{j-1} + b^{i-1}_{j-1}).$$

Similarly we obtain

$$\frac{1}{2\Delta\eta}(b^{i(n)}_j + \varepsilon\hat{b}^i_j + b^{i-1}_j - b^{i(n)}_{j-1} - \varepsilon\hat{b}^i_{j-1} - b^{i-1}_{j-1}) - \frac{1}{4}(c^{i(n)}_j + \varepsilon\hat{c}^i_j + c^{i-1}_j + c^{i(n)}_{j-1} + \varepsilon\hat{c}^i_{j-1} + c^{i-1}_{j-1}) = 0.$$

Therefore

$$\frac{1}{\Delta\eta}(\varepsilon\hat{b}^i_j - \varepsilon\hat{b}^i_{j-1}) - \frac{1}{2}(\varepsilon\hat{c}^i_j + \varepsilon\hat{c}^i_{j-1}) = r^i_{2_j},$$

where

$$(r_2)^i_j = -\frac{1}{\Delta\eta}(b^{i(n)}_j + b^{i-1}_j - b^{i(n)}_{j-1} - b^{i-1}_{j-1}) + \frac{1}{2}(c^{i(n)}_j + c^{i-1}_j + c^{i(n)}_{j-1} + c^{i-1}_{j-1}).$$

For the momentum equation we have that

$$\begin{aligned}
&\frac{(\sigma^2)^{i-\frac{1}{2}}}{2\Delta\eta}(c_j^{i(n)}+\varepsilon\hat{c}_j^i+c_j^{i-1}-c_{j-1}^{i(n)}-\varepsilon\hat{c}_{j-1}^i-c_{j-1}^{i-1})\\
&+\frac{1}{32}(a_j^{i(n)}+\varepsilon\hat{a}_j^i+a_j^{i-1}+a_{j-1}^{i(n)}+\varepsilon\hat{a}_{j-1}^i+a_{j-1}^{i-1})(c_j^{i(n)}+\varepsilon\hat{c}_j^i+c_j^{i-1}+c_{j-1}^{i(n)}+\varepsilon\hat{c}_{j-1}^i+c_{j-1}^{i-1})\\
&-\left(\xi\frac{\sigma'_\xi}{\sigma}\right)^{i-\frac{1}{2}}\frac{1}{16}(b_j^{i(n)}+\varepsilon\hat{b}_j^i+b_j^{i-1}+b_{j-1}^{i(n)}+\varepsilon\hat{b}_{j-1}^i+b_{j-1}^{i-1})^2\\
&-\frac{\xi^{i-\frac{1}{2}}}{8\Delta\xi}(b_j^{i(n)}+\varepsilon\hat{b}_j^i+b_j^{i-1}+b_{j-1}^{i(n)}+\varepsilon\hat{b}_{j-1}^i+b_{j-1}^{i-1})(b_j^{i(n)}+\varepsilon\hat{b}_j^i-b_j^{i-1}+b_{j-1}^{i(n)}+\varepsilon\hat{b}_{j-1}^i-b_{j-1}^{i-1})\\
&+\frac{\xi^{i-\frac{1}{2}}}{8\Delta\xi}(c_j^{i(n)}+\varepsilon\hat{c}_j^i+c_j^{i-1}+c_{j-1}^{i(n)}+\varepsilon\hat{c}_{j-1}^i+c_{j-1}^{i-1})(a_j^{i(n)}+\varepsilon\hat{a}_j^i-a_j^{i-1}+a_{j-1}^{i(n)}+\varepsilon\hat{a}_{j-1}^i-a_{j-1}^{i-1})=0.
\end{aligned} \tag{2.3.6}$$

Now

$$\begin{aligned}
&\frac{(\sigma^2)^{i-\frac{1}{2}}}{2\Delta\eta}(\varepsilon\hat{c}_j^i-\varepsilon\hat{c}_{j-1}^i)+\frac{1}{32}(a_j^{i(n)}+a_j^{i-1}+a_{j-1}^{i(n)}+a_{j-1}^{i-1})(\varepsilon\hat{c}_j^i+\varepsilon\hat{c}_{j-1}^i)\\
&+\frac{1}{32}(c_j^{i(n)}+c_j^{i-1}+c_{j-1}^{i(n)}+c_{j-1}^{i-1})(\varepsilon\hat{a}_j^i+\varepsilon\hat{a}_{j-1}^i)\\
&-\left(\xi\frac{\sigma'_\xi}{\sigma}\right)^{i-\frac{1}{2}}\frac{1}{8}(b_j^{i(n)}+b_j^{i-1}+b_{j-1}^{i(n)}+b_{j-1}^{i-1})(\varepsilon\hat{b}_j+\varepsilon\hat{b}_{j-1}^i)\\
&-\xi^{i-\frac{1}{2}}\frac{1}{8\Delta\xi}(\varepsilon\hat{b}_j^i+\varepsilon\hat{b}_{j-1}^i)(b_j^{i(n)}-b_j^{i-1}+b_{j-1}^{i(n)}-b_{j-1}^{i-1})\\
&-\xi^{i-\frac{1}{2}}\frac{1}{8\Delta\xi}(\varepsilon\hat{b}_j^i+\varepsilon\hat{b}_{j-1}^i)(b_j^{i(n)}+b_j^{i-1}+b_{j-1}^{i(n)}+b_{j-1}^{i-1})\\
&+\xi^{i-\frac{1}{2}}\frac{1}{8\Delta\xi}(\varepsilon\hat{c}_j^i+\varepsilon\hat{c}_{j-1}^i)(a_j^{i(n)}-a_j^{i-1}+a_{j-1}^{i(n)}-a_{j-1}^{i-1})\\
&+\xi^{i-\frac{1}{2}}\frac{1}{8\Delta\xi}(\varepsilon\hat{a}_j^i+\varepsilon\hat{a}_{j-1}^i)(c_j^{i(n)}+c_j^{i-1}+c_{j-1}^{i(n)}+c_{j-1}^{i-1})=r_{3_j}^i,
\end{aligned} \tag{2.3.7}$$

where r_3 is given by

$$(r_3)^i_j = -(\sigma^2)^{i-\frac{1}{2}}\Delta_\eta c^i_j - \frac{1}{2}a^{i-\frac{1}{2}}_{j-\frac{1}{2}}c^{i-\frac{1}{2}}_{j-\frac{1}{2}} - \left(\frac{\sigma'_\xi}{\sigma}\xi\right)^{i-\frac{1}{2}}\left(b^{i-\frac{1}{2}}_{j-\frac{1}{2}}\right)^2 + \xi^{i-\frac{1}{2}}\left(b^{i-\frac{1}{2}}_{j-\frac{1}{2}}\Delta_\xi b^i_j - c^{i-\frac{1}{2}}_{j-\frac{1}{2}}\Delta_\xi a^i_j\right).$$

The difference equations have the form

$$\frac{1}{\Delta\eta}(\varepsilon\hat{a}^i_j - \varepsilon\hat{a}^i_{j-1}) - \frac{1}{2}(\varepsilon\hat{b}^i_j + \varepsilon\hat{b}^i_{j-1}) = (r_1)^i_j, \tag{2.3.8a}$$

$$\frac{1}{\Delta\eta}(\varepsilon\hat{b}^i_j - \varepsilon\hat{b}^i_{j-1}) - \frac{1}{2}(\varepsilon\hat{c}^i_j + \varepsilon\hat{c}^i_{j-1}) = (r_2)^i_j, \tag{2.3.8b}$$

$$(\alpha_1)^i_j\varepsilon\hat{a}^i_j + (\alpha_2)^i_j\varepsilon\hat{a}^i_{j-1} + (\alpha_3)^i_j\varepsilon\hat{b}^i_j + (\alpha_4)^i_j\varepsilon\hat{b}^i_{j-1} + (\alpha_5)^i_j\varepsilon\hat{c}^i_j + (\alpha_6)^i_j\varepsilon\hat{c}^i_{j-1} = (r_3)^i_j, \tag{2.3.8c}$$

where the coefficients of the momentum equation are given by

$$(\alpha_1)^i_j = c^{i-\frac{1}{2}}_{j-\frac{1}{2}}\left(\frac{1}{8} + (\xi)^{i-\frac{1}{2}}\frac{1}{2\Delta\xi}\right), \tag{2.3.9a}$$

$$(\alpha_2)^i_j = (\alpha_1)^i_j, \tag{2.3.9b}$$

$$(\alpha_3)^i_j = -\left(\frac{\sigma'_\xi}{\sigma}\xi\right)^{i-\frac{1}{2}}\frac{1}{2}b^{i-\frac{1}{2}}_{j-\frac{1}{2}} - \xi^{i-\frac{1}{2}}\left(\frac{1}{4\Delta\xi}(b^{i(n)}_j + b^{i(n)}_{j-1})\right), \tag{2.3.9c}$$

$$(\alpha_4)^i_j = (\alpha_3)^i_j \tag{2.3.9d}$$

$$(\alpha_5)^i_j = \frac{(\sigma^2)^{i-\frac{1}{2}}}{2\Delta\eta} + \frac{1}{8}a^{i-\frac{1}{2}}_{j-\frac{1}{2}} + \frac{1}{4}\xi^{i-\frac{1}{2}}\Delta_\xi a^i_j, \tag{2.3.9e}$$

$$(\alpha_6)^i_j = -\frac{(\sigma^2)^{i-\frac{1}{2}}}{2\Delta\eta} + \frac{1}{8}a^{i-\frac{1}{2}}_{j-\frac{1}{2}} + \frac{1}{4}\xi^{i-\frac{1}{2}}\Delta_\xi a^i_j. \tag{2.3.9f}$$

We have only imposed that the perturbations satisfy the ordinary differential equations in (2.3.8a) and (2.3.8b) as this prevented oscillations from developing in the corrections. By preventing these oscillations in the corrections our numerical scheme was able to converge successfully. To understand the structure of (2.3.8) we consider only two grid points and obtain the following matrix equation

$$
\begin{bmatrix}
1 & 0 & 0 & 0 & 0 & 0 \\
0 & 1 & 0 & 0 & 0 & 0 \\
-\frac{1}{\Delta\eta} & -\frac{1}{2} & 0 & \frac{1}{\Delta\eta} & -\frac{1}{2} & 0 \\
0 & -\frac{1}{\Delta\eta} & -\frac{1}{2} & 0 & \frac{1}{\Delta\eta} & -\frac{1}{2} \\
(\alpha_2)_2^i & (\alpha_4)_2^i & (\alpha_6)_2^i & (\alpha_1)_2^i & (\alpha_3)_2^i & (\alpha_5)_2^i \\
0 & 0 & 0 & 0 & 1 & 0
\end{bmatrix}
\begin{bmatrix}
\varepsilon\hat{a}_1^i \\ \varepsilon\hat{b}_1^i \\ \varepsilon\hat{c}_1^i \\ \varepsilon\hat{a}_2^i \\ \varepsilon\hat{b}_2^i \\ \varepsilon\hat{c}_2^i
\end{bmatrix}
=
\begin{bmatrix}
-a_1^{i(n)} \\ \frac{1}{\sigma_1^i} - b_1^{i(n)} \\ (r_1)_2^i \\ (r_2)_2^i \\ (r_3)_2^i \\ -b_2^{i(n)}
\end{bmatrix}. \tag{2.3.10}
$$

The above matrix falls into a block diagonal structure where the individual sub matrix blocks are 3×3 matrices, which is readily seen if we choose an arbitrary number of grid points. The above system takes the following form where the A_i, B_i, and C_i, are defined below

$$
\begin{bmatrix}
B_1^i & C_1^i & 0 & \cdots & 0 & 0 & 0 \\
A_2^i & B_2^i & C_2^i & \cdots & 0 & 0 & 0 \\
\vdots & \vdots & \vdots & \ddots & \vdots & \vdots & \vdots \\
0 & 0 & 0 & \cdots & 0 & A_N^i & B_N^i
\end{bmatrix}
\begin{bmatrix}
\varepsilon_1^i \\ \varepsilon_2^i \\ \vdots \\ \varepsilon_N^i
\end{bmatrix}
=
\begin{bmatrix}
R_1^i \\ R_2^i \\ \vdots \\ R_N^i
\end{bmatrix}. \tag{2.3.11}
$$

Note that in system (2.3.10) the leading block on the diagonal, B_1 is singular, therefore we interchange rows three and four and obtain the following

$$
\begin{bmatrix}
1 & 0 & 0 & 0 & 0 & 0 \\
0 & 1 & 0 & 0 & 0 & 0 \\
0 & -\frac{1}{\Delta\eta} & -\frac{1}{2} & 0 & \frac{1}{\Delta\eta} & -\frac{1}{2} \\
-\frac{1}{\Delta\eta} & -\frac{1}{2} & 0 & \frac{1}{\Delta\eta} & -\frac{1}{2} & 0 \\
(\alpha_2)_2^i & (\alpha_4)_2^i & (\alpha_6)_2^i & (\alpha_1)_2^i & (\alpha_3)_2^i & (\alpha_5)_2^i \\
0 & 0 & 0 & 0 & 1 & 0
\end{bmatrix}
\begin{bmatrix}
\varepsilon\hat{a}_1^i \\ \varepsilon\hat{b}_1^i \\ \varepsilon\hat{c}_1^i \\ \varepsilon\hat{a}_2^i \\ \varepsilon\hat{b}_2^i \\ \varepsilon\hat{c}_2^i
\end{bmatrix}
=
\begin{bmatrix}
-a_1^{i(n)} \\ \frac{1}{\sigma_1^i} - b_1^{i(n)} \\ (r_2)_2^i \\ (r_1)_2^i \\ (r_3)_2^i \\ -b_2^{i(n)}
\end{bmatrix}. \tag{2.3.12}
$$

The general form of (2.3.11) is given as follows,

$$B^i_j = \begin{bmatrix} \frac{1}{\Delta\eta} & -\frac{1}{2} & 0 \\ (\alpha_1)^i_j & (\alpha_3)^i_j & (\alpha_6)^i_j \\ 0 & -\frac{1}{\Delta\eta} & -\frac{1}{2} \end{bmatrix}, \tag{2.3.13}$$

$$A^i_j = \begin{bmatrix} -\frac{1}{\Delta\eta} & -\frac{1}{2} & 0 \\ (\alpha_2)^i_j & (\alpha_4)^i_j & (\alpha_6)^i_j \\ 0 & 0 & 0 \end{bmatrix}, \tag{2.3.14}$$

$$C^i_j = \begin{bmatrix} 0 & 0 & 0 \\ 0 & 0 & 0 \\ 0 & \frac{1}{\Delta\eta} & -\frac{1}{2} \end{bmatrix}, \tag{2.3.15}$$

and

$$R^i_j = \begin{bmatrix} (r_1)^i_j \\ (r_2)^i_j \\ (r_3)^i_j \end{bmatrix}. \tag{2.3.16}$$

At the surface we have that

$$B^i_1 = \begin{bmatrix} 1 & 0 & 0 \\ 0 & 1 & 0 \\ 0 & -\frac{1}{\Delta\eta} & -\frac{1}{2} \end{bmatrix}, \tag{2.3.17}$$

and

$$R^i_1 = \begin{bmatrix} -a_1^{i(n)} \\ \frac{1}{\sigma_1} - b_1^{i(n)} \\ (r_2)^i_2 \end{bmatrix}. \tag{2.3.18}$$

At the free stream we have that

$$B_N^i = \begin{bmatrix} \frac{1}{\Delta\eta} & -\frac{1}{2} & 0 \\ (\alpha_1)_N^i & (\alpha_3)_N^i & (\alpha_5)_N^i \\ 0 & 1 & 0 \end{bmatrix}, \tag{2.3.19}$$

and

$$R_N^i = \begin{bmatrix} (r_1)_N^i \\ (r_3)_N^i \\ -b_N^i \end{bmatrix}. \tag{2.3.20}$$

The form of the matrices has a block diagonal structure therefore the solution is obtained using a block diagonal version of the 'well known' tridiagonal matrix algorithm. The technique involves inverting the 'sub matrix' blocks on the diagonal.

Chapter 3

Basic Flow Solutions

In this Chapter we derive the basic flow solutions via two means. In the first instance we obtain the solutions numerically via the Keller-Box approach discussed in §2.3. This method utilities the parabolic nature of the boundary layer equations. For the second case we verify our Keller-Box solutions by exploiting the periodicity of the basic flow and adopting a suitable similarity approach. The study of this two-dimensional flow is similar in some sense, to the three-dimensional rotating disk flow studies conducted by Cooper *et al.* (2015) and Garrett *et al.* (2016). In their analysis, Garrett *et al.* (2016) argued that, given that the radial, azimuthal, and wall-normal flows are radially periodic, and that a similarity-type solution at a large spatial scale is observed, it is a reasonable approximation to take a radial average of the flow field over any complete period of the roughness profile. Having done so, this leads them to arrive at modified von Kármán mean flow profiles that vary only with the wall-normal coordinate. This process is advantageous with respect to the associated stability analysis as it allows for the reduction of both the complexity and dimensionality of the governing system of linear disturbance equations. In essence, having made the assumption of base flow self-similarity, the surface variation is ‘averaged away’ so that one needs only to solve the ordinary differential equations that define the linear stability characteristics of flows over smooth rotating disks (see, for example, Lingwood (1995)). We present a similar argument here.

In §3.1 we analyse the boundary layer formed on a continuously moving flat surface and derive the basic flow solutions. In §3.2 we derive the basic flow solutions induced by a continuously moving wavy surface via the Keller-Box method and examine how the base state varies in the streamwise direction. In §3.3 we follow the work of Garrett *et al.* (2016) and derive the averaged flow solutions for various values of the roughness parameter. Finally in §3.4 we verify our solutions obtained via the Keller-Box method by exploiting the self-similar periodicity in the base flow.

3.1 The Sakiadis Solution

We begin by analysing the boundary layer that develops on a continuously moving flat surface, a problem first studied analytically by Sakiadis (1961*b*). Specifically, we consider a steady, two-dimensional, incompressible flow over a flat surface moving at a constant velocity within a stationary fluid, where body forces are absent. The boundary layer equations governing this configuration are as follows:

$$\frac{\partial u_0}{\partial X} + \frac{\partial v_0}{\partial \hat{Y}} = 0, \tag{3.1.1a}$$

$$u_0 \frac{\partial u_0}{\partial X} + v_0 \frac{\partial u_0}{\partial \hat{Y}} = \frac{\partial^2 u_0}{\partial \hat{Y}^2}, \tag{3.1.1b}$$

where the system is solved subject to the following boundary conditions

$$u_0(\hat{Y} = 0) = 1, \quad v_0(\hat{Y} = 0) = 0, \quad u_0(\hat{Y} \to \infty) \to 0. \tag{3.1.2}$$

We note that the boundary layer equations that describe a non-flat surface reduce to (3.1.1) when the boundary is flat. By introducing the stream function (2.1.21) where $\psi = \sqrt{X} f(\eta)$, and the similarity variable

$$\eta = \frac{\hat{Y}}{\sqrt{X}},$$

the continuity equation is automatically satisfied and the velocity components become

$$u_0 = f'_\eta, \tag{3.1.3a}$$

$$v_0 = \frac{1}{2\sqrt{X}}(\eta f'_\eta - f), \tag{3.1.3b}$$

where the $'$ indicates differentiation with respect η. This leads to the following equation

$$f'''_{\eta\eta\eta} + \frac{1}{2} f f''_{\eta\eta} = 0, \tag{3.1.4}$$

which is solved subject to the conditions

$$f(\eta = 0) = 0, \quad f'_\eta(\eta = 0) = 1, \quad f'_\eta(\eta \to \infty) \to 0. \tag{3.1.5}$$

This is the Blasius equation. However, the boundary conditions that must be satisfied are not the same and will result in a different solution to the one obtained by Blasius. This difference is due to the surface translating in the streamwise direction at a constant velocity in a quiescent fluid, whereas for Blasius flow, the surface is at rest and is subjected to an oncoming unidirectional flow. A comparison of the two flow configurations is well explained in the works of Sakiadis (Sakiadis (1961*a*), Sakiadis (1961*b*)) and Abdelhafez (1985). The solution to (3.1.4) is readily accomplished using numerical methods and we solve (3.1.4) using a fourth order Runga-Kutta scheme combined together with a secant searching method.

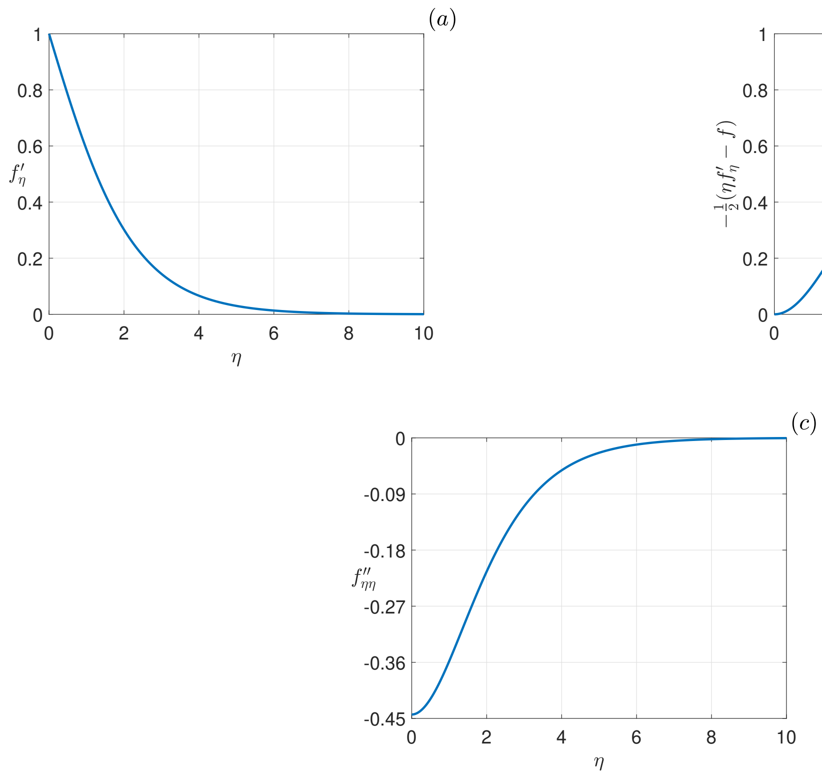

Figure 3.1: The streamwise profile $u_0 = f'_\eta$ versus the similarity variable η is presented in (a). The wall-normal flow component $-\sqrt{X}v_0$ versus η is presented in (b). The shear, $f''_{\eta\eta}$ versus η is presented in (c).

From Figure 3.1 we can readily see that the boundary layer grows in a direction that the surface is moving. At the outer edge of the boundary layer we have that $\sqrt{X}v_0 = -0.8081$ where the negative sign indicates an influx of fluid across the limit of the boundary layer. We also find that $f''_{\eta\eta}(0) = -0.4437$ in agreement with Tsou *et al.* (1967) and Rees & Pop (1995). The boundary layer thickness for flows of this type is defined as the distance from the moving surface at which $u^* = 0.01U^*_w$. We determine that the boundary layer thickness is as follows

$$\delta(x^*) \approx 6.375\sqrt{\frac{\nu^* x^*}{U^*_w}} = 6.375\frac{x^*}{\sqrt{Re_{x^*}}}.$$

An alternative measure of the thickness of the boundary layer flow is the displacement thickness.

This quantity is defined for this problem like so

$$\delta^* = \int_0^\infty \frac{u^*}{U_w^*}\,\mathrm{d}y^* = \frac{x^*}{\sqrt{Re_{x^*}}}\int_0^\infty f_\eta'(\eta)\,\mathrm{d}\eta = \frac{x^*}{\sqrt{Re_{x^*}}}\delta,$$

where $\delta = f(\eta = \eta_{max}) = 1.6161$, which corresponds to the wall-normal flow component $\sqrt{X}v_0$ in the limit as $\eta \to \infty$. We find that our results for the smooth boundary are in excellent agreement with Sakiadis (1961*b*) and other authors such as Tsou *et al.* (1967) and Rees & Pop (1995).

3.2 The Boundary Layer Flow Induced by a Continuously Moving Rough Surface

We now consider a surface that is translating at a constant velocity in an otherwise quiescent fluid where the surface is described by the function given in (2.1.17), and the governing equation describing such a flow is given by (2.1.25).

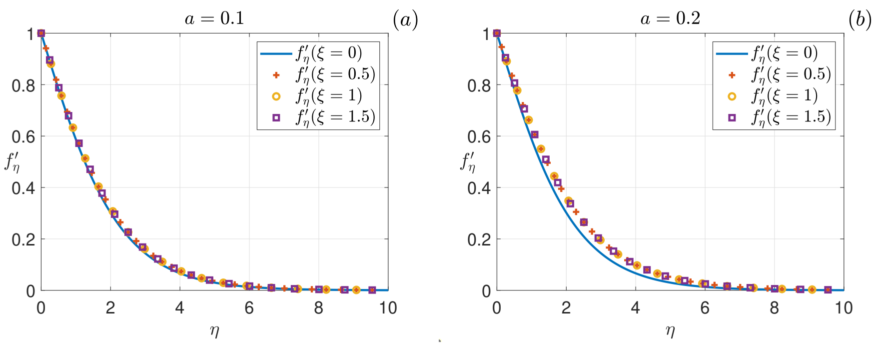

Figure 3.2: (a) Shows a range of streamwise velocity profiles at varying ξ locations when $a = 0.1$. (b) Shows profiles at identical streamwise locations to (a) but with $a = 0.2$. Here we illustrate the initial profile along with solutions at the peaks and troughs of the translating wavy surface where a is the roughness parameter.

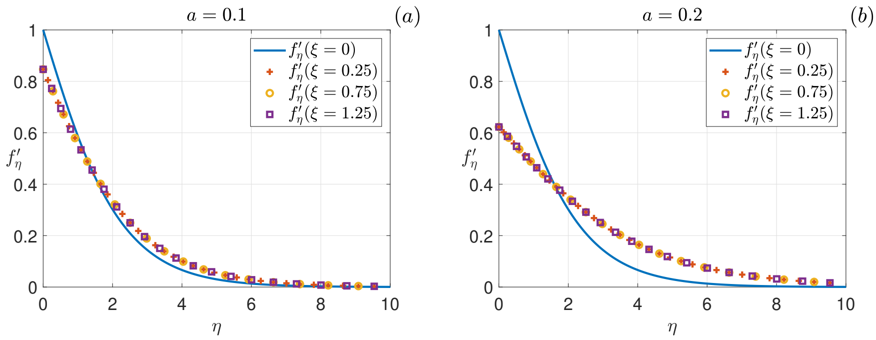

Figure 3.3: In (a) we illustrate a range of streamwise velocity profiles at varying ξ locations in the instance when $a = 0.1$. In (b) we illustrate profiles at identical streamwise locations but with $a = 0.2$. Here we show the initial profile along with solutions at the zeros of the translating wavy surface where a is the roughness parameter.

From Figure 3.2, it can be observed that the streamwise velocity profiles are identical at the peaks and troughs of the wavy surface ($\xi = \frac{n}{2}$ for $n \in \mathbb{Z}^+$). More importantly, the velocity profiles at these locations are distinct from the initial solution at $\xi = 0$. While this distinction may not be immediately apparent, a closer examination—such as zooming into Figure 3.2—reveals the difference between the initial solution at $\xi = 0$ and the profiles at $\xi = \frac{n}{2}$.

In Figure 3.3 we present solutions for the streamwise velocity profile at the locations where $\xi = \frac{2n-1}{4}$ for $n \in \mathbb{Z}^+$, these being the locations at which $s = 0$, the 'zeros' of the wavy surface. Once again, we observe that the solution at $\xi = 0$ differs from these periodic solutions, as previously discussed. We note that streamwise velocity profiles are obtained for all values of ξ; however, by focusing on the specific locations discussed above, we effectively emphasise the streamwise periodicity of the base flow while maintaining clarity in the presentation. For values of ξ around 0.5 or greater we observe a cyclical variation in the basic flow solutions which is best visualised via the streamwise variation of the shear at the wall, see Figure 3.4.

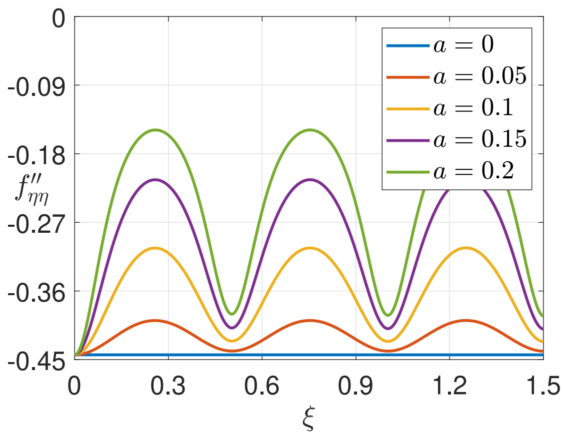

Figure 3.4: The variation of the shear at the wall, $f''_{\eta\eta}$ at the wall, illustrated as a function of the streamwise coordinate ξ, for a range of values of the roughness parameter.

Our results agree qualitatively with the theoretical results presented by Rees & Pop (1995) and the experimental findings of Le Palec *et al.* (1990). In accordance with those studies, we find that as the roughness parameter increases from zero the minimum absolute value of the shear at the wall decreases. From Figure 3.4, we can infer that as a increases beyond moderate values (e.g., $a > 0$), the boundary-layer flow undergoes separation. When this occurs, the fundamental assumptions of classical boundary-layer theory are no longer valid, giving rise to a different flow regime. In an attached boundary layer, the streamwise velocity remains predominantly parallel to the surface, allowing the boundary-layer equations to accurately describe the flow. However, upon separation, the flow detaches from the surface, leading to the formation of a recirculating region where the boundary-layer approximation breaks down. In this regime, the full Navier-Stokes equations must be employed to capture complex flow phenomena such as reverse flow, vortex shedding, and pressure-driven separation. The transition from an attached to a separated boundary layer marks a shift from a viscous-dominated problem to one where inertial, turbulent, and unsteady effects become significant. We notice the flow is doubly periodic (with respect to the period of the roughness profile itself). However the flow is not immediately periodic and the initial flow profile must be allowed to develop downstream from the leading edge before periodicity is first observed.

3.3 Averaged Flow Profiles

In this section, we compute the ensemble average of the base flow quantities at 1000 equally spaced locations along the semi-infinite plate, spanning the interval $[\xi_0, \xi_1] = [0.5, 1.5]$. This range corresponds to a full wavelength of the wavy surface, ensuring a comprehensive representation of its periodic characteristics. This process produces base flow profiles that have no dependence on the streamwise variable ξ. Having computed these spatial averages we have that $\bar{s}(\xi) = 0$, where the overbar represents an averaged quantity. Physically, as was first argued by Harris (2013), this averaging procedure makes sense as the scale associated with the amplitude of the rough surface is small compared to the thickness of the boundary layer. Thus, for the ensuing linear stability analyses the flow field varies in a self-similar manner with profiles being defined as follows

$$\begin{aligned} u_0 &= \overline{f'_\eta}(\eta) = u_B, \\ v_0 &= \frac{\overline{f}(\eta) - \eta \overline{f'_\eta}(\eta)}{2\sqrt{\xi}} = v_B, \end{aligned}$$

where u_B and v_B represent the averaged velocity components in the streamwise and wall normal directions respectively. We also note that the averaging procedure removes the variation of $\hat{Y}$ (and thus η) with ξ, given that $\bar{s}(\xi) = 0$.

From Figure 3.5 it is evident that as the roughness parameter increases from zero the value of the streamwise velocity component at the wall decreases, this being a direct consequence of the boundary condition (2.1.26). This is a physically sensible result as an increase in roughness would essentially result in an increase of fluid ‘slip’ at the wall. We also observe that the flow converges to the free-stream further from the wall indicating that the boundary-layer is thickened in the presence of surface roughness. We illustrate the scaled wall-normal velocity,

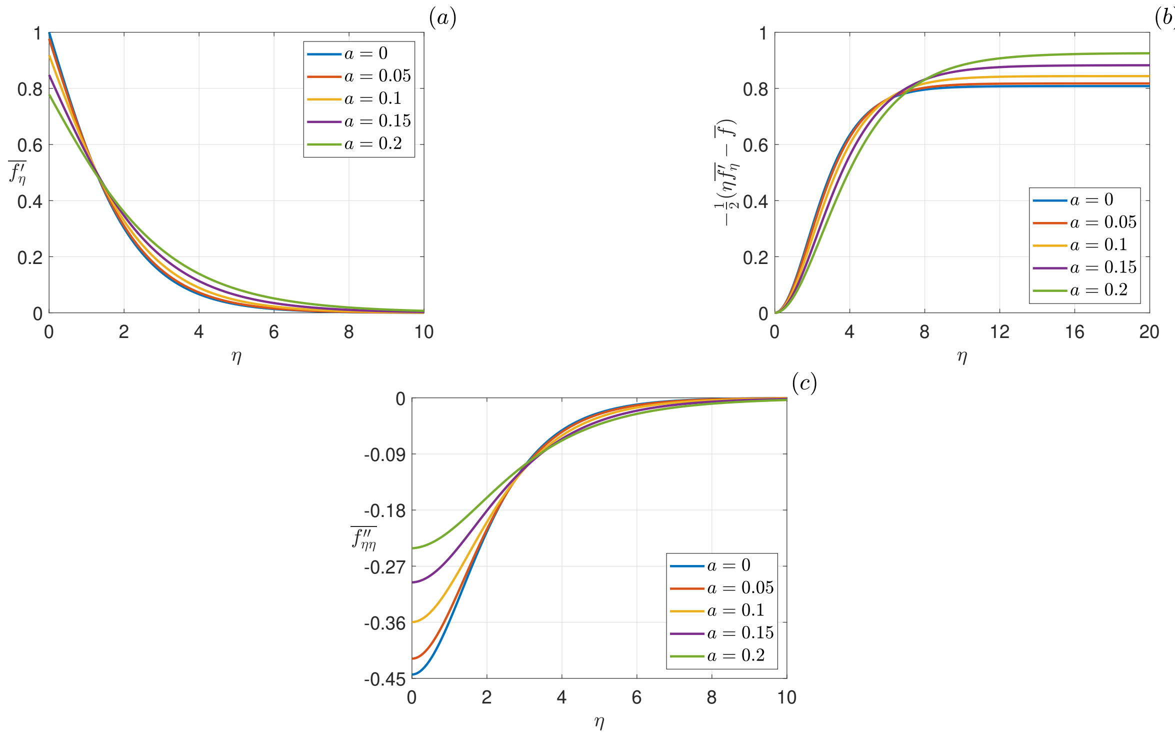

Figure 3.5: In (a) and (b) we illustrate the averaged streamwise and scaled wall-normal velocity profiles, respectively, for a range of values of the roughness parameter. In (c) we illustrate the variation of the averaged shear profiles with the boundary-layer coordinate for the same range of values of a.

$\sqrt{\xi}v_B$. Upon increasing a we find that the constant large-η value of this flow component increases in value, this result being intrinsically linked with the slow decay of the streamwise velocity profile to the far-field. Lastly, we observe that the absolute value of the shear at the wall decreases in the presence of increasing levels of surface roughness. We also find that the boundary layer thickness increases as the value of a increases. For the case when $a = 0.2$, we determine that the boundary layer thickness is as follows

$$\delta^{0.2}(x^*) \approx 9.294\sqrt{\frac{\nu^* x^*}{U_w^*}} = 9.294\frac{x^*}{\sqrt{Re_{x^*}}},$$

which is nearly a 46% increase in boundary layer thickness (here we have introduced the notation $\delta^a(x^*)$, where a is the roughness parameter). The displacement thickness for the averaged

Table 3.1: Numerical values of the basic flow parameters for a range of values of the roughness parameter a.

a	$\overline{f'_{\eta}}(0)$	$\lvert\overline{f''_{\eta\eta}}(0)\rvert$	$\overline{\delta}$
0	1	0.4437	1.6161
0.05	0.9766	0.4183	1.6354
0.1	0.9187	0.3597	1.6885
0.15	0.8479	0.2960	1.7651
0.2	0.7784	0.2413	1.8553

flow profiles is defined as follows

$$\delta^* = \int_0^{\infty} \frac{u^*}{U_w^*} \mathrm{d}y^* = \frac{x^*}{\sqrt{Re_{x^*}}} \int_0^{\infty} \overline{f'_{\eta}}(\eta)\,\mathrm{d}\eta = \frac{x^*}{\sqrt{Re_{x^*}}} \overline{\delta},$$

where $\overline{\delta} = \overline{f}(\eta = \eta_{max})$. We summarise a range of important base flow quantities in Table 3.1, and make use of these numerical values in the ensuing linear stability analyses, see Chapter 4.

Consistent with the results presented in Figure 3.4 we see that the average value of the shear at the wall decreases in absolute value as a increases. Indeed, these results give justification for our restriction that $a \leq 0.2$. As the value of the roughness parameter increases further we determine that $|\overline{f''_{\eta\eta}}(0)|$ becomes vanishingly small, an indication that the flow has indeed separated.

Within both this section and the previous section we have detailed how the flow over a translating wavy surface becomes periodic at a suitable distance downstream from the point where $\xi = 0$. As such, it would be incorrect to apply a base flow averaging procedure over *any* roughness wavelength. Rather, one must ensure that the flow has developed sufficiently far enough downstream from the initial non-periodic flow determined from the solution of (2.1.27). Failure to do so will result in the determination of flow fields that are not in fact identical after application of a spatial averaging process, and instead are skewed by the results near to the point where $\xi = 0$. Therefore, for the problem we are considering here, we computed a spatial average of the mean flow fields over one period of the roughness profile (the cosine wave) between the locations $\xi_0 = 0.5$ and $\xi_1 = 1.5$. We arrive at an identical set of results if we compute these averaged flows over any complete cycle of the roughness profile given that $\xi_0 \geq 0.5$. In fact, given that this flow is doubly periodic, completing this computation over one complete cycle of the roughness profile is, in reality, unnecessary as one arrives at the same results averaging over just one-half cycle. In an attempt to reproduce the rotating disk base flow results presented by Garrett *et al.* (2016) we applied an averaging procedure as outlined above. Given that the disk flow is periodic in exactly the same way as the flow we are considering here, we believe, is a reasonable thing to do. We find that our results disagree somewhat with those of Garrett *et al.* (2016) and that this disagreement increases as the value of the roughness parameter increases. From this we infer that Garrett *et al.* (2016) likely applied their averaging procedure over one complete roughness cycle starting from *the initial* radial location. Our results show clearly that this process cannot simply be applied over *any* roughness wavelength and postulate that the results regarding the linear stability characteristics of the flows considered by Garrett *et al.* (2016) are somewhat affected by the inaccuracies associated with the computation of their averaged mean flow profiles.

3.4 Self Similar Periodicity

In §3.2 we observed cyclical variation in the basic flow solutions using the Keller-Box approach. This motivates us to attempt to reproduce such results analytically using a suitable similarity approach. To do this we now analyse system (2.1.16) without prior knowledge of the shape of the surface profile in the case of constant wall velocity. For the interested reader, flows where the wall velocity is not constant are discussed in Appendix A. Assuming system (2.1.16) admits self similar solutions we introduce the following similarity coordinate

$$\tau = \frac{\hat{Y}}{g\sqrt{X\sigma}},$$

and the streamfunction $\phi = g\sqrt{X/\sigma}f(\tau)$, where g is a function of X to be determined. Given the definition of η and ϕ we can rewrite the $\hat{Y}$ derivative as follows

$$\frac{\partial}{\partial \hat{Y}} = \frac{\partial \tau}{\partial \hat{Y}}\frac{\partial}{\partial \tau} = g^{-1}X^{-\frac{1}{2}}\sigma^{-\frac{1}{2}}\frac{\partial}{\partial \tau}.$$

Therefore, the streamwise flow component is given by

$$u_0 = \frac{\partial \phi}{\partial \hat{Y}} = (g^{-1}X^{-\frac{1}{2}}\sigma^{-\frac{1}{2}})(gX^{\frac{1}{2}}\sigma^{-\frac{1}{2}})\frac{\partial f}{\partial \tau} = \frac{f'_\tau}{\sigma}. \tag{3.4.1}$$

Now

$$\frac{\partial \tau}{\partial X} = -\frac{\hat{Y}}{g}\frac{g'_X}{g}\frac{1}{\sigma^{\frac{1}{2}}X^{\frac{1}{2}}} - \frac{\hat{Y}}{2g}\frac{\sigma'_X}{\sigma^{\frac{3}{2}}X^{\frac{1}{2}}} - \frac{\hat{Y}}{2g}\frac{1}{X^{\frac{3}{2}}\sigma^{\frac{1}{2}}}.$$

Thus, for the X derivative we have that

$$\frac{\partial}{\partial X} = \frac{\partial \tau}{\partial X}\frac{\partial}{\partial \tau} = \tau\left(-\frac{g'_X}{g} - \frac{\sigma'_X}{2\sigma} - \frac{1}{2X}\right)\frac{\partial}{\partial \tau}.$$

Now

$$\frac{\partial \phi}{\partial X} = \left(\frac{\partial}{\partial X}gX^{\frac{1}{2}}\sigma^{-\frac{1}{2}}\right)f + (gX^{\frac{1}{2}}\sigma^{-\frac{1}{2}})\frac{\partial f}{\partial X}.$$

Therefore the wall-normal flow component becomes

$$v_0 = -\frac{\partial \phi}{\partial X} = g\sqrt{\frac{X}{\sigma}}(\tau f'_\tau H_- - fH_+), \tag{3.4.2}$$

where

$$H_\pm = \frac{g'_X}{g} + \frac{1}{2X} \pm \frac{1}{2}\left(-\frac{\sigma'_X}{\sigma}\right).$$

Given the above we have that

$$\frac{\partial u_0}{\partial X} = -\sigma^{-2}\sigma'_X f'_\tau - \sigma^{-1}\tau H_- f''_{\tau\tau}, \tag{3.4.3a}$$

$$\frac{\partial u_0}{\partial \hat{Y}} = g^{-1}X^{-\frac{1}{2}}\sigma^{-\frac{3}{2}}f''_{\tau\tau}, \tag{3.4.3b}$$

$$\frac{\partial^2 u_0}{\partial \hat{Y}^2} = g^{-2}X^{-1}\sigma^{-2}f'''_{\tau\tau\tau}. \tag{3.4.3c}$$

Substituting (3.4.3) into (2.1.16) yields

$$-Xg^2H_+ff''_{\tau\tau} = \sigma^2 f'''_{\tau\tau\tau}. \tag{3.4.4}$$

In order to be able to determine a similarity solution it must then be the case that

$$Xg^2H_+ = c_1\sigma^2. \tag{3.4.5}$$

As consequence of equation (3.4.5), we have that

$$-c_1ff''_{\tau\tau} = f'''_{\tau\tau\tau}, \tag{3.4.6}$$

where c_1 is an arbitrary constant that ensures self-similarity. On rearranging (3.4.5) we obtain

$$Xg^2\left(\frac{g'_X}{g} + \frac{1}{2X} - \frac{\sigma'_X}{2\sigma}\right) = c_1\sigma^2.$$

Now

$$gg'_X + \frac{g^2}{2X} - \frac{g^2\sigma_X}{2\sigma} = \frac{c_1\sigma^2}{X}.$$

By letting $G = g^2$ we have $G'_X = 2gg'_X$, and we obtain the following ODE

$$G'_X + G\left(\frac{1}{X} - \frac{\sigma'_X}{\sigma}\right) = \frac{k^2\sigma^2}{X},$$

where $2c_1 = k^2$. The above equation is of the form

$$G'_X + GP(X) = Q(X).$$

In order to solve the above we make use of an integrating factor. Now

$$\mathcal{K}(X) = \exp\left(\int P(X)\, dX\right) = \frac{X}{\sigma}.$$

Given this form of $\mathcal{K}(X)$, we obtain

$$\frac{d}{dX}\left[\frac{X}{\sigma}G\right] = \frac{k^2\sigma^2}{X}\frac{X}{\sigma} = k^2\sigma.$$

Integrating both sides yields

$$\frac{X}{\sigma}G = k^2\mathcal{I},$$

where

$$\mathcal{I} = \int \sigma(X)\, dX,$$

is the arc length of the wavy surface, $Y = s(X)$. Therefore we have obtained $g = k\sqrt{X^{-1}\mathcal{I}\sigma}$. From (3.4.6) we have that

$$-\frac{k^2}{2} f f''_{\tau\tau} = f'''_{\tau\tau\tau}.$$

By writing $F(\zeta) = kf(\tau)$, where $\zeta = k\tau$, we have that $F'_\zeta = f'_\tau$, $kF''_{\zeta\zeta} = f''_{\tau\tau}$, and $k^2F'''_{\zeta\zeta\zeta} = f'''_{\tau\tau\tau}$. Therefore

$$-\frac{k^2}{2}\frac{F}{k}kF''_{\zeta\zeta} = k^2F'''_{\zeta\zeta\zeta}.$$

Therefore the flow at all streamwise locations is determined from the solution of

$$F'''_{\zeta\zeta\zeta} + \frac{FF''_{\zeta\zeta}}{2} = 0, \tag{3.4.7}$$

solved subject to the conditions $F(\zeta=0)=F'_\zeta(\zeta=0)-1=0$ and $F'_\zeta(\zeta\to\infty)\to 0$. The ODE given by (3.4.7) is identical to one that describes the flow induced by the translation of a purely smooth surface. As detailed in Hanevy *et al.* (2024), the transformations derived in this Section acts to scale out any surface deformations with regards to the calculation of the basic state. Therefore in all cases when the wall velocity is constant, the boundary layer flow induced by a non-flat surface can be determined from the solutions associated with the flow over a smooth boundary. To determine the velocity components we note that

$$\zeta = k\tau = \frac{k\hat{Y}}{g\sqrt{X\sigma}} = \frac{1}{k\sqrt{X^{-1}\mathcal{I}\sigma}}\frac{k\hat{Y}}{\sqrt{X\sigma}} = \frac{\hat{Y}}{\sigma\sqrt{\mathcal{I}}}. \tag{3.4.8}$$

Given we know the form of g, ϕ becomes

$$\phi = g\sqrt{\frac{X}{\sigma}}f(\tau) = k\sqrt{X^{-1}\mathcal{I}\sigma}\sqrt{\frac{X}{\sigma}\frac{F}{k}} = \sqrt{\mathcal{I}}F. \tag{3.4.9}$$

The streamwise flow component is given as follows

$$u_0 = \frac{\partial\phi}{\partial\hat{Y}} = \frac{\partial\zeta}{\partial\hat{Y}}\frac{\partial\phi}{\partial\zeta} = \sigma^{-1}\sqrt{\mathcal{I}^{-1}}\sqrt{\mathcal{I}}F'_\zeta = \frac{F'_\zeta}{\sigma}.$$

For the wall-normal flow component we have that

$$v_0 = -\frac{\partial\phi}{\partial X} = -\frac{\partial}{\partial X}(\sqrt{\mathcal{I}}F).$$

Thus

$$v_0 = -\left(\frac{1}{2}\mathcal{I}^{-\frac{1}{2}}\sigma F + \mathcal{I}^{\frac{1}{2}}\frac{\partial F}{\partial X}\right) = \frac{\sigma}{2\sqrt{\mathcal{I}}}\left(-\frac{2\mathcal{I}}{\sigma}\frac{\partial F}{\partial X} - F\right).$$

We also have that

$$\frac{\partial F}{\partial X} = \frac{\partial\zeta}{\partial X}\frac{\partial F}{\partial\zeta} = \left(-\sigma^{-2}\sigma'_X\mathcal{I}^{-\frac{1}{2}}\hat{Y} - \frac{1}{2}\sigma^{-1}\hat{Y}\mathcal{I}^{-\frac{3}{2}}\sigma\right)F'_\zeta.$$

Therefore

$$\frac{\partial F}{\partial X} = \left(-\sigma^{-1}\sigma'_X\zeta - \frac{1}{2}\mathcal{I}^{-1}\sigma\zeta\right)F'_\zeta.$$

We have obtained the following expressions for u_0 and v_0

$$u_0 = \frac{F'_\zeta}{\sigma}, \tag{3.4.10a}$$

$$v_0 = \frac{\sigma}{2\sqrt{\mathcal{I}}}\left[\left(\frac{2\mathcal{I}\sigma'_X}{\sigma^2}+1\right)\zeta F'_\zeta - F\right]. \tag{3.4.10b}$$

Given the above it is clear to see that the solution for u_0 exhibits periodicity in the streamwise direction. Therefore the problem we are considering here indeed admits self similar solutions given that

$$\xi = X, \quad u_0 = \frac{\partial\phi}{\partial\hat{Y}}, \quad v_0 = -\frac{\partial\phi}{\partial X}, \quad \phi = \sqrt{\mathcal{I}}F(\zeta), \quad \zeta = \frac{\hat{Y}}{\sigma\sqrt{\mathcal{I}}}.$$

In order to compare our Keller-Box solutions with the self similar solution, the streamwise velocities must match, thus

$$\frac{\partial f\left(X, \frac{\hat{Y}}{\sqrt{X}}\right)}{\partial\eta} = \frac{1}{\sigma}\frac{\mathrm{d}F\left(\frac{\hat{Y}}{\sigma\sqrt{\mathcal{I}}}\right)}{\mathrm{d}\zeta}. \tag{3.4.11}$$

Hence

$$\frac{\partial^2 f\left(X, \frac{\hat{Y}}{\sqrt{X}}\right)}{\partial\eta^2} = \frac{1}{\sigma}\frac{\partial}{\partial\eta}\left[\frac{\mathrm{d}F\left(\frac{\hat{Y}}{\sigma\sqrt{\mathcal{I}}}\right)}{\mathrm{d}\zeta}\right]. \tag{3.4.12}$$

Now $\zeta = \eta\sqrt{X}/(\sigma\sqrt{\mathcal{I}})$, therefore

$$\frac{\partial}{\partial\eta} = \frac{\partial}{\partial\zeta}\frac{\partial\zeta}{\partial\eta} = \frac{\sqrt{X}}{\sigma\sqrt{\mathcal{I}}}\frac{\partial}{\partial\zeta}.$$

It transpires that

$$\frac{\partial^2 f(\xi,0)}{\partial\eta^2} = \frac{F''_{ZZ}(0)}{\sigma^2}\sqrt{\frac{X}{\mathcal{I}}} = -\frac{0.4437}{\sigma^2}\sqrt{\frac{X}{\mathcal{I}}}, \tag{3.4.13}$$

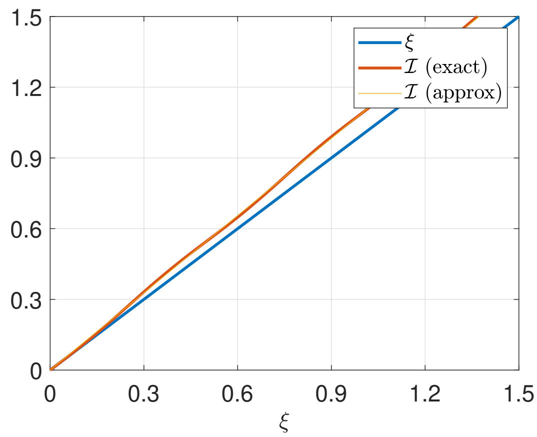

Figure 3.6: Comparison between the exact and approximate values of $\mathcal{I}$.

where the value of $F''_{\zeta\zeta}(0)$ has been determined numerically in §3.1. In the instance when $\mathcal{I} \propto X$, the shear at the wall will vary in a purely sinusoidal fashion. Given the definition of the wavy surface we are analysing here, one finds that

$$\mathcal{I} = \frac{E(2\pi X| - (2a\pi)^2)}{2\pi},$$

where $E(x|m)$ is the incomplete integral of the second kind, where integrals of this type can be found in Abromowitz & Stegun (1972). In the cases when $a \ll 1$, this integral can be very well approximated in the following manner

$$\mathcal{I} \approx \left(1 + \frac{\max(\sigma) - \min(\sigma)}{4}\right)^2 X = (1+\vartheta)^2 X,$$

where $\vartheta = [\sqrt{1+(2a\pi)^2} - 1]/4$, see Figure 3.6.

Thus, we are able to predict analytically the sinusoidal variation of the shear at the wall as follows

$$\frac{\partial^2 f(\xi,0)}{\partial \eta^2} \approx -\frac{0.4437}{(1+\vartheta)\sigma^2}. \tag{3.4.14}$$

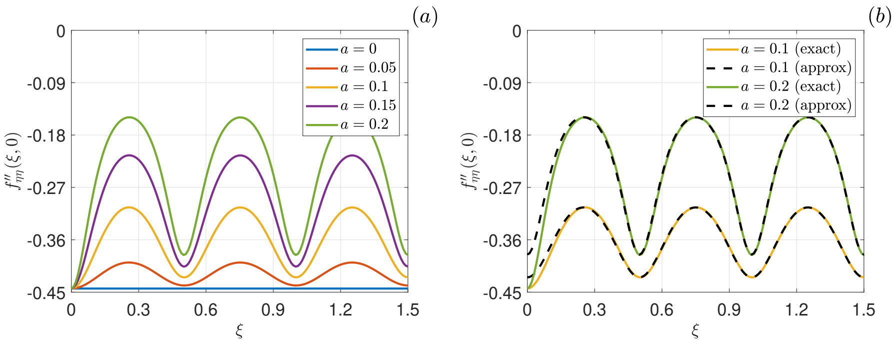

Figure 3.7: In (a) the shear at the wall, $f''_{\eta\eta}(\xi,0)$, is illustrated as a function of the streamwise coordinate ξ, for a range of values of the roughness parameter. In (b) we compare our approximate result given in (3.4.14) with the exact result arising from our numerical calculations.

Once again it is evident from Figure 3.7 that the flow is not immediately periodic as predicted by our self similar analysis. The initial flow profile must be allowed to develop downstream from the point where $\xi = 0$ before periodicity is first observed. This result is a direct consequence of the ratio $\sigma\zeta/\eta = \sqrt{X/\mathcal{I}}$, tending to a limiting constant away from the leading edge. We have also compared our approximate expression for the shear at the wall with the exact solution which gives us an indication of how far away one needs to be from the leading edge before periodicity is established. To further support the validity of our Keller box solutions equation (3.4.11) implies that the results presented in Figures 3.2 and 3.3 will be reproduced when $\sigma^{-1}F'_{\zeta}$ is plotted against $\zeta = \eta\sqrt{X}/(\sigma\sqrt{\mathcal{I}})$. By solving (3.4.7) numerically subject to the appropriate boundary conditions we demonstrate this exactly in Figure 3.8 for the case when $a = 0.2$. Not only that we can directly reproduce the averaged profiles presented in Section §3.3 by taking the average of the velocity components given by (3.4.10).

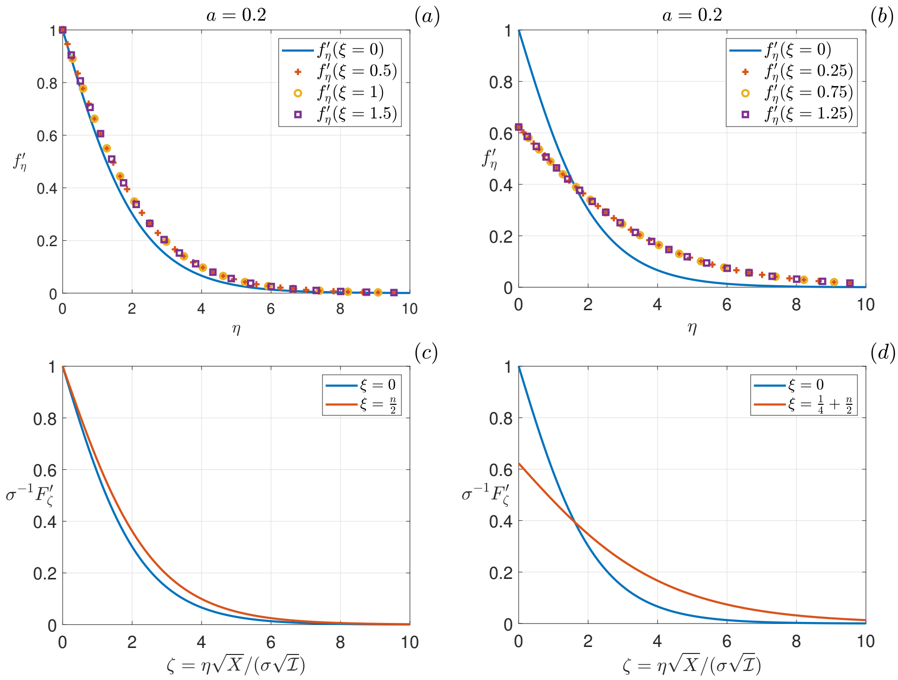

Figure 3.8: Comparison of Keller-box solutions with our self-similar analysis. Solutions are presented at the peaks and troughs of s ($\xi = \frac{n}{2}$ for $n \in \mathbb{Z}^+$), where the Keller-box solution in (a) corresponds to the self-similar solution in (c). Similarly, solutions at $\xi = \frac{1}{4} + \frac{n}{2}$ for $n \in \mathbb{Z}^+$, which represent the zeros of the wavy surface, are shown in (b) and are equivalent to the self-similar solution in (d).

In this section, we have demonstrated that the basic flow solutions presented in §3.2 are, in fact, completely periodic by adapting a suitable similarity approach. However, the initial flow profile must be allowed to develop from the point $\xi = 0$ before periodicity becomes evident. Furthermore, by employing this self-similar approach, we have successfully reproduced the basic flow solutions from §3.2 and §3.3.

Chapter 4

Linear Stability Analysis

In this Chapter we analyse the onset of linear instability of the boundary layer flow induced by a wavy surface via two means. In the first instance we follow the work of Garrett *et al.* (2016) and adopt a standard Orr-Sommerfeld approach to analyse the linear stability of our averaged flow solutions. To do this we calculate the base flows for a range of streamwise values and take the average, we proceed by determining the most dangerous eigenvalue associated with this single profile in order to determine the linear stability characteristics of the flow. In the second case we introduce what we refer to as a 'quasi-spatial' approach motivated by the studies of Morgan & Davies (2020*a*) and, Morgan *et al.* (2021*a*). Essentially the flow field is frozen in space whereby snapshots of the spatially periodic flow are analysed via the standard LSA approach. To this end we calculate the base flows for a range of streamwise values, determine the most dangerous eigenvalue associated with these single profiles and take an average of these eigenvalue results in order to determine the linear stability characteristics of the flow.

This chapter is structured as follows, in §4.1 we derive the governing perturbation equations that allow us to analyse the averaged flow profiles presented in Chapter 3 for various values of a. The resulting perturbation equations are solved utilising a Chebyshev spectral scheme which we discuss in §4.2. In §4.3 we derive the appropriate energy balance for problems of this type.

In §4.4 we present linear stability results for two-dimensional disturbances and also results from our integral energy analysis, which provides insights as to the mechanisms responsible for instability. In §4.5 we conduct a quasi-spatial linear stability analysis and compare the results owing from this methodology to those presented in §4.4.

4.1 Derivation Of The Linear Stability Equations

To derive the governing perturbation equations we make use of the 3-dimensional, time-dependent Navier-Stokes equations for an incompressible fluid in the absence of body forces which are given by

$$\frac{\partial u^*}{\partial x^*} + \frac{\partial v^*}{\partial y^*} + \frac{\partial w^*}{\partial z^*} = 0, \tag{4.1.1a}$$

$$\frac{\partial u^*}{\partial t^*} + u^*\frac{\partial u^*}{\partial x^*} + v^*\frac{\partial u^*}{\partial y^*} + w^*\frac{\partial u^*}{\partial z^*} = -\frac{1}{\rho^*}\frac{\partial p^*}{\partial x^*} + \nu^*\left(\frac{\partial^2 u^*}{\partial x^{*2}} + \frac{\partial^2 u^*}{\partial y^{*2}} + \frac{\partial^2 u^*}{\partial z^{*2}}\right), \tag{4.1.1b}$$

$$\frac{\partial v^*}{\partial t^*} + u^*\frac{\partial v^*}{\partial x^*} + v^*\frac{\partial v^*}{\partial y^*} + w^*\frac{\partial v^*}{\partial z^*} = -\frac{1}{\rho^*}\frac{\partial p^*}{\partial y^*} + \nu^*\left(\frac{\partial^2 v^*}{\partial x^{*2}} + \frac{\partial^2 v^*}{\partial y^{*2}} + \frac{\partial^2 v^*}{\partial z^{*2}}\right), \tag{4.1.1c}$$

$$\frac{\partial w^*}{\partial t^*} + u^*\frac{\partial w^*}{\partial x^*} + v^*\frac{\partial w^*}{\partial y^*} + w^*\frac{\partial w^*}{\partial z^*} = -\frac{1}{\rho^*}\frac{\partial p^*}{\partial z^*} + \nu^*\left(\frac{\partial^2 w^*}{\partial x^{*2}} + \frac{\partial^2 w^*}{\partial y^{*2}} + \frac{\partial^2 w^*}{\partial z^{*2}}\right). \tag{4.1.1d}$$

To numerically analyse the linear stability of the mean flow profiles discussed in§3.3 we non-dimensionlise with the following length, velocity, pressure, and time rescalings

$$(x,y,z) = \frac{(x^*,y^*,z^*)}{\delta^*}, \quad (u,v,w) = \frac{(u^*,v^*,w^*)}{U_w^*}, \quad p = \frac{p^*}{\rho^* U_w^{*2}}, \quad t = \frac{U_w^*}{\delta^*}t^*,$$

where the length and time scales are now expressed in terms of the displacement thickness. After non-dimensionalisation we obtain the following

$$\frac{\partial u}{\partial x}+\frac{\partial v}{\partial y}+\frac{\partial w}{\partial z}=0, \tag{4.1.2a}$$

$$\frac{\partial u}{\partial t}+u\frac{\partial u}{\partial x}+v\frac{\partial u}{\partial y}+w\frac{\partial u}{\partial z}=-\frac{\partial p}{\partial x}+\frac{1}{R}\left(\frac{\partial^2 u}{\partial x^2}+\frac{\partial^2 u}{\partial y^2}+\frac{\partial^2 u}{\partial z^2}\right), \tag{4.1.2b}$$

$$\frac{\partial v}{\partial t}+u\frac{\partial v}{\partial x}+v\frac{\partial v}{\partial y}+w\frac{\partial v}{\partial z}=-\frac{\partial p}{\partial y}+\frac{1}{R}\left(\frac{\partial^2 v}{\partial x^2}+\frac{\partial^2 v}{\partial y^2}+\frac{\partial^2 v}{\partial z^2}\right), \tag{4.1.2c}$$

$$\frac{\partial w}{\partial t}+u\frac{\partial w}{\partial x}+v\frac{\partial w}{\partial y}+w\frac{\partial w}{\partial z}=-\frac{\partial p}{\partial z}+\frac{1}{R}\left(\frac{\partial^2 w}{\partial x^2}+\frac{\partial^2 w}{\partial y^2}+\frac{\partial^2 w}{\partial z^2}\right). \tag{4.1.2d}$$

Where $R=\delta^*U_w^*/\nu^*$ is the Reynolds number based on the displacement thickness. As is standard for these types of problems, we now apply Squire's theorem, which states that if a growing three-dimensional disturbance exists, then a corresponding growing two-dimensional disturbance will exist at a lower Reynolds number. Therefore, we reduce the dimensionality of equation (4.1.2), obtaining the two-dimensional equivalent of the previously discussed three-dimensional system. For readers interested in further details and a formal proof of Squire's theorem, we refer to Ruban *et al.* (2023).

$$\frac{\partial u}{\partial x}+\frac{\partial v}{\partial y}=0, \tag{4.1.3a}$$

$$\frac{\partial u}{\partial t}+u\frac{\partial u}{\partial x}+v\frac{\partial u}{\partial y}=-\frac{\partial p}{\partial x}+\frac{1}{R}\left(\frac{\partial^2 u}{\partial x^2}+\frac{\partial^2 u}{\partial y^2}\right), \tag{4.1.3b}$$

$$\frac{\partial v}{\partial t}+u\frac{\partial v}{\partial x}+v\frac{\partial v}{\partial y}=-\frac{\partial p}{\partial y}+\frac{1}{R}\left(\frac{\partial^2 v}{\partial x^2}+\frac{\partial^2 v}{\partial y^2}\right). \tag{4.1.3c}$$

The mean flow quantities are now perturbed as follows

$$u(x,y,t) = u_B(x,y) + \tilde{u}(x,y,t), \tag{4.1.4a}$$

$$v(x,y,t) = R^{-1/2} v_B(x,y) + \tilde{v}(x,y,t), \tag{4.1.4b}$$

$$p(x,y,t) = p_B + \tilde{p}(x,y,t), \tag{4.1.4c}$$

where the perturbation quantities $(\tilde{u}, \tilde{v}, \tilde{p})$ are assumed to be small. Therefore we obtain the following linearized equations

$$\frac{\partial \tilde{u}}{\partial x} + \frac{\partial \tilde{v}}{\partial y} = 0 \tag{4.1.5a}$$

$$\frac{\partial \tilde{u}}{\partial t} + u_B \frac{\partial \tilde{u}}{\partial x} + \tilde{u}\frac{\partial u_B}{\partial x} + \tilde{v}\frac{\partial u_B}{\partial y} + R^{-\frac{1}{2}} v_B \frac{\partial \tilde{u}}{\partial y} = -\frac{\partial \tilde{p}}{\partial x} + \frac{1}{R}\left(\frac{\partial^2 \tilde{u}}{\partial x^2} + \frac{\partial^2 \tilde{u}}{\partial y^2}\right), \tag{4.1.5b}$$

$$\frac{\partial \tilde{v}}{\partial t} + u_B \frac{\partial \tilde{v}}{\partial x} + \tilde{u} R^{-\frac{1}{2}} \frac{\partial v_B}{\partial x} + v_B R^{-\frac{1}{2}} \frac{\partial \tilde{v}}{\partial y} + \tilde{v} R^{-\frac{1}{2}} \frac{\partial v_B}{\partial y} = -\frac{\partial \tilde{p}}{\partial y} + \frac{1}{R}\left(\frac{\partial^2 \tilde{v}}{\partial x^2} + \frac{\partial^2 \tilde{v}}{\partial y^2}\right). \tag{4.1.5c}$$

We now employ the standard parallel flow approximation. Having made the assumption that sufficiently far enough downstream ($x \gg 1$) the streamwise boundary layer growth is marginal, we consider u_B to be a function of y only, and v_B to be negligible. Therefore we obtain the following

$$\frac{\partial \tilde{u}}{\partial x} + \frac{\partial \tilde{v}}{\partial y} = 0, \tag{4.1.6a}$$

$$\frac{\partial \tilde{u}}{\partial t} + u_B \frac{\partial \tilde{u}}{\partial x} + \tilde{v}\frac{\mathrm{d}u_B}{\mathrm{d}y} = -\frac{\partial \tilde{p}}{\partial x} + \frac{1}{R}\left(\frac{\partial^2 \tilde{u}}{\partial x^2} + \frac{\partial^2 \tilde{u}}{\partial y^2}\right), \tag{4.1.6b}$$

$$\frac{\partial \tilde{v}}{\partial t} + u_B \frac{\partial \tilde{v}}{\partial x} = -\frac{\partial \tilde{p}}{\partial y} + \frac{1}{R}\left(\frac{\partial^2 \tilde{v}}{\partial x^2} + \frac{\partial^2 \tilde{v}}{\partial y^2}\right). \tag{4.1.6c}$$

Utilising the parallel flow approximation makes the solution to (4.1.6) separable and we now express the perturbations in terms of normal modes and write

$$[\tilde{u}(x,y,t),\tilde{v}(x,y,t),\tilde{p}(x,y,t)] = [\hat{u}(y),\hat{v}(y),\hat{p}(y)]\mathrm{e}^{\mathrm{i}(\alpha x-\omega t)},$$

where α is the wavenumber in the x-direction and ω is the disturbance frequency. Here we will be conducting a spatial analysis by fixing ω to be real, allowing us to determine the complex quantity α. The disturbances are periodic in time and grow or decay exponentially with x. By letting $\alpha = \alpha_\mathrm{r} + \mathrm{i}\alpha_\mathrm{i}$ the disturbances will grow exponentially in space if $\alpha_\mathrm{i} < 0$. On substitution of the normal modes into the linear disturbance equations we obtain the following

$$\mathrm{i}\alpha\hat{u} + \hat{v}'_y = 0, \tag{4.1.7a}$$

$$\frac{1}{R}\alpha^2\hat{u} + \mathrm{i}(\alpha u_B - \omega)\hat{u} - \frac{1}{R}\hat{u}''_{yy} + \mathrm{i}\alpha\hat{p} + (u_B)'_y\hat{v} = 0, \tag{4.1.7b}$$

$$\frac{1}{R}\alpha^2\hat{v} + \mathrm{i}(\alpha u_B - \omega)\hat{v} - \frac{1}{R}\hat{v}''_{yy} + \hat{p}'_y = 0. \tag{4.1.7c}$$

Combining the above equations we arrive at the Orr-Sommerfeld equation

$$\{(\mathrm{D}^2-\alpha^2)^2 - \mathrm{i}\alpha R[(u_B - c)(\mathrm{D}^2-\alpha^2) - (u_B)''_{yy}]\}\hat{v} = 0, \tag{4.1.8}$$

where $\mathrm{D} = \mathrm{d}/\mathrm{d}y$ and $c = \omega/\alpha$. The Orr-Sommerfeld equation is a fourth order differential equation, which upon solving would admit four linearly independent solutions. Given that the perturbation velocities are subject to the no-slip condition at the wall, and that all perturbations must decay to zero far from the surface, (4.1.7) is solved subject to

$$\hat{u}(y=0) = \hat{v}(y=0) = \hat{v}'(y=0) = 0, \tag{4.1.9a}$$

$$\hat{u}(y\to\infty) \to \hat{v}(y\to\infty) \to \hat{p}(y\to\infty) \to 0, \tag{4.1.9b}$$

where the condition on $\hat{v}'$ is a direct consequence of the continuity equation. For more details regarding the Orr-Sommerfeld equation see Ruban *et al.* (2023). The derivation of the Orr-Sommerfeld equation can be found in many introductory textbooks so the details are omitted. In order to analyse the linear stability of the averaged mean flow solutions we write $y = \overline{\delta}\eta$, and $u_B(y) = \overline{f'_\eta}(\overline{\delta}\eta)$ where $\overline{f'_\eta}$ represents the averaged basic flow solution and $\overline{\delta}$ is the associated average displacement thickness. Non-trivial solutions can be found for only specific combinations of the wavenumber α, the disturbance frequency ω, and the Reynolds number R.

4.2 Numerical Solution To The Perturbation Equations

In this section we derive the numerical scheme used to solve (4.1.7) subject to the conditions (4.1.9) using a spectral method that utilises Chebyshev polynomials. We follow the methods outlined in Griffiths *et al.* (2021). The Chebyshev polynomials are defined recursively below

$$T_0(y) = 1, \tag{4.2.1a}$$

$$T_1(y) = y, \tag{4.2.1b}$$

$$T_{k+1}(y) = 2yT_k(y) - T_{k-1}(y). \tag{4.2.1c}$$

Assuming that a function $f(y_j)$ is decomposed by Chebyshev expansions we have that

$$f(y_j) \approx \sum_{n=0}^{N} a_n T_n(y_j).$$

Equation (4.1.7) only involves second order ODEs and as a result we only require the first and second derivatives of the Chebyshev polynomials which are given as follows

$$T_0'(y) = T_0''(y) = 0, \tag{4.2.2a}$$

$$T_1'(y) = 1, \tag{4.2.2b}$$

$$T_1''(y) = 0, \tag{4.2.2c}$$

$$T_2'(y) = 4T_1(y), \tag{4.2.2d}$$

$$T_2''(y) = 4T_1'(y), \tag{4.2.2e}$$

$$T_k'(y) = 2T_{k-1}(y) + 2yT_{k-1}'(y) - T_{k-2}'(y), \tag{4.2.2f}$$

$$T_k''(y) = 4T_{k-1}' + 2yT_{k-1}''(y) - T_{k-2}''(y). \tag{4.2.2g}$$

In order to solve (4.1.7) with the aim of obtaining the eigenvalue of the streamwise wavenumber α, and the corresponding eigenfunctions of the perturbation quantities $(\hat{u}, \hat{v}, \hat{p})$, the Chebyshev expansions are introduced at a number of points in the physical domain called collocation points. To determine those points we utilise the transformation of the Gauss-Lobatto collocation points y_j which is defined like so

$$y_j = -\cos\left(\frac{j\pi}{N}\right), \tag{4.2.3}$$

for $j = 0, 1, ..., N$, so there are $N+1$ number of points in the interval $[-1, 1]$. An exponential map is used to transform the Gauss–Lobatto collocation points into the physical domain. The mapping is used to distribute 100 collocation points between the surface of the plate $\eta = 0$, to the top of the domain $\eta_{max} = 100$. This mapping allows us to capture the the exponential nature of the base flow for a range of different ϕ values and is defined like so

$$\eta_j = -\frac{1}{\phi}\ln\left(\frac{1 + y_j + A}{A}\right), \tag{4.2.4}$$

where $A = 2(\exp^{-\phi\eta_{max}} - 1)^{-1}$ and ϕ is a free constant. Other mappings have been used in the literature, for example, Appelquist & Imayama (2017) employed a linear mapping when analysing the linear stability characteristics of the flow over a rotating disk. Unless otherwise stated we set $N = 100$ and $\phi = 1/5$. Various values of ϕ were tested and we found that for values of $\phi \geq 1/5$ the solutions were assured to converge. The Chebyshev polynomials and their derivatives are obtained using the chain rule and are given as follows

$$S_k(\eta) = T_k(y), \tag{4.2.5a}$$

$$S'_k(\eta) = \frac{\mathrm{d}T_k(y)}{\mathrm{d}\eta} = T'_k(y)\frac{\mathrm{d}y}{\mathrm{d}\eta}, \tag{4.2.5b}$$

$$S''_k = \frac{\mathrm{d}^2T_k(y)}{\mathrm{d}\eta^2} = T''_k(y)\left(\frac{\mathrm{d}y}{\mathrm{d}\eta}\right)^2 + T'_k(y)\frac{\mathrm{d}^2y}{\mathrm{d}\eta^2}. \tag{4.2.5c}$$

We note that the polynomials are orthogonal functions in the domain $[-1,1]$ with respect to their defining inner product. The truncated series of the perturbation quantities $(\hat{u},\hat{v},\hat{p})$ and their derivatives at the collocation points η_j, are therefore given by

$$\hat{u}(\eta_j) = \sum_{k=0}^{N} \hat{a}_k^{\hat{u}} S_k(\eta_j), \tag{4.2.6a}$$

$$\hat{u}'(\eta_j) = \sum_{k=0}^{N} \hat{a}_k^{\hat{u}} S'_k(\eta_j), \tag{4.2.6b}$$

$$\hat{u}''(\eta_j) = \sum_{k=0}^{N} \hat{a}_k^{\hat{u}} S''_k(\eta_j). \tag{4.2.6c}$$

We obtain similar expressions for $\hat{v}$ and $\hat{p}$. We require that the perturbation quantities are zero at the surface to ensure the no slip condition is satisfied and the perturbations are equal to zero at the far end of the physical domain as disturbances vanish. Substituting the Chebyshev expansions of the perturbation quantities along with the boundary conditions into (4.1.7) leads to the generalised eigenvalue problem which is of the form

$$(A_2\alpha^2 + A_1\alpha + A_0)V = 0, \tag{4.2.7}$$

where the matrices A_2, A_1 and A_0 are of the size $3(N+1)\times 3(N+1)$ where the 3 is the number of unknowns and V is the matrix of eigenfunctions. It is important to note that eigenvalue solution methods are often prone to spurious eigenvalues, those that are not true eigenvalues of the perturbation equations. These eigenvalues are well explained by Morgan (2018) who states that such eigenvalues may be attributed to the solution method of the problem and may be either stable or unstable. Morgan (2018) highlights that stable spurious eigenvalues are of little importance, however spurious unstable eigenvalues are highly undesirable since they could incorrectly predict the onset of linear instability. There are two types of spurious eigenvalues, physically spurious eigenvalues and numerically spurious eigenvalues. Physically spurious eigenvalues are computed numerically in error because of misapplication of boundary conditions or some other misrepresentation of the physics. Numerically spurious eigenvalues are poor approximations to exact eigenvalues because the mode may be oscillating too rapidly to be resolved using a given discretisation but can always be computed accurately using a sufficiently large degree Chebyshev approximation. The matrices that constitute equation (4.2.7) are defined below, where $S_j^m = S_j(\eta_m)$.

$$A_2 = \begin{bmatrix}
\frac{S_0^0}{R} & 0 & 0 & \cdots & \frac{S_j^0}{R} & 0 & 0 & \cdots & \frac{S_N^0}{R} & 0 & 0 \\
0 & \frac{S_0^0}{R} & 0 & \cdots & 0 & \frac{S_j^0}{R} & 0 & \cdots & 0 & \frac{S_N^0}{R} & 0 \\
0 & 0 & 0 & \cdots & 0 & 0 & 0 & \cdots & 0 & 0 & 0 \\
\vdots & \vdots & \vdots & \ddots & \vdots & \vdots & \vdots & \ddots & \vdots & \vdots & \vdots \\
\frac{S_0^k}{R} & 0 & 0 & \cdots & \frac{S_j^k}{R} & 0 & 0 & \cdots & \frac{S_N^k}{R} & 0 & 0 \\
0 & \frac{S_0^k}{R} & 0 & \cdots & 0 & \frac{S_j^k}{R} & 0 & \cdots & 0 & \frac{S_N^k}{R} & 0 \\
0 & 0 & 0 & \cdots & 0 & 0 & 0 & \cdots & 0 & 0 & 0 \\
\vdots & \vdots & \vdots & \ddots & \vdots & \vdots & \vdots & \ddots & \vdots & \vdots & \vdots \\
\frac{S_0^N}{R} & 0 & 0 & \cdots & \frac{S_j^N}{R} & 0 & 0 & \cdots & \frac{S_N^N}{R} & 0 & 0 \\
0 & \frac{S_0^N}{R} & 0 & \cdots & 0 & \frac{S_j^N}{R} & 0 & \cdots & 0 & \frac{S_N^N}{R} & 0 \\
0 & 0 & 0 & \cdots & 0 & 0 & 0 & \cdots & 0 & 0 & 0
\end{bmatrix}$$

$$
A_1 = \begin{bmatrix}
iu_B S_0^0 & 0 & iS_0^0 & \cdots & iu_B S_j^0 & 0 & iS_j^0 & \cdots & iu_B S_N^0 & 0 & iS_N^0 \\
-i\omega S_0^0 - \frac{S_0''^0}{R} & u_B' S_0^0 & 0 & \cdots & -i\omega S_j^0 - \frac{S_j''^0}{R} & u_B' S_j^0 & 0 & \cdots & -i\omega S_N^0 - \frac{S_N''^0}{R} & u_B' S_N^0 & 0 \\
iS_0^0 & 0 & 0 & \cdots & iS_j^0 & 0 & 0 & \cdots & iS_N^0 & 0 & 0 \\
\vdots & \vdots & \vdots & \ddots & \vdots & \vdots & \vdots & \ddots & \vdots & \vdots & \vdots \\
iu_B S_0^k & 0 & iS_0^k & \cdots & iu_B S_j^k & 0 & iS_j^k & \cdots & iu_B S_N^k & 0 & iS_N^k \\
-i\omega S_0^k - \frac{S_0''^k}{R} & u_B' S_0^k & 0 & \cdots & -i\omega S_j^k - \frac{S_j''^k}{R} & u_B' S_j^k & 0 & \cdots & -i\omega S_N^k - \frac{S_N''^k}{R} & u_B' S_N^k & 0 \\
iS_0^k & 0 & 0 & \cdots & iS_j^k & 0 & 0 & \cdots & iS_N^k & 0 & 0 \\
\vdots & \vdots & \vdots & \ddots & \vdots & \vdots & \vdots & \ddots & \vdots & \vdots & \vdots \\
iu_B S_0^N & 0 & iS_0^N & \cdots & iu_B S_j^N & 0 & iS_j^N & \cdots & iu_B S_N^N & 0 & iS_N^N \\
-i\omega S_0^N - \frac{S_0''^N}{R} & u_B' S_0^N & 0 & \cdots & -i\omega S_j^N - \frac{S_j''^N}{R} & u_B' S_j^N & 0 & \cdots & -i\omega S_N^N - \frac{S_N''^N}{R} & u_B' S_N^N & 0 \\
iS_0^N & 0 & 0 & \cdots & iS_j^N & 0 & 0 & \cdots & iS_N^N & 0 & 0
\end{bmatrix},
$$

$$
A_0 = \begin{bmatrix}
-i\omega S_0^0 - \frac{S_0''^0}{R} & u_B' S_0^0 & 0 & \cdots & -i\omega S_j^0 - \frac{S_j''^0}{R} & u_B' S_j^0 & 0 & \cdots & -i\omega S_N^0 - \frac{S_N''^0}{R} & u_B' S_N^0 & 0 \\
0 & -i\omega S_0^0 - \frac{S_0''^0}{R} & S_0'^0 & \cdots & 0 & -i\omega S_j^0 - \frac{S_j''^0}{R} & S_j'^0 & \cdots & 0 & -i\omega S_N^0 - \frac{S_N''^0}{R} & S_N'^0 \\
0 & S_0'^0 & 0 & \cdots & 0 & S_j'^0 & 0 & \cdots & 0 & S_N'^0 & 0 \\
\vdots & \vdots & \vdots & \ddots & \vdots & \vdots & \vdots & \ddots & \vdots & \vdots & \vdots \\
-i\omega S_0^k - \frac{S_0''^k}{R} & u_B' S_0^k & 0 & \cdots & -i\omega S_j^k - \frac{S_j''^k}{R} & u_B' S_j^k & 0 & \cdots & -i\omega S_N^k - \frac{S_N''^k}{R} & u_B' S_N^k & 0 \\
0 & -i\omega S_0^k - \frac{S_0''^k}{R} & S_0'^k & \cdots & 0 & -i\omega S_j^k - \frac{S_j''^k}{R} & S_j'^k & \cdots & 0 & -i\omega S_N^k - \frac{S_N''^k}{R} & S_N'^k \\
0 & S_0'^k & 0 & \cdots & 0 & S_j'^k & 0 & \cdots & 0 & S_N'^k & 0 \\
\vdots & \vdots & \vdots & \ddots & \vdots & \vdots & \vdots & \ddots & \vdots & \vdots & \vdots \\
-i\omega S_0^N - \frac{S_0''^N}{R} & u_B' S_0^N & 0 & \cdots & -i\omega S_j^N - \frac{S_j''^N}{R} & u_B' S_j^N & 0 & \cdots & -i\omega S_N^N - \frac{S_N''^N}{R} & u_B' S_N^N & 0 \\
0 & -i\omega S_0^N - \frac{S_0''^N}{R} & S_0'^N & \cdots & 0 & -i\omega S_j^N - \frac{S_j''^N}{R} & S_j'^N & \cdots & 0 & -i\omega S_N^N - \frac{S_N''^N}{R} & S_N'^N \\
0 & S_0'^N & 0 & \cdots & 0 & S_j'^N & 0 & \cdots & 0 & S_N'^N & 0
\end{bmatrix},
$$

and

$$V = \begin{bmatrix} \hat{a}_0^{\hat{u}} \\ \hat{a}_0^{\hat{v}} \\ \hat{a}_0^{\hat{p}} \\ \vdots \\ \hat{a}_j^{\hat{u}} \\ \hat{a}_j^{\hat{v}} \\ \hat{a}_j^{\hat{p}} \\ \vdots \\ \hat{a}_N^{\hat{u}} \\ \hat{a}_N^{\hat{v}} \\ \hat{a}_N^{\hat{p}} \end{bmatrix}.$$

The eigenvalue problem was solved using Matlab's polyeig function using our known averaged basic flow solutions by prescribing R and ω. Our numerical scheme was verified against the familiar neutral stability results of the Blasius boundary-layer problem. It was found that the critical values were $R_{\text{crit}} = 519.1$, $\alpha_{\text{crit}} = 0.3044$, and $\omega_{\text{crit}} = 0.1208$, which are in excellent agreement with the results of Schmid & Henningson (2001), for example.

4.3 Derivation Of Energy Balance Equations

In an attempt to better understand the mechanisms of the instability we consider the energy balance of the system. In order to derive an appropriate integral energy analysis for this problem we multiply the streamwise and wall-normal perturbation equations (4.1.6) by $\tilde{u}$ and $\tilde{v}$, respectively and take the sum which yields

$$\left(\frac{\partial}{\partial t} + u_B\frac{\partial}{\partial x}\right)\tilde{q} + \tilde{u}\tilde{v}\frac{\mathrm{d}u_B}{\mathrm{d}y} = -\frac{\partial(\tilde{u}\tilde{p})}{\partial x} - \frac{\partial(\tilde{v}\tilde{p})}{\partial y} + \frac{1}{R}\left(\tilde{u}\frac{\partial^2\tilde{u}}{\partial x^2} + \tilde{v}\frac{\partial^2\tilde{v}}{\partial x^2} + \tilde{u}\frac{\partial^2\tilde{u}}{\partial y^2} + \tilde{v}\frac{\partial^2\tilde{v}}{\partial y^2}\right). \quad (4.3.1)$$

Equation (4.3.1) represents the energy transfer processes of the system where $\tilde{q} = (\tilde{u}^2 + \tilde{v}^2)/2$ is the kinetic energy of the two disturbances. We can rewrite (4.3.1) as follows

$$\left(\frac{\partial}{\partial t} + u_B \frac{\partial}{\partial x}\right)\tilde{q} + \tilde{u}\tilde{v}\frac{\mathrm{d}u_B}{\mathrm{d}y} = -\frac{\partial(\tilde{u}\tilde{p})}{\partial x} - \frac{(\tilde{v}\tilde{p})}{\partial y} + \frac{1}{R}\left(\frac{\partial(\tilde{v}\tilde{\Omega})}{\partial x} - \frac{\partial(\tilde{u}\tilde{\Omega})}{\partial y} - \tilde{\Omega}^2\right), \tag{4.3.2}$$

where

$$\tilde{\Omega} = \frac{\partial \tilde{v}}{\partial x} - \frac{\partial \tilde{u}}{\partial y},$$

represents the disturbance vorticity perpendicular to the plane of motion. To see that the final term in (4.3.2) is correct let

$$C = \frac{\partial(\tilde{v}\tilde{\Omega})}{\partial x} - \frac{\partial(\tilde{u}\tilde{\Omega})}{\partial y} - \tilde{\Omega}^2.$$

Given the definition of $\tilde{\Omega}$ we obtain

$$C = \tilde{u}\frac{\partial^2 \tilde{u}}{\partial y^2} + \tilde{v}\frac{\partial^2 \tilde{v}}{\partial x^2} - \tilde{v}\frac{\partial^2 \tilde{u}}{\partial x \partial y} - \tilde{u}\frac{\partial^2 \tilde{v}}{\partial x \partial y}.$$

From the continuity equation we have that

$$\frac{\partial \tilde{u}}{\partial x} = -\frac{\partial \tilde{v}}{\partial y}. \tag{4.3.3}$$

Differentiating (4.3.3) with respect to x and multiplying by $\tilde{u}$ yields

$$\tilde{u}\frac{\partial^2 \tilde{u}}{\partial x^2} = -\tilde{u}\frac{\partial^2 \tilde{v}}{\partial x \partial y}.$$

Differentiating (4.3.3) with respect to y and multiplying by $\tilde{v}$ yields

$$\tilde{v}\frac{\partial^2 \tilde{v}}{\partial y^2} = -\tilde{v}\frac{\partial^2 \tilde{u}}{\partial x \partial y}.$$

Therefore C becomes

$$C = \tilde{u}\frac{\partial^2 \tilde{u}}{\partial x^2} + \tilde{v}\frac{\partial^2 \tilde{v}}{\partial x^2} + \tilde{u}\frac{\partial^2 \tilde{u}}{\partial y^2} + \tilde{v}\frac{\partial^2 \tilde{v}}{\partial y^2}.$$

Which verifies the final term in equation (4.3.2). On returning to equation (4.3.2) we average over one time period, and integrate across the boundary layer. Having done so we arrive at the governing integral energy equation for flows of this nature

$$\begin{aligned}\frac{\partial}{\partial x}\left[\int_0^\infty (u_B\tilde{q})\mathrm{d}y + \int_0^\infty (\tilde{u}\tilde{p})\mathrm{d}y - \frac{1}{R}\int_0^\infty (\tilde{v}\tilde{\Omega})\mathrm{d}y\right] &= -(\tilde{v}\tilde{p})|_{y=0} - \int_0^\infty \frac{\mathrm{d}u_B}{\mathrm{d}y}(\tilde{u}\tilde{v})\mathrm{d}y \\ &\quad - \frac{(\tilde{u}\tilde{\Omega})|_{y=0}}{R} - \frac{1}{R}\int_0^\infty \tilde{\Omega}^2\mathrm{d}y,\end{aligned} \tag{4.3.4}$$

On numerical investigation one finds that the term $R^{-1}\tilde{v}\tilde{\Omega}$ is negligible and that this result is independent of the roughness parameter a. In terms of the normal modes one finds that

$$\begin{aligned}\frac{\partial}{\partial x}\left[e^{2\mathrm{i}(\alpha x-\omega t)}\left(\int_0^\infty (u_B\hat{q})\mathrm{d}y + \int_0^\infty (\hat{u}\hat{p})\mathrm{d}y\right)\right] &= -e^{2\mathrm{i}(\alpha x-\omega t)}\int_0^\infty \frac{\mathrm{d}u_B}{\mathrm{d}y}(\hat{u}\hat{v})\mathrm{d}y \\ &\quad - \frac{1}{R}e^{2\mathrm{i}(\alpha x-\omega t)}\int_0^\infty \hat{\Omega}^2\mathrm{d}y,\end{aligned}$$

where $\hat{\Omega} = \mathrm{i}\alpha\hat{v} - \hat{u}'$. Now

$$2\mathrm{i}\alpha\left[\int_0^\infty (u_B\hat{q})\mathrm{d}y + \int_0^\infty (\hat{u}\hat{p})\mathrm{d}y\right] = -\int_0^\infty \frac{\mathrm{d}u_B}{\mathrm{d}y}(\hat{u}\hat{v})\mathrm{d}y - \frac{1}{R}\int_0^\infty \hat{\Omega}^2\mathrm{d}y.$$

Given that $\alpha = \alpha_\mathrm{r} + \mathrm{i}\alpha_i$ we obtain

$$2\mathrm{i}(\alpha_\mathrm{r} + \mathrm{i}\alpha_i)\left[\int_0^\infty (u_B\hat{q})\mathrm{d}y + \int_0^\infty (\hat{u}\hat{p})\mathrm{d}y\right] = -\int_0^\infty \frac{\mathrm{d}u_B}{\mathrm{d}y}(\hat{u}\hat{v})\mathrm{d}y - \frac{1}{R}\int_0^\infty \hat{\Omega}^2\mathrm{d}y.$$

Taking the real part yields

$$2\alpha_{\mathrm{i}}\left[\int_0^\infty u_B\langle\hat{q}\rangle\mathrm{d}y+\int_0^\infty\langle\hat{u}\hat{p}\rangle\mathrm{d}y\right]=\int_0^\infty\frac{\mathrm{d}u_B}{\mathrm{d}y}\langle\hat{u}\hat{v}\rangle\mathrm{d}y+\frac{1}{R}\int_0^\infty\langle\hat{\Omega}^2\rangle\mathrm{d}y.$$

Thus

$$2\alpha_{\mathrm{i}}\sim\frac{\int_0^\infty\frac{\mathrm{d}u_B}{\mathrm{d}y}\langle\hat{u}\hat{v}\rangle\mathrm{d}y+\frac{1}{R}\int_0^\infty\langle\hat{\Omega}^2\rangle\mathrm{d}y}{\int_0^\infty(u_B\langle\hat{q}\rangle+\langle\hat{u}\hat{p}\rangle)\mathrm{d}y}. \tag{4.3.5}$$

Normalising the above by the integral of the combination of energy flux and the work done by pressure yields

$$\underbrace{2\alpha_{\mathrm{i}}}_{\text{TME}}\sim\underbrace{\int_0^\infty\frac{\mathrm{d}u_B}{\mathrm{d}y}\langle\hat{u}\hat{v}\rangle\mathrm{d}y}_{\text{EPRS}}+\underbrace{\frac{1}{R}\int_0^\infty\langle\hat{\Omega}^2\rangle\mathrm{d}y}_{\text{EDAV}}, \tag{4.3.6}$$

where $\langle\hat{a}\hat{b}\rangle=\hat{a}\hat{b}^\star+\hat{a}^\star\hat{b}$ and * denotes the complex conjugate. Here TME relates to the Total Mechanical Energy of a given disturbance. The term EPRS represents the Energy Production due to Reynolds Stresses and will always be positive. The Energy Dissipation due to the Action of Viscosity is denoted EDAV and will always be negative. When the value of the term EPRS is greater than the absolute value of the EDAV term the right-hand side of the above is positive which implies that $\alpha_{\mathrm{i}}<0$ which is consistent with our definition of the criterion for linear instability.

4.4 Linear Stability Analysis - Numerical Solutions

We begin by solving (4.1.7) subject to the boundary conditions (4.1.9) for various values of the roughness parameter a. To visualise our results we cycle through a range of values of ω and R in order to determine points where $\alpha_{\mathrm{i}}\leq 0$. The points where $\alpha_{\mathrm{i}}=0$ are the neutrally stable points. In the first instance we aim to reproduce the results presented by Tsou *et al.* (1966) who analysed the linear stability of a continuous moving surface in the case of a smooth boundary. Those authors showed that the flow is linearly unstable above a critical Reynolds number $R_{\text{crit}}=3600$. Here we determine that the critical Reynolds number for the smooth boundary, i.e., in

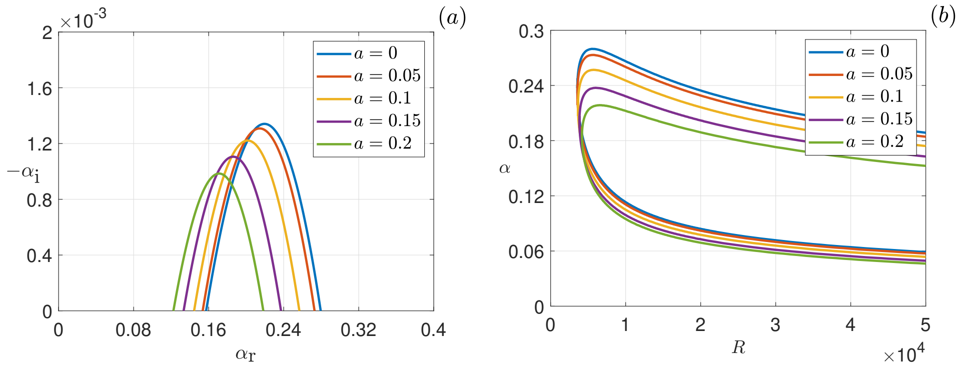

Figure 4.1: In (a) the growth rate, defined as $-\alpha_i$, is illustrated against α_r for a range of values of the roughness parameter a at a fixed value of the Reynolds number $R = R_{\text{crit}} \times 1.5$. In (b) the neutral stability curves, all the points where $\alpha_i = 0$, are illustrated for a range of values of the roughness parameter a.

the case when $a = 0$, is $R_{\text{crit}} = 3564.01$ (see Table 4.1). We argue that the numerical scheme used in the present analysis is far more accurate than the finite difference scheme used by Tsou *et al.* (1966) which explains the discrepancy in the results. For example, in their study Tsou *et al.* (1966) quote the critical Reynolds number for the Blasius boundary layer problem to be $R_{\text{crit}} = 530$, this is again an overprediction of the classical result. We expect that these slight inaccuracies are simply a function of the computing resources that were available at the time that Tsou, Sparrow and Kurtz's calculations were performed. We note here that the critical Reynolds number associated with a boundary layer flow that is developing as a result of the translation of a smooth surface is considerably larger than that of the Blasius flow problem. Tsou *et al.* (1966) argue that this increase in the value of R_{crit} is a consequence of the critical layer for these types of problems being much closer to the wall when compared to the equivalent Blasius result. Increasing the value of the parameter a we find that the addition of surface roughness has a stabilising effect on the boundary layer flow both in terms of the onset of linear instability and the growth rates of the associated disturbances. In Figure 4.1 we present the growth rates for a range of values of the roughness parameter a at a fixed Reynolds number $R = R_{\text{crit}} \times 1.5$. We find that the amplitude of the growth rate is significantly reduced which suggests stabilisation. This stabilisation is also observed as the area encompassed by the neutral curve is noticeably

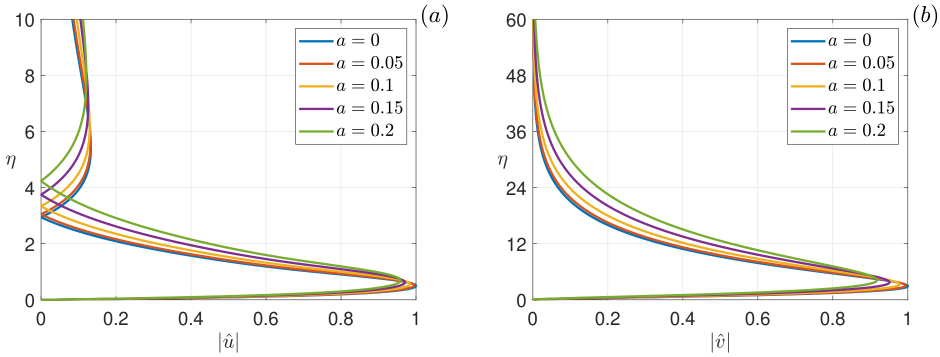

Figure 4.2: Plots of the streamwise and wall-normal eigenfuncions for a range of values of the roughness parameter a at a fixed value of the Reynolds number, $R = R_{\text{crit}} \times 1.5$. In each case the most unstable eigenmode $(\alpha_{\text{i}} = \max(\alpha_{\text{i}}))$ is selected. All the results have been normalised with respect to the maximum value at $a = 0$.

Table 4.1: Critical values for the onset of linear instability for various values of the roughness parameter.

a	R_{crit}	α_{crit}	ω_{crit}
0	3564.01	0.2367	0.1736
0.05	3571.43	0.2311	0.1655
0.1	3640.48	0.2173	0.1466
0.15	3836.58	0.2007	0.1255
0.2	4177.80	0.1846	0.1066

reduced upon increasing a. Essentially, this means there are fewer wavenumbers susceptible to linear stability as the level of surface roughness is increased. Before discussing the results associated with the integral energy analysis it proves useful to first determine the form of the eigenfunctions. In Figure 4.2 we illustrate $|\hat{u}|$, and $|\hat{v}|$ for a range of values of the roughness parameter. We observe that the peak of the wall-normal eigenfunction is reduced as a increases and similarly for the streamwise eigenfunction, which provides supporting evidence for the observed stabilisation. In Figure 4.3 we present the three energy contribution terms highlighted in (4.3.6). We observe that the energy production decreases with increasing a. The absolute value of the energy dissipation due to viscosity follows a similar trend and, as such, the total mechanical energy of the system decreases with increasing a. This result is entirely consistent with the conclusions drawn from our neutral stability curve predictions.

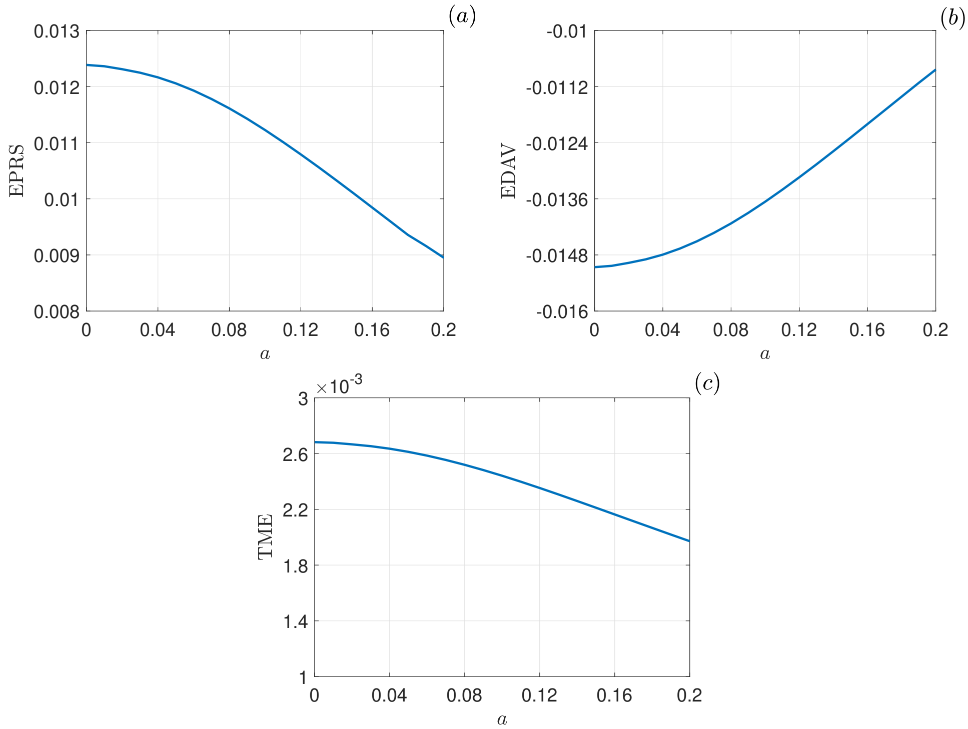

Figure 4.3: In (a) we plot the variation of the energy production due to Reynolds stresses versus a. In (b) we plot the variation of the energy dissipation due to the action of viscosity. In (c) we plot the variation of the total mechanical energy. The integrals as defined in (4.3.6) are computed at a fixed Reynolds number $R = R_{\text{crit}} \times 1.5$ where the most unstable eigenmode is selected.

4.5 Linear Stability Analysis - Quasi-Spatial Approach

Given the problem we are considering here has many analogies with the aforementioned studies of Morgan and coworkers we now conduct a quasi-spatial analysis. As we have already shown, the flow profiles we determined in Chapter 3 are periodic in space, not time. As such, we choose to employ a frozen flow-type analysis whereby we freeze the flow in space, removing the spatial dependence from the problem. By treating the base flow to be quasi-steady Morgan & Davies (2020*b*) were able to determine that the temporal variation of the complex-valued radial wavenumber, calculated over a full cycle of the base state oscillation, forms a closed loop. Taking the average of each of these solutions that forms the loop then gives a sin-

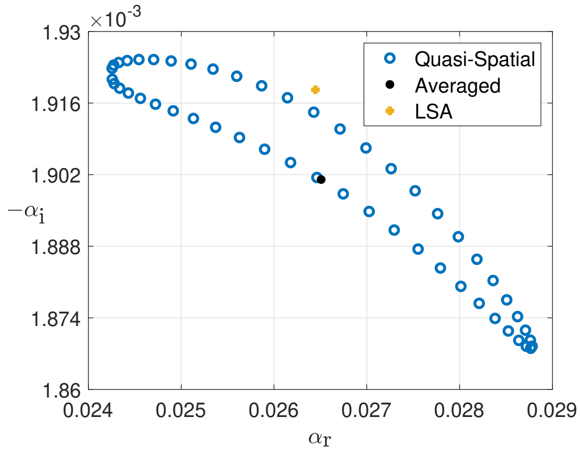

Figure 4.4: The spatial evolution of the streamwise wavenumber over a one-half cycle of the roughness wavelength. In this instance the disturbance frequency and Reynolds number are set equal to $\omega = 0.02$, and $R = 10000$, respectively. The roughness parameter is fixed such that $a = 0.1$. The black marker indicates an average of all the quasi-spatial points given in blue. As a point of reference the equivalent LSA result is indicated by the yellow marker.

gle eigenvalue that determines the growth or decay of a perturbation for a given combination of disturbance frequency and value of the Reynolds number. Fascinatingly, Morgan *et al.* (2021*b*) show that this procedure reproduces the results one would obtain from a much more computationally expensive Floquet analysis (see Figure 8(a) of Morgan *et al.* (2021*b*) for a presentation of this result) almost exactly.

We present in Figure 4.4 evidence that over one-half cycle of the wavelength period (since the flow is doubly periodic) we obtain a very similar closed-loop structure for the variation of the complex-valued streamwise wavenumber α. Indeed, for the same fixed combination of ω and R, we find that an identical closed-loop structure is evident for any choice of streamwise values given that, at least one half-cycle of the wavelength has been traversed, and that the calculation begins sufficiently far enough downstream from the initial point where $\xi = 0$. These restrictions are consistent with the arguments we present in Chapter 3.

If the analysis we present in §4.4. can be summarised as; 'calculate base flows over a range of streamwise values, average these flow profiles and then calculate the most dangerous eigenvalue associated with this single profile in order to determine the linear stability characteristics

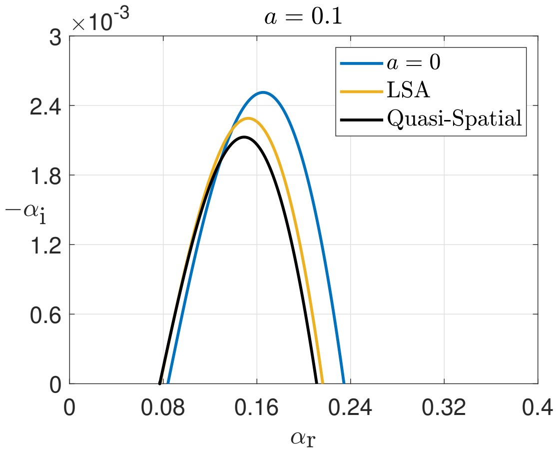

Figure 4.5: The growth rate plotted against α_r using both the LSA approach and quasi-spatial approach for $a = 0.1$. In both cases the Reynolds number is fixed at $R = 20000$. The smooth surface LSA result has been included as a point of reference.

.

of the flow', the analysis we present here is summarised as follows; 'calculate base flows over a range of streamwise values, determine the most dangerous eigenvalue associated with each flow profile and then average these results to determine the linear stability characteristics of the flow'. This procedure is essentially identical to the quasi-steady methodology presented by Morgan & Davies (2020*b*) with the expectation that our problem is quasi-spatial in nature.

In the limit as $a \to 0$ the aforementioned processes produce identical results given that the base flow is, in this instance, purely self-similar. However, as we increase the value of the roughness parameter from zero we observe a marginal difference between the results predicted by our previous LSA and the results owing from this quasi-spatial (QS) approach. In order to characterise the quasi-spatial results we determine growth rates and neutral stability curves thus allowing for comparisons to be made with the LSA results presented in §4.4. In Figure 4.5 we plot, from both approaches, the disturbance growth rate at a fixed value of the Reynolds number for a non-zero value of the roughness parameter. One can readily observe the fact that the maximum growth rate is marginally reduced when comparing the QS results with our previous LSA results. Importantly, the overall trend that increasing the value of a diminishes the growth

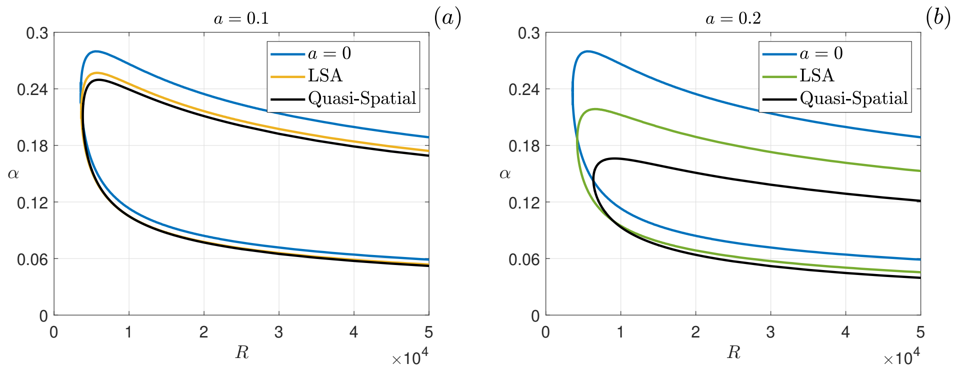

Figure 4.6: Neutral stability curves owing from both the LSA and quasi-spatial approaches. In (a) we plot the results for the case when $a = 0.1$, and in (b) for the case when $a = 0.2$. The smooth surface LSA result has been included as a point of reference.

of the disturbances remains a consistent conclusion across both analyses. In Figure 4.6 we present curves of neutral stability for both the LSA and QS approaches for two fixed values of the roughness parameter. In both cases we observe that the prediction for the lower branch of the neutral stability curve is largely unaffected. As expected, we see that as the value of a increases so the difference between the results of the two approaches becomes more apparent. For all cases considered here, we find that the QS method always predicts a larger critical Reynolds number when compared to the equivalent LSA results and that the area encompassed by the neutral stability curve effectively decreases. This reduction in area is primarily associated with a downward shift of the upper branch of the neutral stability curve. Most importantly, the results from the QS analysis support our LSA findings. Indeed, one can readily conclude that the QS findings predict an even greater level of boundary-layer stabilisation when compared to our initial LSA results.

Chapter 5

Linear Stability Analysis - Large Reynolds Number Asymptotics

Having established that averaged surface roughness has a stabilising effect on the flow we are now in a position to verify our numerical findings. To do this we proceed by conducting a large Reynolds number asymptotic analysis. An analysis of this nature has been performed for various flow configurations. For instance, Smith (1979) conducted an asymptotic analysis at large Reynolds numbers for the Blasius boundary layer, incorporating non-parallel effects. Smith (1979) successfully identified the lower branch of the neutral curve, demonstrating improved alignment with the experimental observations reported by Schubauer & Skramstad (1948). Hall (1986) performed a large Reynolds number asymptotic analysis to study the stationary modes of instability in the boundary layer on a rotating disk, demonstrating satisfactory agreement with the numerical results of Malik (1986), who used the standard LSA approach. Our approach aligns closely with the methodology presented by Griffiths *et al.* (2021), which investigated the boundary layer flow induced by a linear stretching sheet. In their work, the authors found excellent agreement between the asymptotic results and numerical solutions. In this chapter, we compare our asymptotic approximations with our previous numerical solutions obtained using the standard Linear Stability Analysis (LSA), as discussed in §4.4. Notably, an asymptotic analysis for flows of this type has not been undertaken, even for the case of a smooth boundary. Our primary focus is on examining the structure of Tollmien-Schlichting (TS) waves within the near-wall viscous layer. Since the most amplified TS disturbances occur near the lower branch of the neutral curve, this motivates us to validate our numerical findings through a lower branch asymptotic analysis rather than focusing on the upper branch. We begin by analysing the Orr-Sommerfeld equation (4.1.8) in the limit as $R \to \infty$ for neutrally stable solutions. In the limit as $R \to \infty$ we obtain Rayleigh's equation

$$(u_B - c)(\mathrm{D}^2\hat{v} - \alpha^2\hat{v}) - (u_B)''_{yy}\hat{v} = 0,$$

where $c = \omega/\alpha$. The above equation holds away from the fixed wall and the critical layer where $u_B = c$. However, in these two regions viscous effects cannot be ignored and, when $R \gg 1$, (4.1.8) is approximated as follows

$$\mathrm{D}^4\hat{v} \approx \mathrm{i}\alpha R(u_B - c)\mathrm{D}^2\hat{v}. \tag{5.0.1}$$

Close to the wall we can rewrite the basic flow u_B as follows

$$u_B = \overline{f'}(0) + \overline{f''}(0)\eta + \frac{\overline{f'''}(0)}{2}\eta^2 + \cdots,$$

where we have applied a Taylor series expansion around the point $\eta = 0$. Therefore the base flow can be approximated like so

$$u_B \approx \overline{f'}(0) - \lambda(X)\hat{Y}, \tag{5.0.2}$$

where $\lambda(X) = -\overline{f''}(0)X^{-\frac{1}{2}}$. Applying a similar approach for the wall normal velocity we obtain

$$v_B \approx \lambda'_X(X)\hat{Y}^2/2.$$

To determine the thickness of the wall layer we substitute (5.0.2) into (5.0.1) which yields

$$D^4\hat{v} \sim i\alpha R\left(\overline{f'}(0) - c - \lambda\hat{Y}\right)D^2\hat{v}.$$

By letting the thickness of the wall layer be of $\mathcal{O}(\hat{\delta})$ and writing $\hat{Y} = \hat{\delta}\overline{Y}$ we have that

$$\frac{1}{\hat{\delta}^4} \sim i\alpha R\left(\overline{f'}(0) - c - \lambda\hat{\delta}\overline{Y}\right)\frac{1}{\hat{\delta}^2}.$$

Rearranging for $\hat{\delta}$ at leading order we obtain

$$\hat{\delta} \sim \left(\alpha R\left(\overline{f'}(0) - c\right)\right)^{-\frac{1}{2}},$$

therefore the thickness of the wall layer is $\mathcal{O}\left(\alpha R\left(\overline{f'}(0) - c\right)\right)^{-\frac{1}{2}}$, where we note that $\overline{f'_\eta}(0) \leq 1$. The critical layer is located at $Y = Y_c$ where $u_B(Y_c) = c$. Expanding u_B about $Y = Y_c$ using a Taylor series gives

$$u_B \approx c + (Y - Y_c)u'_B + \cdots,$$

making use of (5.0.1) yields the following

$$D^4\hat{v} \sim i\alpha R((Y - Y_c)u'_B)D^2\hat{v}.$$

By writing $Y = Y_c + \hat{\delta}\overline{Y}$ we obtain

$$\frac{1}{\hat{\delta}^4} \sim \alpha R\hat{\delta}\overline{Y}u'_B\frac{1}{\hat{\delta}^2},$$

where u'_B is of $\mathcal{O}(1)$. Therefore we determine the thickness of the critical layer to be $\mathcal{O}((\alpha R)^{-1/3})$. On the lower branch of the stability curve, the wall layer and the critical layer merge. Here, close to the wall, $u_B \approx \overline{f'}(0) - \lambda \hat{Y}$. If $u_B = c$ this gives

$$\hat{Y} = \frac{1}{\lambda}\left(\overline{f'}(0) - c\right).$$

Balancing this $\hat{Y}$ with the wall layer thickness and ignoring the higher order term $\hat{\delta}\overline{Y}$ yields

$$\frac{1}{\lambda}\left(\overline{f'}(0) - c\right) \sim \left(\alpha R\left(\overline{f'}(0) - c\right)\right)^{-\frac{1}{2}}.$$

Therefore

$$\frac{1}{\lambda}\left(\overline{f'}(0) - c\right) \sim (\alpha R)^{-\frac{1}{3}}.$$

For the above to hold we approximate c like so

$$c \sim \overline{f'}(0) + \hat{c},$$

were $\hat{c} \sim (\alpha R)^{-\frac{1}{3}}$. Analysis of the Blasius boundary layer reveals that $\alpha \sim R^{-\frac{1}{4}}$, where full details can be found in Ruban *et al.* (2023). The analysis we present here is similar to work presented by Griffiths *et al.* (2021), where a large Reynolds number asymptotic analysis was conducted for boundary layer flows induced by a linear stretching sheet where again one finds that $\alpha \sim R^{-\frac{1}{4}}$. Now

$$c = \frac{\omega}{\alpha} \approx \overline{f'}(0) + \mathcal{O}(R^{-\frac{1}{4}}).$$

Which implies that $\omega \sim R^{-\frac{1}{4}}$ since $c \sim \mathcal{O}(1)$, hence $\alpha \sim \omega \sim R^{-\frac{1}{4}}$. In addition to this, our numerical solutions exhibit the behaviour $(\overline{f'_\eta}(0) - c) \sim R^{-1/4}$. For the ensuing asymptotic analysis, it is convenient to non-dimensionalise lengths with respect to the reference length-scale L^*, thus meaning that the dimensionless parameter upon which this analysis is based is

Re, not R. We perform a local stability analysis about the streamwise location x for $Re \gg 1$. The relationship between this Reynolds number and the local Reynolds number used in the numerical analysis is then $R = \overline{\delta}\sqrt{xRe}$. To see this we note that

$$R = \overline{\delta} x^{\frac{1}{2}} Re^{\frac{1}{2}} = \delta^* \sqrt{\frac{\rho^* U_w^*}{\mu^* x^*}} x^{\frac{1}{2}} \sqrt{\frac{U_w^* \rho^* L^*}{\mu^*}} = \frac{\delta^* U_w^*}{\nu^*}.$$

We note that the ratio of the different length scales is $L^*/\delta^* = Re^{1/2}$, and the ratio of the different time scales is $(L^* t/U_w^*)/(\delta^* t/U_w^*) = L^*/\delta^* = Re^{1/2}$. We let α_n and ω_n denote the wavenumber and frequency of the numerical formulation and α_a and ω_a denote the corresponding terms in the asymptotic formulation. We then have that $\alpha_a = (L^*/\delta^*)\alpha_n$, which gives $\alpha_a \sim Re^{1/2} Re^{-1/8} = Re^{3/8}$. Similarly we have that $\omega_a \sim Re^{3/8}$. Then, in terms of Re, the streamwise and spanwise length scales and the timescale, are $\mathcal{O}(Re^{-3/8})$. Also, the thickness of the wall layer is then $\mathcal{O}(Re^{-1/2} Re^{-1/8}) = \mathcal{O}(Re^{-5/8})$. We introduce scaled coordinates and time to reflect these scales. For convenience, we set $\varepsilon = Re^{-1/8}$, and write

$$x = 1 + \varepsilon^3 \chi, \quad t = \varepsilon^3 \tau.$$

Having carefully considered the appropriate asymptotic scales we are now in a position to analyse the problem and compare our results with our numerical findings. Unlike the LSA approach we do not make any assumptions about the parallel (or not) nature of the basic flow. As such, and in order to ensure that the following analysis is more easily tractable, we present the linear disturbance equations relevant to the asymptotic problem below

$$\frac{\partial \tilde{u}}{\partial x} + \frac{\partial \tilde{v}}{\partial y} = 0, \tag{5.0.3a}$$

$$\left(\frac{\partial}{\partial t} + u_B \frac{\partial}{\partial x}\right)\tilde{u} + \left(\tilde{u}\frac{\partial}{\partial x} + \tilde{v}\frac{\partial}{\partial y}\right)u_B + Re^{-1/2} v_B \frac{\partial \tilde{u}}{\partial y} = -\frac{\partial \tilde{p}}{\partial x}$$

$$+\frac{1}{Re}\left(\frac{\partial^2\tilde{u}}{\partial x^2}+\frac{\partial^2\tilde{u}}{\partial y^2}\right), \tag{5.0.3b}$$

$$\left(\frac{\partial}{\partial t}+u_B\frac{\partial}{\partial x}\right)\tilde{v}+Re^{-1/2}\left(\tilde{u}\frac{\partial}{\partial x}+\tilde{v}\frac{\partial}{\partial y}\right)v_B+Re^{-1/2}v_B\frac{\partial\tilde{v}}{\partial y}=-\frac{\partial\tilde{p}}{\partial y}$$
$$+\frac{1}{Re}\left(\frac{\partial^2\tilde{v}}{\partial x^2}+\frac{\partial^2\tilde{v}}{\partial y^2}\right). \tag{5.0.3c}$$

5.1 Triple Deck Structure

Similar to the analysis presented by Griffiths *et al.* (2021) we find that we have a triple deck structure where the timescale that the disturbances develop over is equal to the streamwise lengthscale. The main deck covers the full extent of the boundary layer. The upper deck is inviscid and is required so that the disturbances tend to zero in the far field. The lower deck is required to satisfy the viscous no-slip boundary conditions of the moving surface. We have an upper deck of thickness $\mathcal{O}(Re^{-3/8})$, a main deck of thickness $\mathcal{O}(Re^{-1/2})$, and a lower deck of thickness $\mathcal{O}(Re^{-5/8})$. We consider normal mode solutions and assume the perturbations are proportional to

$$E=\exp[\mathrm{i}(\theta(\chi)-\omega\tau)].$$

The wavenumber θ is a slowly varying function of x that satisfies

$$\frac{\mathrm{d}\theta}{\mathrm{d}\chi}=\alpha=\alpha_1(x)+\varepsilon\alpha_2(x)+\cdots,$$

whereas the frequency

$$\omega=\omega_1+\varepsilon\omega_2+\cdots,$$

is constant. We begin our analysis in the main deck where $y=\varepsilon^4\hat{Y}$, with $\hat{Y}=\mathcal{O}(1)$ and the disturbances expand as

$$\tilde{u}=(u_1+\varepsilon u_2+\cdots)E, \tag{5.1.1a}$$

$$\tilde{v} = (\varepsilon v_1 + \varepsilon^2 v_2 + \cdots)E, \tag{5.1.1b}$$

$$\tilde{p} = (\varepsilon p_1 + \varepsilon^2 p_2 + \cdots)E. \tag{5.1.1c}$$

Here u_i, v_i and p_i are functions of $\hat{Y}$ and the slow variable x. Taking the relevant asymptotic scalings in the main deck and substituting those into the continuity equation (5.0.3a) we arrive at

$$\frac{1}{\varepsilon^3}\frac{\partial \tilde{u}}{\partial \chi} + \frac{\partial \tilde{u}}{\partial x} + \frac{1}{\varepsilon^4}\frac{\partial \tilde{v}}{\partial \hat{Y}} = 0.$$

Substitution of (5.1.1) into (5.0.3a) yields the following expansion

$$\begin{aligned}&\frac{1}{\varepsilon^3}\mathrm{i}(\alpha_1 + \varepsilon\alpha_2 + \cdots)(u_1 + \varepsilon u_2 + \cdots) + \frac{\partial}{\partial x}(u_1 + \varepsilon u_2 + \cdots)\\ &+ \frac{1}{\varepsilon^4}\frac{\partial}{\partial \hat{Y}}(\varepsilon v_1 + \varepsilon^2 v_2 + \cdots) = 0.\end{aligned}$$

Now expanding the above we arrive at

$$\begin{aligned}&\frac{1}{\varepsilon^3}\mathrm{i}(\alpha_1 u_1 + \varepsilon\alpha_1 u_2 + \varepsilon\alpha_2 u_1 + \varepsilon^2\alpha_2 u_2 + \cdots) + \frac{\partial}{\partial x}(u_1 + \varepsilon u_2 + \cdots)\\ &+ \frac{1}{\varepsilon^4}\frac{\partial}{\partial \hat{Y}}(\varepsilon v_1 + \varepsilon^2 v_2 + \cdots) = 0.\end{aligned}$$

Collecting terms of $\mathcal{O}(\varepsilon^{-3})$ we obtain the following equation

$$\mathrm{i}\alpha_1 u_1 + \frac{\partial v_1}{\partial \hat{Y}} = 0.$$

Following the process outlined above for the x momentum equation. The relevant PDE in terms of the asymptotic scales is given as follows

$$\begin{aligned}&\frac{1}{\varepsilon^3}\frac{\partial \tilde{u}}{\partial \tau} + \frac{\partial \tilde{u}}{\partial t} + u_B\left(\frac{1}{\varepsilon^3}\frac{\partial \tilde{u}}{\partial \chi} + \frac{\partial \tilde{u}}{\partial x}\right) + \tilde{u}\frac{\partial u_B}{\partial x}\\ &+ \frac{\tilde{v}}{\varepsilon^4}\frac{\partial u_B}{\partial \hat{Y}} + \frac{\varepsilon^4 v_B}{\varepsilon^4}\frac{\partial \tilde{u}}{\partial \hat{Y}} = -\frac{1}{\varepsilon^3}\frac{\partial \tilde{p}}{\partial \chi} - \frac{\partial \tilde{p}}{\partial x}\end{aligned}$$

$$+\varepsilon^8\left(\frac{1}{\varepsilon^6}\frac{\partial^2\tilde{u}}{\partial\chi^2}+\frac{2}{\varepsilon^3}\frac{\partial^2\tilde{u}}{\partial x\partial\chi}+\frac{\partial^2\tilde{u}}{\partial x^2}+\frac{1}{\varepsilon^8}\frac{\partial^2\tilde{u}}{\partial\hat{Y}^2}\right).$$

Substitution of (5.1.1) into (5.0.3b) we arrive at

$$\begin{aligned}
&\frac{1}{\varepsilon^3}(-\mathrm{i}\omega_1-\varepsilon\mathrm{i}\omega_2-\cdots)(u_1+\varepsilon u_2+\cdots)+\frac{\partial}{\partial t}(u_1+\varepsilon u_2+\cdots)\\
&+u_B\left[\frac{1}{\varepsilon^3}\mathrm{i}(\alpha_1+\varepsilon\alpha_2+\cdots)(u_1+\varepsilon u_2+\cdots)+\frac{\partial}{\partial x}(u_1+\varepsilon u_2+\cdots)\right]\\
&+(u_1+\varepsilon u_2+\cdots)\frac{\partial u_B}{\partial x}+\frac{(\varepsilon v_1+\varepsilon^2 v_2+\cdots)}{\varepsilon^4}\frac{\mathrm{d}u_B}{\mathrm{d}\hat{Y}}+v_B\frac{\partial}{\partial\hat{Y}}(u_1+\varepsilon u_2+\cdots)\\
&=-\frac{1}{\varepsilon^3}\mathrm{i}(\alpha_1+\varepsilon\alpha_2+\cdots)(\varepsilon p_1+\varepsilon^2 p_2+\cdots)-\frac{\partial}{\partial x}(\varepsilon p_1+\varepsilon^2 p_2+\cdots)\\
&-\varepsilon^2(\alpha_1+\varepsilon\alpha_2+\cdots)^2(u_1+\varepsilon u_2+\cdots)+2\varepsilon^5\frac{\partial}{\partial x}\mathrm{i}(\alpha_1+\varepsilon\alpha_2+\cdots)(u_1+\varepsilon u_2+\cdots)\\
&+\varepsilon^8\frac{\partial^2}{\partial x^2}(u_1+\varepsilon u_2+\cdots)+\frac{\partial^2}{\partial\hat{Y}^2}(u_1+\varepsilon u_2+\cdots).
\end{aligned}$$

Expanding the above we have that

$$\begin{aligned}
&\frac{1}{\varepsilon^3}(-\mathrm{i}\omega_1u_1-\varepsilon\mathrm{i}\omega_1u_2-\varepsilon\mathrm{i}\omega_2u_1-\varepsilon^2\mathrm{i}\omega_2u_2+\cdots)+\frac{\partial}{\partial t}(u_1+\varepsilon u_2+\cdots)\\
&+u_B\left[\frac{1}{\varepsilon^3}\mathrm{i}(\alpha_1u_1+\varepsilon\alpha_1u_2+\varepsilon\alpha_2u_1+\varepsilon^2\alpha_2u_2+\cdots)+\frac{\partial}{\partial x}(u_1+\varepsilon u_2+\cdots)\right]\\
&+(u_1+\varepsilon u_2+\cdots)\frac{\partial u_B}{\partial x}+\frac{(\varepsilon v_1+\varepsilon^2 v_2+\cdots)}{\varepsilon^4}\frac{\mathrm{d}u_B}{\mathrm{d}\hat{Y}}+v_B\frac{\partial}{\partial\hat{Y}}(u_1+\varepsilon u_2+\cdots)\\
&=-\frac{1}{\varepsilon^3}\mathrm{i}(\varepsilon\alpha_1p_1+\varepsilon^2\alpha_1p_2+\varepsilon^2\alpha_2p_1+\varepsilon^3\alpha_2p_2+\cdots)\\
&-\frac{\partial}{\partial x}(\varepsilon p_1+\varepsilon^2 p_2+\cdots)-\varepsilon^2(\alpha_1+\varepsilon\alpha_2+\cdots)^2(u_1+\varepsilon u_2+\cdots)\\
&+2\varepsilon^5\mathrm{i}(\alpha_1+\varepsilon\alpha_2+\cdots)\frac{\partial}{\partial x}(u_1+\varepsilon u_2+\cdots)+\varepsilon^8\frac{\partial^2}{\partial x^2}(u_1+\varepsilon u_2+\cdots)\\
&+\frac{\partial^2}{\partial\hat{Y}^2}(u_1+\varepsilon u_2+\cdots).
\end{aligned}$$

Collecting terms of order $\mathcal{O}(\varepsilon^{-3})$ yields the following equation

$$-\mathrm{i}\omega_1u_1+\mathrm{i}\alpha_1u_1u_B+\frac{\mathrm{d}u_B}{\mathrm{d}\hat{Y}}v_1=0.$$

Following a similar process for the y momentum equation. The relevant PDE in terms of the asymptotic scales is given as follows

$$\frac{1}{\varepsilon^3}\frac{\partial \tilde{v}}{\partial \tau}+\frac{\partial \tilde{v}}{\partial t}+u_B\left(\frac{1}{\varepsilon^3}\frac{\partial \tilde{v}}{\partial \chi}+\frac{\partial \tilde{v}}{\partial x}\right)+\varepsilon^4\frac{\partial v_B}{\partial x}+\frac{\varepsilon^4 v_B}{\varepsilon^4}\frac{\partial \tilde{v}}{\partial \hat{Y}}+\frac{\varepsilon^4 \tilde{v}}{\varepsilon^4}\frac{\partial v_B}{\partial \hat{Y}}=-\frac{1}{\varepsilon^4}\frac{\partial \tilde{p}}{\partial \hat{Y}}$$
$$+\varepsilon^8\left(\frac{1}{\varepsilon^6}\frac{\partial^2 \tilde{v}}{\partial \chi^2}+\frac{2}{\varepsilon^3}\frac{\partial^2 \tilde{v}}{\partial x \partial \chi}+\frac{\partial^2 \tilde{v}}{\partial x^2}+\frac{1}{\varepsilon^8}\frac{\partial^2 \tilde{v}}{\partial \hat{Y}^2}\right).$$

Substitution of (5.1.1) into (5.0.3c) yields

$$\frac{1}{\varepsilon^3}(-\mathrm{i}\omega_1-\varepsilon\mathrm{i}\omega_2+\cdots)(\varepsilon v_1+\varepsilon^2 v_2+\cdots)+\frac{\partial}{\partial t}(\varepsilon v_1+\varepsilon^2 v_2+\cdots)$$
$$+u_B\left[\frac{1}{\varepsilon^3}\mathrm{i}(\alpha_1+\varepsilon\alpha_2+\cdots)(\varepsilon v_1+\varepsilon^2 v_2+\cdots)+\frac{\partial}{\partial x}(\varepsilon v_1+\varepsilon^2 v_2+\cdots)\right]$$
$$+\varepsilon^4(u_1+\varepsilon u_2+\cdots)\frac{\partial v_B}{\partial x}+v_B\frac{\partial}{\partial \hat{Y}}(\varepsilon v_1+\varepsilon^2 v_2+\cdots)+(\varepsilon v_1+\varepsilon^2 v_2+\cdots)\frac{\partial v_B}{\partial \hat{Y}}$$
$$=-\frac{1}{\varepsilon^4}\frac{\partial}{\partial \hat{Y}}(\varepsilon p_1+\varepsilon^2 p_2+\cdots)-\varepsilon^2(\alpha_1+\varepsilon\alpha_2+\cdots)^2(\varepsilon v_1+\varepsilon^2 v_2+\cdots)$$
$$+2\varepsilon^5\mathrm{i}(\alpha_1+\varepsilon\alpha_2+\cdots)\frac{\partial}{\partial x}(\varepsilon v_1+\varepsilon^2 v_2+\cdots)$$
$$+\varepsilon^8\frac{\partial^2}{\partial x^2}(\varepsilon v_1+\varepsilon^2 v_2+\cdots)+\frac{\partial^2}{\partial \hat{Y}^2}(\varepsilon v_1+\varepsilon^2 v_2+\cdots).$$

Expanding the above yields

$$\frac{1}{\varepsilon^3}(-\varepsilon\mathrm{i}\omega_1 v_1-\varepsilon^2\mathrm{i}\omega_1 v_2-\varepsilon^2\mathrm{i}\omega_2 v_1-\varepsilon^3\mathrm{i}\omega_2 v_2-\cdots)+\frac{\partial}{\partial t}(\varepsilon v_1+\varepsilon^2 v_2+\cdots)$$
$$+u_B\left[\frac{1}{\varepsilon^3}\mathrm{i}(\varepsilon\alpha_1 v_1+\varepsilon^2\alpha_1 v_2+\varepsilon^2\alpha_2 v_1+\varepsilon^3\alpha_2 v_2+\cdots)+\frac{\partial}{\partial x}(\varepsilon v_1+\varepsilon^2 v_2+\cdots)\right]$$
$$+\varepsilon^4(u_1+\varepsilon u_2+\cdots)\frac{\partial v_B}{\partial x}+v_B\frac{\partial}{\partial \hat{Y}}(\varepsilon v_1+\varepsilon^2 v_2+\cdots)+(\varepsilon v_1+\varepsilon^2 v_2+\cdots)\frac{\partial v_B}{\partial \hat{Y}}$$
$$=-\frac{1}{\varepsilon^4}\frac{\partial}{\partial \hat{Y}}(\varepsilon p_1+\varepsilon^2 p_2+\cdots)-\varepsilon^2(\alpha_1+\varepsilon\alpha_2+\cdots)(\varepsilon v_2+\varepsilon^2 v_2+\cdots)$$
$$+2\varepsilon^5\mathrm{i}(\alpha_1+\varepsilon\alpha_2+\cdots)\frac{\partial}{\partial x}(\varepsilon v_1+\varepsilon^2 v_2+\cdots)$$
$$+\varepsilon^8\frac{\partial^2}{\partial x^2}(\varepsilon v_1+\varepsilon^2 v_2+\cdots)+\frac{\partial^2}{\partial \hat{Y}^2}(\varepsilon v_1+\varepsilon^2 v_2+\cdots).$$

The pressure term which is of $\mathcal{O}(\varepsilon^{-3})$ dominates all the terms in the above expression and we obtain

$$\frac{\partial p_1}{\partial \hat{Y}} = 0.$$

Therefore at leading order we obtain the following equations for the main deck

$$\mathrm{i}\alpha_1 u_1 + \frac{\partial v_1}{\partial \hat{Y}} = 0, \tag{5.1.2a}$$

$$-\mathrm{i}\omega_1 u_1 + \mathrm{i}\alpha_1 u_1 u_B + \frac{du_B}{d\hat{Y}} v_1 = 0, \tag{5.1.2b}$$

$$\frac{\partial p_1}{\partial \hat{Y}} = 0. \tag{5.1.2c}$$

We can readily see that that $p_1 = p_1(x)$. Rearranging (5.1.2a) for u_1 and substituting into (5.1.2b) yields

$$\left(\frac{\omega_1}{\alpha_1} - u_B\right)\frac{\partial v_1}{\partial \hat{Y}} + \frac{du_B}{d\hat{Y}} v_1 = 0.$$

On separating variables we obtain

$$\frac{1}{v_1}\frac{\partial v_1}{\partial \hat{Y}} = \frac{\frac{\mathrm{d}u_B}{\mathrm{d}\hat{Y}}}{u_B - \frac{\omega_1}{\alpha_1}}.$$

Integrating both sides yields

$$\ln v_1 = \ln\left(u_B - \frac{\omega_1}{\alpha_1}\right) + A(x),$$

where $A(x)$ is an arbitrary integration function. Therefore we have that

$$v_1 = \left(u_B - \frac{\omega_1}{\alpha_1}\right) e^{A(x)}.$$

For convenience let

$$e^{A(x)} = \mathrm{i}B_0(x)\alpha_1.$$

Therefore

$$v_1 = \mathrm{i}B_0(x)(u_B\alpha_1 - \omega_1). \tag{5.1.3}$$

On making use of v_1 and (5.1.2a) we obtain

$$u_1 = -B_0(x)\frac{du_B}{dY}.$$

Therefore

$$v_1 = \mathrm{i}B_0(x)(\alpha_1 u_B - \omega_1), \tag{5.1.4a}$$

$$u_1 = -B_0(x)\frac{du_B}{d\hat{Y}}, \tag{5.1.4b}$$

$$p_1 = p_1(x), \tag{5.1.4c}$$

where $p_1(x)$ and $B_0(x)$ are unknown slowly varying amplitude functions. Recalling the far-field condition on u_B, i.e., $u_B \to 0$, as $\hat{Y} \to \infty$, we obtain

$$u_1 \to 0, \quad v_1 \to -\mathrm{i}\omega_1 B_0.$$

Close to the wall we have that $u_B \to (\overline{f'_\eta}(0) - \lambda\hat{Y})$, as $\hat{Y} \to 0$, therefore

$$u_1 \to \lambda B_0, \quad v_1 \to \mathrm{i}B_0(\alpha_1\overline{f'}(0) - \omega_1) - \mathrm{i}B_0\alpha_1\lambda\hat{Y}.$$

From the scalings we have that $\alpha_1\overline{f'_\eta}(0) = \omega_1$. This choice stipulates that the critical layer, where $u_B = \omega/(\alpha\overline{f'_\eta}(0))$, moves to the wall at leading order. This is analogous to the analysis for the flow induced by a linear stretching sheet, see Griffiths *et al.* (2021).

An upper deck is required to reduce the disturbances to zero as $\hat{Y} \to \infty$. In the upper deck $y = \varepsilon^3\bar{y}$, with $\bar{y} = \mathcal{O}(1)$. Of interest here is the matching of the wall-normal velocities between the upper and the main deck. Here

$$\tilde{u} = (\varepsilon\overline{u}_1 + \varepsilon^2\overline{u}_2 + \cdots)E, \tag{5.1.5a}$$

$$\tilde{v} = (\varepsilon\overline{v}_1 + \varepsilon^2\overline{v}_2 + \cdots)E, \tag{5.1.5b}$$

$$\tilde{p} = (\varepsilon\overline{p}_1 + \varepsilon^2\overline{p}_2 + \cdots)E. \tag{5.1.5c}$$

Here the basic flow $u_B \to 0$ and at leading order v_B is negligible. Following the process used in the analysis of the main deck and taking the relevant asymptotic scalings we obtain the following continuity equation

$$\frac{1}{\varepsilon^3}\frac{\partial\tilde{u}}{\partial\chi} + \frac{\partial\tilde{u}}{\partial x} + \frac{1}{\varepsilon^3}\frac{\partial\tilde{v}}{\partial\overline{y}} = 0.$$

Substitution of (5.1.5) into (5.0.3a) we arrive at

$$\frac{1}{\varepsilon^3}\mathrm{i}(\alpha_1 + \varepsilon\alpha_2 + \cdots)(\varepsilon\overline{u}_1 + \varepsilon^2\overline{u}_2 + \ldots) + \frac{\partial}{\partial x}(\varepsilon\overline{u}_1 + \varepsilon^2\overline{u}_2 + \cdots)$$
$$+ \frac{1}{\varepsilon^3}\frac{\partial}{\partial\overline{y}}(\varepsilon\overline{v}_1 + \varepsilon^2\overline{v}_2 + \cdots) = 0.$$

Expanding the above yields

$$\frac{1}{\varepsilon^3}\mathrm{i}(\varepsilon\alpha_1\overline{u}_1 + \varepsilon^2\alpha_1\overline{u}_2 + \varepsilon^2\alpha_2\overline{u}_1 + \varepsilon^3\alpha_2\overline{u}_2 + \cdots) + \frac{\partial}{\partial x}(\varepsilon\overline{u}_1 + \varepsilon^2\overline{u}_2 + \cdots)$$
$$+ \frac{1}{\varepsilon^3}\frac{\partial}{\partial\overline{y}}(\varepsilon\overline{v}_1 + \overline{v}_2 + \cdots) = 0.$$

Collecting terms of $\mathcal{O}(\varepsilon^{-2})$ we arrive at

$$\mathrm{i}\alpha_1\overline{u}_1 + \frac{\partial\overline{v}_1}{\partial\overline{y}} = 0.$$

The relevant PDE for the x momentum equation in terms of the asymptotic scales is give as follows

$$\frac{1}{\varepsilon^3}\frac{\partial \tilde{u}}{\partial \tau}+\frac{\partial \tilde{u}}{\partial t}=-\frac{1}{\varepsilon^3}\frac{\partial \tilde{p}}{\partial \chi}-\frac{\partial \tilde{p}}{\partial x}+\varepsilon^8\left(\frac{1}{\varepsilon^6}\frac{\partial^2 \tilde{u}}{\partial \chi^2}+\frac{2}{\varepsilon^3}\frac{\partial^2 \tilde{u}}{\partial x\partial \chi}+\frac{\partial^2 \tilde{u}}{\partial x^2}+\frac{1}{\varepsilon^6}\frac{\partial^2 \tilde{u}}{\partial \overline{y}^2}\right).$$

Substitution of (5.1.5) into (5.0.3b) yields

$$\begin{aligned}
&\frac{1}{\varepsilon^3}(-\mathrm{i}\omega_1-\varepsilon\mathrm{i}\omega_2-\cdots)(\varepsilon\overline{u}_1+\varepsilon^2\overline{u}_2+\cdots)+\frac{\partial}{\partial t}(\varepsilon\overline{u}_1+\varepsilon^2\overline{u}_2+\cdots)\\
&=-\frac{1}{\varepsilon^3}\mathrm{i}(\alpha_1+\varepsilon\alpha_2+\cdots)(\varepsilon\overline{p}_1+\varepsilon^2\overline{p}_2+\cdots)-\frac{\partial}{\partial x}(\varepsilon\overline{p}_1+\varepsilon^2\overline{p}_2+\cdots)\\
&-\varepsilon^2(\alpha_1+\varepsilon\alpha_2+\cdots)^2(\varepsilon\overline{u}_1+\varepsilon^2\overline{u}_2+\cdots)+2\varepsilon^5\mathrm{i}(\alpha_1+\varepsilon\alpha_2+\cdots)\frac{\partial}{\partial x}(\varepsilon\overline{u}_1+\varepsilon^2\overline{u}_2+\cdots)\\
&+\varepsilon^8\frac{\partial^2}{\partial x^2}(\varepsilon\overline{u}_1+\varepsilon^2\overline{u}_2+\cdots)+\varepsilon^2\frac{\partial^2}{\partial \overline{y}^2}(\varepsilon\overline{u}_1+\varepsilon^2\overline{u}_2+\cdots).
\end{aligned}$$

Expanding the above yields

$$\begin{aligned}
&\frac{1}{\varepsilon^3}(-\varepsilon\mathrm{i}\omega_1\overline{u}_1-\varepsilon^2\mathrm{i}\omega_1\overline{u}_2-\varepsilon^2\mathrm{i}\omega_2\overline{u}_1-\varepsilon^3\mathrm{i}\omega_2\overline{u}_1)+\frac{\partial}{\partial t}(\varepsilon\overline{u}_1+\varepsilon^2\overline{u}_2+\ldots)\\
&=-\frac{1}{\varepsilon^3}\mathrm{i}(\varepsilon\alpha_1\overline{p}_1+\varepsilon^2\alpha_1\overline{p}_2+\varepsilon\alpha_2\overline{p}_1+\varepsilon^3\alpha_2\overline{p}_2)-\frac{\partial}{\partial x}(\varepsilon\overline{p}_1+\varepsilon^2\overline{p}_2+\ldots)\\
&-\varepsilon^2(\alpha_1+\varepsilon\alpha_2+\cdots)^2(\varepsilon\overline{u}_1+\varepsilon^2\overline{u}_2+\cdots)+2\varepsilon^5\mathrm{i}(\alpha_1+\varepsilon\alpha_2+\cdots)\frac{\partial}{\partial x}(\varepsilon\overline{u}_1+\varepsilon^2\overline{u}_2+\cdots)\\
&+\varepsilon^8\frac{\partial^2}{\partial x^2}(\varepsilon\overline{u}_1+\varepsilon^2\overline{u}_2+\cdots)+\varepsilon^2\frac{\partial^2}{\partial \overline{y}^2}(\varepsilon\overline{u}_1+\varepsilon^2\overline{u}_2+\cdots).
\end{aligned}$$

Collecting terms of $\mathcal{O}(\varepsilon^{-2})$ we arrive at

$$-\mathrm{i}\omega_1\overline{u}_1=-\mathrm{i}\alpha_1\overline{p}_1.$$

The y momentum equation in terms of asymptotic scales is given as follows

$$\frac{1}{\varepsilon^3}\frac{\partial \tilde{v}}{\partial \tau}+\frac{\partial \tilde{v}}{\partial t}=-\frac{1}{\varepsilon^3}\frac{\partial \tilde{p}}{\partial \overline{y}}+\varepsilon^8\left(\frac{1}{\varepsilon^6}\frac{\partial^2 \tilde{v}}{\partial \chi^2}+\frac{2}{\varepsilon^3}\frac{\partial^2 \tilde{v}}{\partial x\partial \chi}+\frac{\partial^2 \tilde{v}}{\partial x^2}+\frac{1}{\varepsilon^6}\frac{\partial^2 \tilde{v}}{\partial \overline{y}^2}\right).$$

Substitution of (5.1.5) into (5.0.3c) yields

$$
\begin{aligned}
&\frac{1}{\varepsilon^3}(-\mathrm{i}\omega_1-\varepsilon-\mathrm{i}\omega_2-\cdots)(\varepsilon\overline{v}_1+\varepsilon^2\overline{v}_2+\cdots)+\frac{\partial}{\partial t}(\varepsilon\overline{v}_1+\varepsilon^2\overline{v}_2+\cdots)\\
&=-\frac{1}{\varepsilon^3}\frac{\partial}{\partial\overline{y}}(\varepsilon\overline{p}_1+\varepsilon^2\overline{p}_2+\cdots)-\varepsilon^2(\alpha_1+\varepsilon\alpha_2+\cdots)^2(\varepsilon\overline{v}_1+\varepsilon^2\overline{v}_2+\cdots)\\
&+2\varepsilon^5-\mathrm{i}(\alpha_1+\varepsilon\alpha_2+\cdots)\frac{\partial}{\partial x}(\varepsilon\overline{v}_1+\varepsilon^2\overline{v}_2+\cdots)\\
&+\varepsilon^8\frac{\partial^2}{\partial x^2}(\varepsilon\overline{v}_1+\varepsilon^2\overline{v}_2+\cdots)+\varepsilon^2\frac{\partial^2}{\partial\overline{y}^2}(\varepsilon\overline{v}_1+\varepsilon^2\overline{v}_2+\cdots).
\end{aligned}
$$

Expanding the above yields

$$
\begin{aligned}
&\frac{1}{\varepsilon^3}(-\varepsilon\mathrm{i}\omega_1\overline{v}_1-\varepsilon^2\mathrm{i}\omega_1\overline{v}_2-\varepsilon^2\mathrm{i}\omega_2\overline{v}_1-\varepsilon^3\mathrm{i}\omega_2\overline{v}_2)+\frac{\partial}{\partial t}(\varepsilon\overline{v}_1+\varepsilon^2\overline{v}_2+...)\\
&=-\frac{1}{\varepsilon^3}\frac{\partial}{\partial\overline{y}}(\varepsilon\overline{p}_1+\varepsilon^2\overline{p}_2+...)+\varepsilon^2\frac{\partial^2}{\partial\chi^2}(\varepsilon\overline{v}_1+\varepsilon^2\overline{v}_2+\cdots)\\
&+2\varepsilon^5\mathrm{i}(\alpha_1+\varepsilon\alpha_2+\cdots)\frac{\partial}{\partial x}(\varepsilon\overline{v}_1+\varepsilon^2\overline{v}_2+\cdots)\\
&+\varepsilon^8\frac{\partial^2}{\partial x^2}(\varepsilon\overline{v}_1+\varepsilon^2\overline{v}_2+\cdots)+\varepsilon^2\frac{\partial^2}{\partial\overline{y}^2}(\varepsilon\overline{v}_1+\varepsilon^2\overline{v}_2+\cdots).
\end{aligned}
$$

Collecting terms of $\mathcal{O}(\varepsilon^{-2})$ we arrive at

$$-\mathrm{i}\omega_1\overline{v}_1=-\frac{\partial\overline{p}_1}{\partial\overline{y}}.$$

Therefore the equations for the upper deck are given by

$$i\alpha_1\overline{u}_1+\frac{\partial\overline{v}_1}{\partial\overline{y}}=0, \tag{5.1.6a}$$

$$-\mathrm{i}\omega_1\overline{u}_1=-\mathrm{i}\alpha_1\overline{p}_1, \tag{5.1.6b}$$

$$-\mathrm{i}\omega_1\overline{v}_1=-\frac{\partial\overline{p}_1}{\partial\overline{y}}. \tag{5.1.6c}$$

We will now eliminate $\overline{u}_1$ and $\overline{v}_1$. Differentiating (5.1.6c) with respect to $\overline{y}$ yields

$$-\mathrm{i}\omega_1 \frac{\partial \overline{v}_1}{\partial \overline{y}} = -\frac{\partial^2 \overline{p}_1}{\partial \overline{y}^2}.$$

Now

$$-\mathrm{i}\omega_1(-\mathrm{i}\alpha_1 \overline{u}_1) = -\frac{\partial^2 \overline{p}_1}{\partial \overline{y}^2}.$$

Therefore

$$\frac{\partial^2 \overline{p}_1}{\partial \overline{y}^2} - \alpha_1^2 \overline{p}_1 = 0.$$

The solution satisfying boundedness as $\overline{y} \to \infty$ and matching with the solution in the main deck is

$$\overline{p}_1 = p_1(x)e^{-\alpha_1 \overline{y}},$$

where $p_1(x)$ is an arbitrary integration function. From (5.1.6b) we have that

$$\overline{u}_1 = \frac{\alpha_1}{\omega_1}\overline{p}_1 = \frac{1}{\overline{f'}(0)} p_1(x)e^{-\alpha_1 \overline{y}}.$$

From (5.1.6c) we have that

$$\overline{v}_1 = \frac{i}{\overline{f'}(0)} p_1(x)e^{-\alpha_1 \overline{y}}.$$

Matching $\overline{v}_1$ as $\overline{y} \to 0$ with v_1 as $\hat{Y} \to \infty$ yields

$$B_0 = -\frac{p_1(x)}{\alpha_1(\overline{f'}(0))^2}.$$

The desired dispersion relation is then obtained by matching the solutions in the main deck with those in the lower deck. In the lower deck $y = \varepsilon^5 Z$, with $Z = \mathcal{O}(1)$. Close to the wall $u_B \approx \overline{f'_\eta}(0) - \lambda \varepsilon Z + \cdots$, and $v_B \approx -\varepsilon^2 \lambda'_X Z^2/2 + \cdots$. To match with the main deck solutions, the disturbance quantities expand as

$$\tilde{u} = (U_1 + \varepsilon U_2 + \cdots)E, \tag{5.1.7a}$$

$$\tilde{v} = (\varepsilon^2 V_1 + \varepsilon^3 V_2 + \cdots)E, \tag{5.1.7b}$$

$$\tilde{p} = (\varepsilon P_1 + \varepsilon^2 P_2 + \cdots)E, \tag{5.1.7c}$$

where all of the above functions depend on both Z and x. Taking the relevant scalings we obtain the following for the continuity equation

$$\frac{1}{\varepsilon^3}\frac{\partial \tilde{u}}{\partial X} + \frac{\partial \tilde{u}}{\partial x} + \frac{1}{\varepsilon^5}\frac{\partial \tilde{v}}{\partial Z} = 0.$$

Substituting (5.1.7) into (5.0.3a) yields

$$\frac{1}{\varepsilon^3} i(\alpha_1 + \varepsilon\alpha_2 + \cdots)(U_1 + \varepsilon U_2 + \cdots) + \frac{\partial}{\partial x}(U_1 + \varepsilon U_2 + \ldots) + \frac{1}{\varepsilon^5}\frac{\partial}{\partial Z}(\varepsilon^2 V_1 + \varepsilon^3 V_2 + \cdots) = 0.$$

Expanding the above yields

$$\begin{aligned}&\frac{1}{\varepsilon^3} i(\alpha_1 U_1 + \varepsilon\alpha_1 U_2 + \varepsilon\alpha_2 U_1 + \varepsilon^2\alpha_2 U_2 + \cdots) + \frac{\partial}{\partial x}(U_1 + \varepsilon U_2 + \cdots)\\ &+ \frac{1}{\varepsilon^5}\frac{\partial}{\partial Z}(\varepsilon^2 V_1 + \varepsilon^3 V_2 + \cdots) = 0.\end{aligned}$$

Collecting $\mathcal{O}(\varepsilon^{-3})$ terms we arrive at

$$i\alpha_1 U_1 + \frac{\partial V_1}{\partial Z} = 0.$$

The relevant PDE for the x momentum equation in terms of the asymptotic scales is given as follows

$$\begin{aligned}
&\frac{1}{\varepsilon^3}\frac{\partial \tilde{u}}{\partial \tau}+\frac{\partial \tilde{u}}{\partial t}+(\overline{f'}(0)-\lambda\varepsilon Z)\left(\frac{1}{\varepsilon^3}\frac{\partial \tilde{u}}{\partial \chi}+\frac{\partial \tilde{u}}{\partial x}\right)+\tilde{u}\frac{\partial}{\partial x}(\overline{f'}(0)-\lambda\varepsilon Z)\\
&+\frac{\tilde{v}}{\varepsilon^5}\frac{\partial}{\partial Z}(\overline{f'}(0)-\lambda\varepsilon Z)-\frac{\varepsilon\lambda_X' Z^2}{2}\frac{\partial \tilde{u}}{\partial Z}=-\frac{1}{\varepsilon^3}\frac{\partial \tilde{p}}{\partial \chi}-\frac{\partial \tilde{p}}{\partial x}\\
&+\varepsilon^8\left(\frac{1}{\varepsilon^6}\frac{\partial^2 \tilde{u}}{\partial \chi^2}+\frac{2}{\varepsilon^3}\frac{\partial^2 \tilde{u}}{\partial x\partial \chi}+\frac{\partial^2 \tilde{u}}{\partial x^2}+\frac{1}{\varepsilon^{10}}\frac{\partial^2 \tilde{u}}{\partial Z^2}\right).
\end{aligned}$$

Substituting (5.1.7) into (5.0.3b) yields

$$\begin{aligned}
&\frac{1}{\varepsilon^3}(-i\omega_1-\varepsilon i\omega_2-\cdots)(U_1+\varepsilon U_2+\cdots)+\frac{\partial}{\partial t}(U_1+\varepsilon U_2+\cdots)\\
&+\frac{\overline{f'}(0)}{\varepsilon^3}i(\alpha_1+\varepsilon\alpha_2+\cdots)(U_1+\varepsilon U_2+\cdots)+\overline{f'}(0)\frac{\partial}{\partial x}(U_1+\varepsilon U_2+\cdots)\\
&-\frac{\lambda Z}{\varepsilon^2}i(\alpha_1+\varepsilon\alpha_2+\cdots)(U_1+\varepsilon U_2+\cdots)-\lambda\varepsilon Z\frac{\partial}{\partial x}(U_1+\varepsilon U_2+\cdots)\\
&-\frac{\lambda}{\varepsilon^4}(\varepsilon^2 V_1+\varepsilon^3 V_2+\cdots)-\frac{\varepsilon\lambda_X' Z^2}{2}\frac{\partial}{\partial Z}(U_1+\varepsilon U_2+\cdots)\\
&=-\frac{1}{\varepsilon^3}i(\alpha_1+\varepsilon\alpha_2+\cdots)(\varepsilon P_1+\varepsilon^2 P_2+\cdots)\\
&-\frac{\partial}{\partial x}(\varepsilon P_1+\varepsilon^2 P_2+\cdots)-\varepsilon^2(\alpha_1+\varepsilon\alpha_2+\cdots)^2(U_1+\varepsilon U_2+\cdots)\\
&+2\varepsilon^5 i(\alpha_1+\varepsilon\alpha_2+\cdots)\frac{\partial}{\partial x}(U_1+\varepsilon U_2+\cdots)\\
&+\varepsilon^8\frac{\partial^2}{\partial x^2}(U_1+\varepsilon U_2+\cdots)+\frac{1}{\varepsilon^2}\frac{\partial^2}{\partial Z^2}(U_1+\varepsilon U_2+\cdots).
\end{aligned}$$

We have that

$$\begin{aligned}
&\frac{1}{\varepsilon^3}(-i\omega_1 U_1-\varepsilon i\omega_1 U_2-\varepsilon i\omega_2 U_1-\varepsilon^2 i\omega_2 U_2-\cdots)+\frac{\partial}{\partial t}(U_1+\varepsilon U_2+\cdots)\\
&+\frac{\overline{f'}(0)}{\varepsilon^3}i(\alpha_1 U_1+\varepsilon\alpha_1 U_2+\varepsilon\alpha_2 U_1+\varepsilon^2\alpha_2 U_2+\cdots)+\overline{f'}(0)\frac{\partial}{\partial x}(U_1+\varepsilon U_2+\cdots)\\
&-\frac{\lambda Z}{\varepsilon^2}i(\alpha_1 U_1+\varepsilon\alpha_1 U_2+\varepsilon\alpha_2 U_1+\varepsilon^2\alpha_2 U_2+\cdots)-\lambda\varepsilon Z\frac{\partial}{\partial x}(U_1+\varepsilon U_2+\cdots)\\
&-\frac{\lambda}{\varepsilon^4}(\varepsilon^2 V_1+\varepsilon^3 V_2+\cdots)-\frac{\varepsilon\lambda_X' Z^2}{2}\frac{\partial}{\partial Z}(U_1+\varepsilon U_2+\cdots)
\end{aligned}$$

$$
\begin{aligned}
&= -\frac{1}{\varepsilon^3} i(\varepsilon\alpha_1 P_1 + \varepsilon^2\alpha_1 P_2 + \varepsilon^2\alpha_2 P_1 + \varepsilon^3\alpha_2 P_2 + \cdots) \\
&- \frac{\partial}{\partial x}(\varepsilon P_1 + \varepsilon^2 P_2 + \cdots) - \varepsilon^2(\alpha_1 + \varepsilon\alpha_2 + \cdots)^2(U_1 + \varepsilon U_2 + \cdots) \\
&+ 2\varepsilon^5 i(\alpha_1 + \varepsilon\alpha_2 + \cdots)\frac{\partial}{\partial x}(U_1 + \varepsilon U_2 + \cdots) \\
&+ \varepsilon^8 \frac{\partial^2}{\partial x^2}(U_1 + \varepsilon U_2 + \cdots) + \frac{1}{\varepsilon^2}\frac{\partial^2}{\partial Z^2}(U_1 + \varepsilon U_2 + \cdots).
\end{aligned}
$$

Given that $\alpha_1 \overline{f'}(0) = \omega_1$ and collecting terms of $\mathcal{O}(\varepsilon^{-2})$ yields

$$
-i(\omega_2 - \overline{f'}(0)\alpha_2)U_1 - i\alpha_1\lambda Z U_1 - \lambda V_1 = -i\alpha_1 P_1 + \frac{\partial^2 U_1}{\partial Z^2}.
$$

The relevant PDE for the y momentum equation in terms of the asymptotic scales is given by

$$
\begin{aligned}
&\frac{1}{\varepsilon^3}\frac{\partial \tilde{v}}{\partial \tau} + \frac{\partial \tilde{v}}{\partial t} + (\overline{f'}(0) - \lambda\varepsilon Z)\left(\frac{1}{\varepsilon^3}\frac{\partial \tilde{v}}{\partial \chi} + \frac{\partial \tilde{v}}{\partial x}\right) \\
&- \frac{1}{2}\varepsilon^6 \lambda''_{XX} Z^2 \tilde{u} - \varepsilon Z \lambda'_X \tilde{v} - \frac{1}{2}\lambda'_X Z^2 \frac{\partial \tilde{v}}{\partial Z} = -\frac{1}{\varepsilon^5}\frac{\partial \tilde{p}}{\partial Z} \\
&+ \varepsilon^8\left(\frac{1}{\varepsilon^6}\frac{\partial^2 \tilde{v}}{\partial \chi^2} + \frac{2}{\varepsilon^3}\frac{\partial^2 \tilde{v}}{\partial x \partial \chi} + \frac{\partial^2 \tilde{v}}{\partial x^2} + \frac{1}{\varepsilon^{10}}\frac{\partial^2 \tilde{v}}{\partial Z^2}\right).
\end{aligned}
$$

Substitution of (5.1.7) into (5.0.3c) yields

$$
\begin{aligned}
&\frac{1}{\varepsilon^3}(-i\omega_1 - \varepsilon i\omega_2 - \cdots)(\varepsilon^2 V_1 + \varepsilon^3 V_2 + \cdots) + \frac{\partial}{\partial t}(\varepsilon^2 V_1 + \varepsilon^3 V_2 + \cdots) \\
&+ \frac{\overline{f'}(0)}{\varepsilon^3} i(\alpha_1 + \varepsilon\alpha_2 + \cdots)(\varepsilon^2 V_1 + \varepsilon^3 V_2 + \cdots) + \overline{f'}(0)\frac{\partial}{\partial x}(\varepsilon^2 V_1 + \varepsilon^3 V_2 + \cdots) \\
&- \frac{\lambda Z}{\varepsilon^2} i(\alpha_1 + \varepsilon\alpha_2 + \cdots)(\varepsilon^2 V_1 + \varepsilon^3 V_2 + \cdots) - \lambda\varepsilon Z\frac{\partial}{\partial x}(\varepsilon^2 V_1 + \varepsilon^3 V_2 + \cdots) \\
&- \frac{1}{2}\varepsilon^6\lambda''_{XX} Z^2(U_1 + \varepsilon U_2 + \cdots) - \varepsilon Z\lambda'_X(\varepsilon^2 V_1 + \varepsilon^3 V_2) - \frac{1}{2}\varepsilon\lambda'_X Z^2\frac{\partial}{\partial Z}(\varepsilon^2 V_1 + \varepsilon^3 V_2 + \cdots) \\
&= -\frac{1}{\varepsilon^5}\frac{\partial}{\partial Z}(\varepsilon P_1 + \varepsilon^2 P_2 + \cdots) - \varepsilon^2(\alpha_1 + \varepsilon\alpha_2 + \cdots)^2(\varepsilon^2 V_1 + \varepsilon^3 V_2 + \cdots) \\
&+ 2\varepsilon^5 i(\alpha_1 + \varepsilon\alpha_2 + \cdots)\frac{\partial}{\partial x}(\varepsilon^2 V_1 + \varepsilon^3 V_2 + \cdots) \\
&+ \varepsilon^8\frac{\partial^2}{\partial x^2}(\varepsilon^2 V_1 + \varepsilon^3 V_2 + \cdots) + \frac{1}{\varepsilon^2}\frac{\partial^2}{\partial Z^2}(\varepsilon^2 V_1 + \varepsilon^3 V_2 + \cdots).
\end{aligned}
$$

The pressure term dominates all other terms in the above expression therefore we obtain

$$\frac{\partial P_1}{\partial Z} = 0.$$

The governing equations at leading order are therefore given by

$$i\alpha_1 U_1 + \frac{\partial V_1}{\partial Z} = 0, \tag{5.1.8a}$$

$$-i(\omega_2 - \overline{f'}(0)\alpha_2)U_1 - i\alpha_1\lambda Z U_1 - \lambda V_1 = -i\alpha_1 P_1 + \frac{\partial^2 U_1}{\partial Z^2}, \tag{5.1.8b}$$

$$\frac{\partial P_1}{\partial Z} = 0. \tag{5.1.8c}$$

From equation (5.1.8c) we have that $P_1 = P_1(x)$ and this matches with the pressure in the main deck so

$$P_1 = p_1.$$

Differentiating (5.1.8b) with respect Z yields

$$-i(\omega_2 - \overline{f'}(0)\alpha_2)\frac{\partial U_1}{\partial Z} - i\alpha_1\lambda U_1 - i\alpha_1\lambda Z\frac{\partial U_1}{\partial Z} - \lambda\frac{\partial V_1}{\partial Z} = \frac{\partial^3 U_1}{\partial Z^3}.$$

Making use of the continuity equation (5.1.8a) yields

$$\frac{\partial^3 U_1}{\partial Z^3} - [i(\alpha_2\overline{f'}(0) - \omega_2) - i\alpha_1\lambda Z]\frac{\partial U_1}{\partial Z} = 0. \tag{5.1.9}$$

By setting

$$\zeta = (-i\alpha_1\lambda)^{\frac{1}{3}}\left(Z - \frac{\alpha_2\overline{f'}(0) - \omega_2}{\alpha_1\lambda}\right),$$

we can simplify (5.1.9) and by doing so we obtain the following

$$\frac{\partial^3 U_1}{\partial \zeta^3} - \zeta\frac{\partial U_1}{\partial \zeta} = 0.$$

We note that the solution for U_1 must satisfy $U_1 = 0$ at $Z = 0$. As $\hat{Y} \to \infty$ in the lower deck we have that $u_1 \to \lambda B_0$. Matching $\overline{v}_1$ as $\overline{y} \to 0$ with v_1 as $\hat{Y} \to \infty$ we showed that

$$B_0 = -\frac{p_1(x)}{\alpha_1(\overline{f'}(0))^2}. \tag{5.1.10}$$

Therefore

$$U_1 \to -\frac{p_1\lambda}{\alpha_1(\overline{f'}(0))^2}$$

as $Z \to \infty$. The solution which is bounded as $\zeta \to \infty$ is

$$\frac{\partial U_1}{\partial \zeta} = C\mathrm{Ai}(\zeta),$$

where Ai is the appropriately decaying Airy function. Integrating the previous expression we have that

$$U_1 = C\int_{\zeta_0}^{\zeta} \mathrm{Ai}(\hat{\zeta})d\hat{\zeta}.$$

To satisfy the boundary condition $U_1 = 0$ at $\zeta = \zeta_0$ we have that

$$\zeta_0 = (-i\alpha_1\lambda)^{-\frac{2}{3}} i(\alpha_2\overline{f'}(0) - \omega_2).$$

Applying the boundary conditions $U_1(Z = 0) = V_1(Z = 0) = 0$ to (5.1.8b) yields

$$\frac{\partial^2 U_1}{\partial Z^2} = i\alpha_1 P_1,$$

at $Z = 0$. Therefore we obtain

$$(-i\alpha_1\lambda)^{\frac{2}{3}} \frac{\partial^2 U_1}{\partial \zeta^2} = i\alpha_1 p_1,$$

Thus we determine the following relation between C and p_1

$$(-i\alpha_1\lambda)^{\frac{2}{3}}C\mathrm{Ai}'(\xi_0) = i\alpha_1 p_1. \tag{5.1.11}$$

5.2 The Governing Eigenrelation

Matching between the main and lower decks gives us a second relationship between C and p_1, this being

$$C\int_{\zeta_0}^{\infty}\mathrm{Ai}(\zeta)\,\mathrm{d}\zeta = -\frac{\lambda p_1}{\alpha_1(\overline{f'_\eta}(0))^2}. \tag{5.2.1}$$

Combining (5.1.11) and (5.2.1) gives

$$\frac{(-\mathrm{i}\alpha_1\lambda)^{2/3}\,\mathrm{Ai}'(\zeta_0)}{\kappa} = -\frac{\mathrm{i}\alpha_1^2(\overline{f'_\eta}(0))^2}{\lambda}, \tag{5.2.2}$$

where

$$\kappa = \int_{\zeta_0}^{\infty}\mathrm{Ai}(\zeta)\,\mathrm{d}\zeta.$$

To solve (5.2.2) we start by rewriting ζ as follows

$$\zeta = (\alpha_1\lambda Z - (\alpha_2\overline{f'_\eta}(0) - \omega_2))\frac{(-i\alpha_1\lambda)^{\frac{1}{3}}}{\alpha_1\lambda} = \left(\lambda Z - \frac{(\alpha_2\overline{f'_\eta}(0) - \omega_2)}{\alpha_1}\right)\frac{(-i\alpha_1\lambda)^{\frac{1}{3}}}{\lambda}.$$

By letting $\beta = \alpha_2\overline{f'_\eta}(0) - \omega_2$ we have that

$$\zeta = \frac{(\lambda Z - \alpha_1^{-1}\beta)}{q},$$

where

$$q = \left(\frac{\lambda^3}{-i\alpha_1\lambda}\right)^{\frac{1}{3}} = \left(\frac{\lambda^2}{-i\alpha_1}\right)^{\frac{1}{3}},$$

and $\zeta_0 = -\frac{\beta}{\alpha_1 q}$. On rearranging (5.2.2) we obtain the following expression for α_1

$$\alpha_1 = -\frac{\lambda}{i\alpha_1(\overline{f'_\eta}(0)^2}(-i\alpha_1\lambda)^{\frac{2}{3}}\frac{\mathrm{Ai}'(\zeta_0)}{\kappa} = \alpha_1^{-\frac{1}{3}}\lambda^{\frac{2}{3}}(-i)^{-\frac{1}{3}}\lambda(\overline{f'_\eta}(0))^{-2}\frac{\mathrm{Ai}'(\zeta_0)}{\kappa}.$$

Therefore

$$\alpha_1 = q\lambda(\overline{f'_\eta}(0))^{-2}\frac{\mathrm{Ai}'(\zeta_0)}{\kappa}.$$

Restricting our attention to neutrally stable solutions (α_1 real) and following a similar analysis to that outlined in Miller *et al.* (2018) one finds that $\mathrm{Ai}'(\zeta_0)/\kappa = c_2(-i)^{\frac{1}{3}}$ where $c_2 \approx 1.0003$. We also have that $\zeta_0 = -c_1(-i)^{\frac{1}{3}}$ where $c_1 \approx 2.2970$. To see this we note that $\mathrm{Ai}'(\zeta_0)/\kappa$ is related to the Tietjens function (see, for example, Healey (1995)). Using the notation in Healey (1995), this function is given by

$$F^+(\xi_0) = 1 - \frac{\mathrm{Ai}'(\xi_0)}{\xi_0\int_\infty^{\xi_0}\mathrm{Ai}(\xi)\mathrm{d}\xi}.$$

A standard property of the Tietjens function is that it is real for $z = z_0 \approx 2.2970$, with

$$F^+(e^{-\frac{5\pi i}{6}}z_0) \approx 0.564.$$

For the Blasius boundary layer $z = z_0$ corresponds to the lower branch of the neutral curve, while $F^+(\xi_0) \to 0$, as $|\xi_0| \to \infty$, where this limit corresponds to the upper branch, see Healey (1995). For the present problem $F^+(\zeta_0)$ is the complex conjugate of $F^+(\xi_0)$, see Figure 5.1.

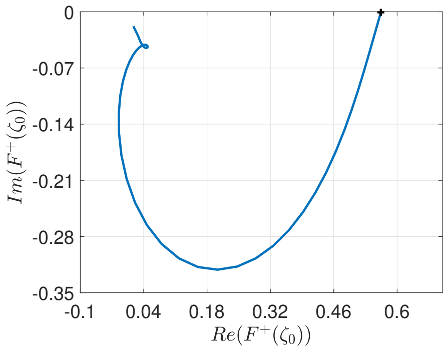

Figure 5.1: The locus of the Tietjens function for ζ_0, were z is real and varies between 2.2 and 12. The black marker represents the point $F^+(e^{\frac{5\pi i}{6}}z_0) \approx 0.564$ were $z = z_0 \approx 2.2970$.

Now

$$\alpha_1 = q\lambda(\overline{f'_\eta}(0))^{-2}c_2(-i)^{\frac{1}{3}},$$

and given the definition of q we have that

$$\alpha_1 = \lambda^{\frac{5}{4}}(\overline{f'_\eta}(0))^{-\frac{3}{2}}c_2^{\frac{3}{4}}.$$

Therefore we obtain the following expression for β

$$\beta = -\zeta_0\alpha_1 q = -(-c_1(-i)^{\frac{1}{3}})\alpha_1\left(\frac{\lambda^2}{-i\alpha_1}\right)^{\frac{1}{3}}.$$

Now

$$\beta = c_1(\overline{f'_\eta}(0))^{-1}c_2^{\frac{1}{2}}\lambda^{\frac{3}{2}}. \tag{5.2.3}$$

Given that $\alpha\overline{f'_\eta}(0) = \omega$, we notice that

$$\overline{f'_\eta}(0) - c = \overline{f'_\eta}(0) - \frac{\omega_1 + \varepsilon\omega_2 + \dots}{\alpha_1(1 + \varepsilon\frac{\alpha_2}{\alpha_1} + \cdots)}.$$

Now

$$\overline{f'_\eta}(0) - c = \overline{f'_\eta}(0) - \frac{\omega_1}{\alpha_1} + \varepsilon\frac{(\alpha_2\overline{f'_\eta}(0) - \omega_2)}{\alpha_1} + \cdots$$

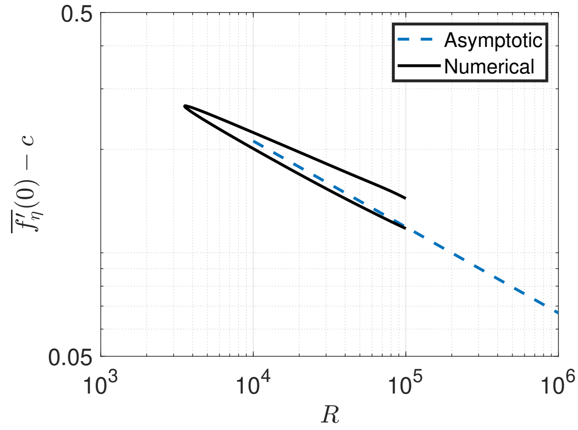

Figure 5.2: A comparison between the asymptotic and numerical results in the case when $a=0$. The large Reynolds number asymptotic solution is given by the dashed curve.

using $\alpha_1\overline{f'_\eta}(0)=\omega_1$ we have that

$$\overline{f'_\eta}(0)-c=\varepsilon\frac{\beta}{\alpha_1}+\cdots$$

Recall that $\varepsilon=Re^{-\frac{1}{8}}$ and the relationship between Re and R is given by $R=\overline{\delta}\sqrt{Rex}$, this gives $\varepsilon=R^{-\frac{1}{4}}\overline{\delta}^{\frac{1}{4}}x^{\frac{1}{8}}$. Substituting into the above yields

$$\overline{f'_\eta}(0)-c=\frac{(\overline{f'_\eta}(0))^{-1}\overline{\delta}^{\frac{1}{4}}c_1c_2^{\frac{1}{2}}\lambda^{\frac{3}{2}}R^{-\frac{1}{4}}}{\lambda^{\frac{5}{4}}c_2^{\frac{3}{2}}(\overline{f'_\eta}(0))^{-\frac{3}{2}}},$$

where λ is of the form $\overline{f''_{\eta\eta}}(0)x^{-\frac{1}{2}}$. Therefore we obtain

$$\overline{f'(0)}-c\approx 2.297\left[\frac{\overline{\delta}|\overline{f''_{\eta\eta}}(0)|(\overline{f'_\eta}(0))^2}{R}\right]^{1/4}. \tag{5.2.4}$$

This expression gives a leading order approximation to the lower branch of the neutral stability curve in the limit of large R. We are, therefore, able to make a comparison between the solutions we determined numerically in §4.4 and this analytical expression.

In Figure 5.2 we present this comparison in the case of a smooth translating boundary, i.e.,

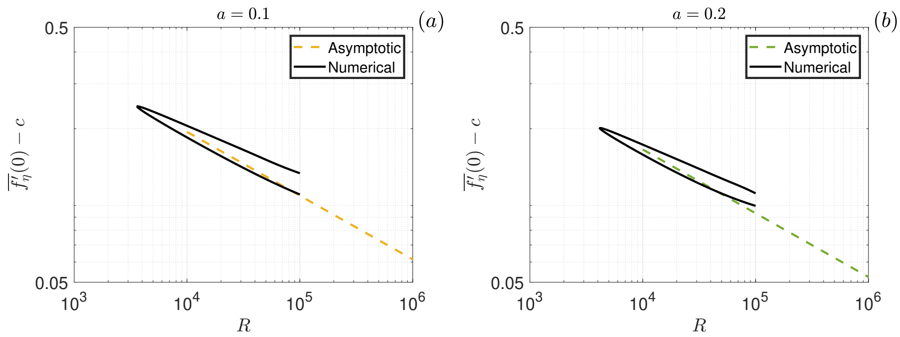

Figure 5.3: In (a) a comparison between the asymptotic and numerical results in the case when $a = 0.1$. In (b) a comparison between the asymptotic and numerical results in the case when $a = 0.2$. The large Reynolds number asymptotic solution is given by the dashed curve.

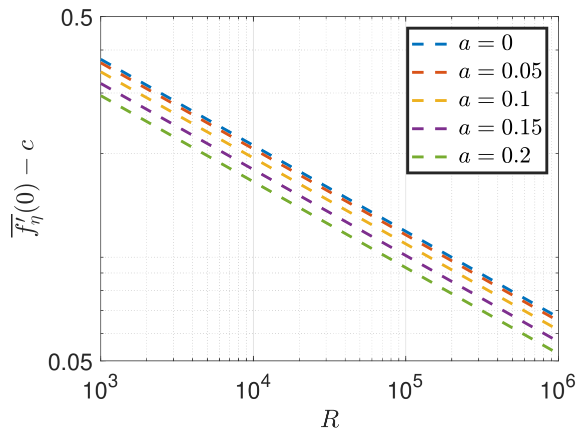

Figure 5.4: Asymptotic approximations for the quantity $\overline{f'_\eta}(0) - c$ on a log-log scale for various values of the roughness paramter.

when the constant a is equal to zero. In this case the expression (5.2.4) reduces in complexity given that $f'_\eta(0) = 1$. We observe an excellent agreement between the two sets of solutions, with the lower branch of the neutral stability curve tending towards our asymptotic result in the limit as $R \to \infty$. Indeed, we find that this agreement is equally as good for the values $a = 0.1$ and $a = 0.2$, see Figure 5.3.

In Figure 5.4 we present the lower branch asymptotic results for various values of the roughness parameter. We outlined in 4.1 that as the value of a increases there is a downward shift of both the upper and lower branches of the neutral stability curves, with the overall result being a reduction in the area encompassed by the curves. This shifting of the lower branch is supported by the asymptotic results we present here and is clearly evidenced in Figure 5.4. In conclusion, we have demonstrated excellent agreement between the asymptotic predictions and the numerical solutions presented in Section §4.4. It is worth noting that this agreement has been achieved using only the leading term in the asymptotic expansion. Given the strong alignment observed between the numerical and asymptotic solutions, we argue that incorporating additional terms in the expansion is unnecessary. However, including more terms would likely further enhance the agreement between the two approaches.

Chapter 6

Linear Stability - Effect of Small Amplitude Waviness

In this chapter, we build upon the ideas presented by Lessen & Gangwani (1976), who investigated how small-amplitude wall roughness influences the minimum critical Reynolds number of a laminar boundary layer. Their analysis employed assumptions typical of parallel flow stability problems. Specifically, Lessen & Gangwani (1976) examined the two-dimensional flow of an inviscid incompressible fluid over a flat plate with a single Fourier component of roughness. To explore this effect, they solved the steady Orr-Sommerfeld equation under inhomogeneous boundary conditions, capturing the response of the boundary layer to the surface waviness. The solution provided key information for evaluating the Reynolds stress, which alters the mean flow. Subsequently, they derived the modified mean flow by solving the Reynolds-averaged boundary layer equations. Through linear stability analysis of this adjusted mean flow, the authors found that the minimum critical Reynolds number decreased by 10% for a surface roughness amplitude of just 1% of the boundary layer thickness.

In §6.1, we derive the Reynolds-averaged boundary layer equations, followed by the formulation of the inhomogeneous boundary conditions in §6.2. In §6.4, we aim to replicate the findings of Lessen & Gangwani (1976) by investigating how increasing the amplitude influences the mean flow, employing the methods detailed in §6.3. Subsequently, we examine the linear stability characteristics of the flow in §6.5 using the techniques described in Chapter 4. Finally, in §6.6 and §6.7, we extend the methods of Lessen & Gangwani (1976) to explore the effects of a wavy wall on the boundary layer generated by a surface moving at a constant velocity, followed by an analysis of the linear stability of this flow.

6.1 The Reynolds-Averaged Boundary Layer Equations

Our analysis here differs from our previous work as we now separate the flow into a mean component and a perturbation component. This allows the analysis of small disturbances caused by wall waviness while assuming that these disturbances do not significantly alter the mean flow. The mean flow represents the primary, undisturbed laminar boundary layer flow, while the fluctuating component captures the boundary layer's response to small-amplitude waviness. By applying this linear superposition, we arrive at the Reynolds-averaged boundary layer equations—essentially the standard boundary layer equations with the inclusion of the Reynolds stress. Solving the steady Orr-Sommerfeld equation with inhomogeneous boundary conditions yields the fluctuating components, allowing us to compute the Reynolds stress and quantify how the perturbations impact the mean flow. Once the modified mean flow is obtained, the techniques introduced in Chapter 4 can be used to analyse the onset of linear instability.

To solve for the mean distorted profile that results in the presence of the wavy wall we begin by deriving the modified boundary layer equations. We start by considering the standard boundary layer equations which are given by

$$\frac{\partial u^*}{\partial x^*} + \frac{\partial v^*}{\partial y^*} = 0, \tag{6.1.1a}$$

$$u^* \frac{\partial u^*}{\partial x^*} + v^* \frac{\partial u^*}{\partial y^*} = \nu^* \frac{\partial^2 u^*}{\partial y^{*2}}. \tag{6.1.1b}$$

Here the surface of the plate is described by

$$y^* = h^*(x^*) = \varsigma^* e^{\mathrm{i}\tilde{\alpha}^* x^*} + \text{c.c}, \tag{6.1.2}$$

where $(\varsigma^* \tilde{\alpha}^* / 2\pi) \ll 1$ and c.c denotes complex conjugate. The term $\varsigma^* e^{\mathrm{i}\tilde{\alpha}^* x^*}$ represents a small sinusoidal disturbance where ς^* is the dimensional amplitude and $\tilde{\alpha}^*$ is the wavenumber that determines the periodicity of the wall waviness and is real , and it governs how frequently the surface undulates along the streamwise direction. The condition $(\varsigma^* \tilde{\alpha}^* / 2\pi) \ll 1$, implies that $\frac{\mathrm{d}h^*}{\mathrm{d}x^*} \ll 1$, ensuring that the amplitude is small compared to the wavelength. The complex conjugate ensures the disturbance is real valued. The difference between A^* used previously and ς^* lies in the way each is non-dimensionalised. The dimesnional amplitude A^*, introduced in Section §2.1, is related to the roughness parameter a, which is defined as

$$a = \frac{A^*}{\gamma^*},$$

where γ^* is the wavelength of the surface waviness. In this case, the non-dimensionalising length-scale L^* is set equal to the wavelength. The dimensional amplitude ς^*, introduced here, is expressed in terms of the displacement thickness δ^*. This approach is necessary because obtaining the modified mean flow requires evaluating the Reynolds stress, which is computed by solving the steady Orr-Sommerfeld equation. In the derivation of the Orr-Sommerfeld equation, all length scales are expressed in terms of the displacement thickness. Therefore, to maintain consistency, ς^* must also be expressed relative to δ^*. System (6.1.1) is solved subject to the following conditions

$$u^*(y^* = h^*(x^*)) = v^*(y = h^*(x^*)) = 0, \quad u^*(y^* \to \infty) \to U_\infty^*, \tag{6.1.3}$$

where U_∞^* is the dimensional free stream velocity. We now make the equations dimensionless by introducing the following scalings

$$(x,y,\varsigma) = \frac{(x^*,y^*,\varsigma^*)}{\delta^*}, \quad (u,v) = \frac{(u^*,v^*)}{U_\infty^*}, \quad \tilde{\alpha} = \tilde{\alpha}^*\delta^*.$$

Applying the above scalings yields the following

$$\frac{\partial u}{\partial x} + \frac{\partial v}{\partial y} = 0, \tag{6.1.4a}$$

$$u\frac{\partial u}{\partial x} + v\frac{\partial u}{\partial y} = \frac{1}{R}\frac{\partial^2 u}{\partial y^2}, \tag{6.1.4b}$$

where $R = U_\infty^*\delta^*/\nu^*$. System (6.1.4) is now solved subject to the conditions

$$u(y = h(x)) = v(y = h(x)) = 0, \quad u(y \to \infty) \to 1. \tag{6.1.5}$$

We now decompose the flow components (u,v) into a mean part (U_m,V_m), representing the undisturbed laminar boundary layer flow, and a fluctuating part $(\tilde{u},\tilde{v})$,which captures the boundary layer's response to the small-amplitude wall waviness. This gives the following expressions for the velocity components:

$$u = U_m + \tilde{u}, \quad v = V_m + \tilde{v}. \tag{6.1.6}$$

Given that the surface variation described by (6.1.2) is a steady, spatially periodic function — meaning the surface waviness does not change with time — the resulting fluctuations in the flow are also time-invariant. These fluctuations can be defined as:

$$\tilde{u} = \hat{u}(y)e^{\mathrm{i}\tilde{\alpha}x} + \text{c.c}, \tag{6.1.7a}$$

$$\tilde{v} = \hat{v}(y)e^{\mathrm{i}\tilde{\alpha}x} + \text{c.c.} \tag{6.1.7b}$$

To simplify the subsequent analysis, we apply a spatial averaging procedure over one wavelength of the wavy surface. This averaging is defined by the following integral,

$$\overline{H} = \frac{\tilde{\alpha}}{2\pi} \int_{x}^{x+\frac{2\pi}{\tilde{\alpha}}} H \,\mathrm{d}x.$$

Notably, taking the spatial average of the mean part leaves the mean flow U_m unchanged, i.e., $\overline{U_m} = U_m$. Additionally, due to the periodic nature of the fluctuations, the spatial averages of the fluctuating components are zero: $\overline{\tilde{u}} = 0$ and $\overline{\tilde{v}} = 0$. Substitution of (6.1.6) into the continuity equation yields

$$\frac{\partial U_m}{\partial x} + \frac{\partial \tilde{u}}{\partial x} + \frac{\partial V_m}{\partial y} + \frac{\partial \tilde{v}}{\partial y} = 0. \tag{6.1.8}$$

Averaging over one wall wavelength yields the following

$$\overline{\frac{\partial U_m}{\partial x}} + \overline{\frac{\partial \tilde{u}}{\partial x}} + \overline{\frac{\partial V_m}{\partial u}} + \overline{\frac{\partial \tilde{v}}{\partial y}} = 0.$$

Since the average of the mean flow remains unchanged and the average of the fluctuations vanish, we obtain the following

$$\frac{\partial U_m}{\partial x} + \frac{\partial V_m}{\partial y} = 0. \tag{6.1.9}$$

Substitution of (6.1.9) into (6.1.8) yields

$$\frac{\partial \tilde{u}}{\partial x} + \frac{\partial \tilde{v}}{\partial y} = 0. \tag{6.1.10}$$

We proceed by substituting (6.1.6) into the momentum equation. Averaging the resulting expression over one wall wavelength yields

$$\begin{aligned}
&\overline{U_m \frac{\partial U_m}{\partial x}} + \overline{U_m \frac{\partial \tilde{u}}{\partial x}} + \overline{\tilde{u} \frac{\partial U_m}{\partial x}} + \overline{\tilde{u} \frac{\partial \tilde{u}}{\partial x}} + \overline{V_m \frac{\partial U_m}{\partial y}} + \overline{V_m \frac{\partial \tilde{u}}{\partial y}} + \overline{\tilde{v} \frac{\partial U_m}{\partial y}} + \overline{\tilde{v} \frac{\partial \tilde{u}}{\partial y}} \\
&= \frac{1}{R} \left(\overline{\frac{\partial^2 U_m}{\partial y^2}} + \overline{\frac{\partial^2 \tilde{u}}{\partial y^2}} \right).
\end{aligned}$$

Since the average of the mean flow remains unchanged and the average of the fluctuations is zero, we obtain

$$U_m \frac{\partial U_m}{\partial x} + V_m \frac{\partial U_m}{\partial y} = \frac{1}{R} \frac{\partial^2 U_m}{\partial y^2} - \left(\overline{\tilde{u} \frac{\partial \tilde{u}}{\partial x}} + \overline{\tilde{v} \frac{\partial \tilde{u}}{\partial y}} \right).$$

We notice that

$$\begin{aligned}
\tilde{u} \frac{\partial \tilde{u}}{\partial x} + \tilde{v} \frac{\partial \tilde{u}}{\partial y} &= \left(2\tilde{u} \frac{\partial \tilde{u}}{\partial x} - \tilde{u} \frac{\partial \tilde{u}}{\partial x} \right) + \tilde{v} \frac{\partial \tilde{u}}{\partial y} + \left(\tilde{u} \frac{\partial \tilde{v}}{\partial y} - \tilde{u} \frac{\partial \tilde{v}}{\partial y} \right) \\
&= 2\tilde{u} \frac{\partial \tilde{u}}{\partial x} + \tilde{v} \frac{\partial \tilde{u}}{\partial y} + \tilde{u} \frac{\partial \tilde{v}}{\partial y} - \tilde{u} \left(\frac{\partial \tilde{u}}{\partial x} + \frac{\partial \tilde{v}}{\partial y} \right) \\
&= \frac{\partial (\tilde{u}\tilde{u})}{\partial x} + \frac{\partial (\tilde{u}\tilde{v})}{\partial y} - \tilde{u} \left(\frac{\partial \tilde{u}}{\partial x} + \frac{\partial \tilde{v}}{\partial y} \right).
\end{aligned}$$

Using (6.1.10) yields

$$\tilde{u} \frac{\partial \tilde{u}}{\partial x} + \tilde{v} \frac{\partial \tilde{u}}{\partial y} = \frac{\partial (\tilde{u}\tilde{u})}{\partial x} + \frac{\partial (\tilde{u}\tilde{v})}{\partial y}.$$

Therefore

$$U_m \frac{\partial U_m}{\partial x} + V_m \frac{\partial U_m}{\partial y} = \frac{1}{R} \frac{\partial^2 U_m}{\partial y^2} - \overline{\frac{\partial (\tilde{u}\tilde{u})}{\partial x}} - \overline{\frac{\partial (\tilde{u}\tilde{v})}{\partial y}}.$$

Now

$$\overline{\frac{\partial (\tilde{u}\tilde{u})}{\partial x}} = \frac{\tilde{\alpha}}{2\pi} \int_x^{x+\frac{2\pi}{\tilde{\alpha}}} \frac{\partial (\tilde{u}\tilde{u})}{\partial x} \, \mathrm{d}x = \frac{\alpha}{2\pi} [\tilde{u}\tilde{u}]_x^{x+\frac{2\pi}{\tilde{\alpha}}} = 0.$$

Since $(\tilde{u}\tilde{u})$ is a periodic function, it returns to its original value after one wavelength, making the net change over the period zero. Therefore we obtain the following system

$$\frac{\partial U_m}{\partial x} + \frac{\partial V_m}{\partial y} = 0, \tag{6.1.11a}$$

$$U_m \frac{\partial U_m}{\partial x} + V_m \frac{\partial U_m}{\partial y} = \frac{1}{R} \frac{\partial^2 U_m}{\partial y^2} - \frac{\partial (\overline{\tilde{u}\tilde{v}})}{\partial y}. \tag{6.1.11b}$$

The system above describes the mean flow of the boundary layer, modified to account for the effects of small-amplitude wall waviness. The mean flow is influenced by the Reynolds stress, which arises from perturbations induced by the wavy surface. This Reynolds stress term results directly from the averaging process and quantifies the impact of these perturbations on the mean flow. Consequently, the Reynolds stress modifies the mean velocity profile and, therefore, the stability characteristics of the boundary layer.

To solve this system, we need to evaluate the Reynolds stress. Given the form of the perturbations described by (6.1.7), this requires solving the steady Orr-Sommerfeld equation to determine the velocity perturbations caused by the wall waviness. The steady Orr-Sommerfeld equation is given by:

$$\{(\mathrm{D}^2-\tilde{\alpha}^2)^2-\mathrm{i}\alpha R[U_m(\mathrm{D}^2-\tilde{\alpha}^2)-(U_m)''_{yy}]\}\hat{v}=0. \tag{6.1.12}$$

These perturbations are steady, spatially periodic fluctuations that reflect the shape of the wavy surface. Because the wall is not flat, solving this equation requires inhomogeneous boundary conditions which we derive in §6.2 that incorporate the effect of the wall waviness. These boundary conditions ensure that the velocity perturbations accurately represent the influence of the wavy surface on the flow, specifically satisfying the no-slip and no-penetration conditions imposed by the wall geometry.

The solution to the steady Orr-Sommerfeld equation captures how the boundary layer responds to these disturbances. The resulting velocity perturbations are then used to compute the Reynolds stress term, which is essential for understanding how wall waviness alters the mean flow and its stability properties. By solving (6.1.11) and (6.1.12) simultaneously, with the appropriate boundary conditions, we obtain the modified mean flow in the presence of the wavy surface. First, the system (6.1.11) can be reformulated into a more convenient form using a similarity transformation. To determine the similarity variable we recall from Chapter 2 that $\eta=\hat{Y}/\sqrt{X}$. Now

$$\eta=\frac{\hat{Y}}{\sqrt{X}}=\frac{Re^{\frac{1}{2}}Y}{\sqrt{X}}=\frac{Re^{\frac{1}{2}}(L^*)^{-1}y^*}{\sqrt{(L^*)^{-1}X^*}}=\frac{Re^{\frac{1}{2}}y^*}{\sqrt{L^*x^*}}=\left(\frac{U^*_\infty}{\nu^*}\right)^{\frac{1}{2}}\frac{y^*}{\sqrt{x^*}}.$$

As previously defined, the quantities are $Y = y^*/L^*$, $X = x^*/L^*$, $\hat{Y} = Re^{1/2}Y$ and $Re = U_\infty^* L^*/\nu^*$. In this analysis, the length scales are expressed in terms of the displacement thickness, such that $y = y^*/\delta^*$ and $x = x^*/\delta^*$. This yields the following similarity variable

$$\eta = y\sqrt{\frac{R}{x}}.$$

We now introduce the following

$$U_m = \frac{\partial \Psi}{\partial y}, \quad V_m = -\frac{\partial \Psi}{\partial x}, \quad \Psi = \sqrt{x/R}f(\eta). \tag{6.1.13}$$

Given the form of η, we can derive the following expressions for the relevant derivatives

$$\frac{\partial \eta}{\partial y} = \sqrt{\frac{R}{x}},$$
$$\frac{\partial \eta}{\partial x} = -\frac{\eta}{2x}.$$

Making use of (6.1.13) we obtain the following

$$U_m = \frac{\mathrm{d}f}{\mathrm{d}\eta}, \tag{6.1.14a}$$
$$V_m = -\frac{1}{2x^{\frac{1}{2}}R^{\frac{1}{2}}}f + \frac{\eta}{2x^{\frac{1}{2}}R^{\frac{1}{2}}}\frac{\mathrm{d}f}{\mathrm{d}\eta}, \tag{6.1.14b}$$
$$\frac{\partial U_m}{\partial y} = \frac{R^{\frac{1}{2}}}{x^{\frac{1}{2}}}\frac{\mathrm{d}^2 f}{\mathrm{d}\eta^2}, \tag{6.1.14c}$$
$$\frac{\partial U_m}{\partial x} = -\frac{\eta}{2x}\frac{\mathrm{d}^2 f}{\mathrm{d}\eta^2}, \tag{6.1.14d}$$
$$\frac{\partial^2 U_m}{\partial y^2} = \frac{R}{x}\frac{\mathrm{d}^3 f}{\mathrm{d}\eta^3}. \tag{6.1.14e}$$

By applying (6.1.13), the continuity equation is inherently satisfied. Substituting (6.1.14) into (6.1.11) results in the following

$$\frac{d^3 f}{d\eta^3} + \frac{f}{2}\frac{d^2 f}{d\eta^2} = x\frac{d\overline{(\tilde{u}\tilde{v})}}{dy}. \tag{6.1.15}$$

We note that $x^{\frac{1}{2}}R^{\frac{1}{2}} = Re_{x^*}^{\frac{1}{2}}$, which we can rewrite as follows

$$Re_{x^*}^{\frac{1}{2}} = \left(\frac{x^*}{\delta^*}\right)\delta.$$

Therefore

$$x^{\frac{1}{2}}R^{\frac{1}{2}} = x\delta.$$

We can rewrite (6.1.15) as follows

$$\frac{d^3 f}{d\eta^3} + \frac{f}{2}\frac{d^2 f}{d\eta^2} = \frac{R}{\delta^2}\frac{d\overline{(\tilde{u}\tilde{v})}}{dy}. \tag{6.1.16}$$

To determine the form of the right-hand side of (6.1.16), we utilise (6.1.7).

$$\begin{aligned}\frac{d\overline{(\tilde{u}\tilde{v})}}{dy} &= \frac{d}{dy}\overline{[(\hat{u}(y)e^{i\tilde{\alpha}x} + \hat{u}^\star(y)e^{-i\tilde{\alpha}x})(\hat{v}(y)e^{i\tilde{\alpha}x} + v^\star(y)e^{-i\tilde{\alpha}x})]} \\ &= \frac{\tilde{\alpha}}{2\pi}\frac{d}{dy}\int_x^{x+\frac{2\pi}{\tilde{\alpha}}}(\hat{u}\hat{v}e^{2i\tilde{\alpha}x} + \hat{u}\hat{v}^\star + \hat{u}^\star\hat{v} + \hat{u}^\star\hat{v}^\star e^{-2i\tilde{\alpha}x})\,dx \\ &= \frac{d}{dy}(\hat{u}\hat{v}^\star + \hat{u}^\star\hat{v}).\end{aligned}$$

Therefore (6.1.16) now becomes

$$\frac{f}{2}\frac{d^2 f}{d\eta^2} + \frac{d^3 f}{d\eta^3} = \frac{R}{\delta^2}\left(\frac{d\hat{u}}{dy}\hat{v}^\star + \hat{u}\frac{d\hat{v}^\star}{dy} + \frac{d\hat{u}^\star}{dy}\hat{v} + \hat{u}^\star\frac{d\hat{v}}{dy}\right). \tag{6.1.17}$$

To express the right hand side of (6.1.17) in terms of $\hat{v}$, we make use of equations (6.1.10) and

(6.1.7) which yields

$$\mathrm{i}\tilde{\alpha}\hat{u} + \frac{\mathrm{d}\hat{v}}{\mathrm{d}y} = 0, \tag{6.1.18a}$$

$$-\mathrm{i}\tilde{\alpha}\hat{u}^{\star} + \frac{\mathrm{d}\hat{v}^{\star}}{\mathrm{d}y} = 0. \tag{6.1.18b}$$

By utilising (6.1.18) we obtain the following

$$\frac{f}{2}\frac{\mathrm{d}^2 f}{\mathrm{d}\eta^2} + \frac{\mathrm{d}^3 f}{\mathrm{d}\eta^3} = \frac{\mathrm{i}R}{\tilde{\alpha}\delta^2}\left(\frac{\mathrm{d}^2\hat{v}}{\mathrm{d}y^2}\hat{v}^{\star} - \frac{\mathrm{d}^2\hat{v}^{\star}}{\mathrm{d}y^2}\hat{v}\right). \tag{6.1.19}$$

To derive the terms on the right-hand side of (6.1.19), we solve the steady Orr-Sommerfeld equation with inhomogeneous boundary conditions, which will be derived in the following section.

6.2 Modified Boundary Conditions

To derive the inhomogeneous wall conditions used to solve (6.1.12), we recall that the no-slip and no-penetration conditions at the wavy surface require

$$u(y = h(x)) = 0, \quad v(y = h(x)) = 0.$$

By decomposing the flow into a mean part (representing the average over one wall wavelength) and a fluctuating part induced by the wall waviness, we obtain:

$$u(y = h(x)) = U_m(y = h(x)) + \tilde{u}(y = h(x)) = 0,$$

$$v(y = h(x)) = V_m(y = h(x)) + \tilde{v}(y = h(x)) = 0.$$

Since h is small we can apply a Taylor series about $h=0$ which yields

$$U_m(h) = U_m(0) + \frac{\mathrm{d}U_m(0)}{\mathrm{d}y}h + \frac{\mathrm{d}^2U_m(0)}{\mathrm{d}y^2}\frac{h^2}{2} + \cdots = 0,$$
$$\tilde{u}(h) = \tilde{u}(0) + \frac{\mathrm{d}\tilde{u}(0)}{\mathrm{d}y}h + \frac{\mathrm{d}^2\tilde{u}(0)}{\mathrm{d}y^2}\frac{h^2}{2} + \cdots = 0.$$

Therefore

$$U_m(0) + h\frac{\mathrm{d}U_m(0)}{\mathrm{d}y} + \tilde{u}(0) + \frac{\mathrm{d}\tilde{u}(0)}{\mathrm{d}y}h + \cdots = 0.$$

Ignoring terms of $\mathcal{O}(\varsigma^2)$ or higher since the analysis is based on the assumption of small-amplitude wall waviness we obtain

$$U_m(0) + h\frac{\mathrm{d}U_m(0)}{\mathrm{d}y} + \tilde{u}(0) = 0,$$
$$V_m(0) + h\frac{\mathrm{d}V_m(0)}{\mathrm{d}y} + \tilde{v}(0) = 0.$$

Where we note that $\tilde{u}$ and $\tilde{v}$ are $\mathcal{O}(\varsigma)$. Given the definition of h and $\tilde{u}$ we obtain

$$U_m(0) + \varsigma(e^{\mathrm{i}\tilde{\alpha}x} + e^{-\mathrm{i}\tilde{\alpha}x})\frac{\mathrm{d}U_m(0)}{\mathrm{d}y} + \hat{u}(0)e^{\mathrm{i}\tilde{\alpha}x} + \hat{u}^{\star}(0)e^{-\mathrm{i}\tilde{\alpha}x} = 0.$$

Comparing the coefficients of $e^{\mathrm{i}\tilde{\alpha}x}$ leads to

$$\varsigma\frac{\mathrm{d}U_m(0)}{\mathrm{d}y} + \hat{u}(0) = 0. \tag{6.2.1}$$

Making use of (6.1.18) we obtain the following wall conditions used to solve (6.1.12)

$$\hat{v}(0) = 0, \quad \frac{\mathrm{d}\hat{v}(0)}{\mathrm{d}y} = \mathrm{i}\tilde{\alpha}\varsigma\frac{\mathrm{d}U_m(0)}{\mathrm{d}y}, \tag{6.2.2}$$

were $V_m \approx 0$. Given the perturbations must decay to zero far from the surface we obtain the following far field conditions used to solve (6.1.12)

$$\hat{v}(y \to \infty) \to 0, \quad \frac{\mathrm{d}\hat{v}(y \to \infty)}{\mathrm{d}y} \to 0. \tag{6.2.3}$$

To derive the wall conditions used to solve (6.1.19) recall that

$$U_m(0) + h\frac{\mathrm{d}U_m(0)}{\mathrm{d}y} + \tilde{u}(0) + \frac{\mathrm{d}\tilde{u}(0)}{\mathrm{d}y}h + \cdots = 0,$$

Taking the average over one wall wavelength yields the following

$$\overline{U_m(0)} + \overline{h\frac{\mathrm{d}U_m(0)}{\mathrm{d}y}} + \overline{\tilde{u}(0)} + \overline{h\frac{\mathrm{d}\tilde{u}(0)}{\mathrm{d}y}} + \cdots = 0.$$

Given that $\overline{U_m}(0) = U_m(0)$ and $\overline{\tilde{u}}(0) = 0$, we obtain

$$U_m(0) + \overline{h}\frac{\mathrm{d}U_m(0)}{\mathrm{d}y} + \overline{h\frac{\mathrm{d}\tilde{u}(0)}{\mathrm{d}y}} + \cdots = 0.$$

Since $\overline{h} = 0$ we obtain the following wall condition

$$U_m(0) = -\overline{h\frac{\mathrm{d}\tilde{u}(0)}{\mathrm{d}y}}.$$

We obtain a similar expression for $V_m(0)$

$$V_m(0) = -\overline{h\frac{\mathrm{d}\tilde{v}(0)}{\mathrm{d}y}}.$$

In terms of the similarity variables we obtain

$$\frac{\mathrm{d}f(0)}{\mathrm{d}\eta} = -\overline{h\frac{\mathrm{d}\tilde{u}(0)}{\mathrm{d}y}}, \quad f(0) = 2x^{\frac{1}{2}}R^{\frac{1}{2}}\overline{h\frac{\mathrm{d}\tilde{v}(0)}{\mathrm{d}y}},$$

which we can rewrite as follows

$$\frac{\mathrm{d}f(0)}{\mathrm{d}\eta} = -\overline{h\frac{\mathrm{d}\tilde{u}(0)}{\mathrm{d}y}}, \quad f(0) = \frac{2R}{\delta}\overline{h\frac{\mathrm{d}\tilde{v}(0)}{\mathrm{d}y}}.$$

For the far field condition we obtain

$$\frac{\mathrm{d}f(\eta \to \infty)}{\mathrm{d}\eta} \to 1.$$

To determine the form of the right-hand sides of both $f(0)$ and $\mathrm{d}f(0)/\mathrm{d}\eta$, we utilise (6.1.7). Therefore,

$$\begin{aligned}
\overline{h\frac{\mathrm{d}\tilde{u}(0)}{\mathrm{d}y}} &= \overline{\varsigma(e^{\mathrm{i}\tilde{\alpha}x} + e^{-\mathrm{i}\tilde{\alpha}x})\left(\frac{\mathrm{d}\hat{u}(0)}{\mathrm{d}y}e^{\mathrm{i}\tilde{\alpha}x} + \frac{\mathrm{d}\hat{u}^{\star}(0)}{\mathrm{d}y}e^{-\mathrm{i}\tilde{\alpha}x}\right)} \\
&= \varsigma\frac{\tilde{\alpha}}{2\pi}\int_{x}^{x+\frac{2\pi}{\tilde{\alpha}}}\left(\frac{\mathrm{d}\hat{u}(0)}{\mathrm{d}y}e^{2\mathrm{i}\tilde{\alpha}x} + \frac{\mathrm{d}\hat{u}^{\star}(0)}{\mathrm{d}y} + \frac{\mathrm{d}\hat{u}(0)}{\mathrm{d}y} + \frac{\mathrm{d}u^{\star}(0)}{\mathrm{d}y}e^{-2\mathrm{i}\tilde{\alpha}x}\right)\mathrm{d}x \\
&= \varsigma\left(\frac{\mathrm{d}\hat{u}^{\star}(0)}{\mathrm{d}y} + \frac{\mathrm{d}\hat{u}(0)}{\mathrm{d}y}\right).
\end{aligned}$$

Similarly we obtain

$$\overline{h\frac{\mathrm{d}\tilde{v}(0)}{\mathrm{d}y}} = \varsigma\left(\frac{\mathrm{d}\hat{v}^{\star}(0)}{\mathrm{d}y} + \frac{\mathrm{d}\hat{v}(0)}{\mathrm{d}y}\right).$$

Therefore system (6.1.19) is solved subject to

$$\begin{gathered}
\frac{\mathrm{d}f(\eta=0)}{\mathrm{d}\eta} = -\frac{\varsigma\mathrm{i}}{\tilde{\alpha}}\left(\frac{\mathrm{d}^2\hat{v}(0)}{\mathrm{d}y^2} - \frac{\mathrm{d}^2\hat{v}^{\star}(0)}{\mathrm{d}y^2}\right), \quad f(0) = \frac{2R\varsigma}{\delta}\left(\frac{\mathrm{d}\hat{v}^{\star}(0)}{\mathrm{d}y} + \frac{\mathrm{d}\hat{v}(0)}{\mathrm{d}y}\right), \\
\frac{\mathrm{d}f(\eta \to \infty)}{\mathrm{d}\eta} \to 1. \quad (6.2.4)
\end{gathered}$$

6.3 The Solution Process

To obtain the modified mean flow, we employ an iterative procedure. The process begins by solving equation (6.1.12) with the boundary conditions (6.2.2) and (6.2.3), using the Blasius mean flow as an initial approximation. To solve (6.1.12), we rewrite it as a system of ODEs. Let

$$\begin{aligned}
z_1 &= \hat{v}, \\
z_2 &= \frac{\mathrm{d}z_1}{\mathrm{d}y} = \frac{\mathrm{d}\hat{v}}{\mathrm{d}y}, \\
z_3 &= \frac{\mathrm{d}z_2}{\mathrm{d}y} = \frac{\mathrm{d}^2\hat{v}}{\mathrm{d}y^2}, \\
z_4 &= \frac{\mathrm{d}z_3}{\mathrm{d}y} = \frac{\mathrm{d}^3\hat{v}}{\mathrm{d}y^3}.
\end{aligned}$$

We define the vector Z as

$$Z = [z_1, z_2, z_3, z_4]^T.$$

The system of ODEs becomes

$$\frac{\mathrm{d}Z}{\mathrm{d}y} = [z_2, z_3, z_4, W]^T, \tag{6.3.1}$$

where

$$W = (2\tilde{\alpha}^2 + \mathrm{i}\tilde{\alpha}RU_m)z_3 - \left(\tilde{\alpha}^4 + \mathrm{i}\tilde{\alpha}^3RU_m + \mathrm{i}\tilde{\alpha}R\frac{\mathrm{d}^2U_m}{\mathrm{d}y^2}\right)z_1.$$

The boundary conditions for this system are

$$z_1(0) = 0, \quad z_2(0) - \mathrm{i}\tilde{\alpha}\varsigma\frac{\mathrm{d}U_m(0)}{\mathrm{d}y} = 0, \quad z_1(y\to\infty)\to 0, \quad z_2(y\to\infty)\to 0. \tag{6.3.2}$$

We solve the system of ODEs using MATLAB's BVP4C solver, which handles boundary value problems effectively. The solution provides the necessary data to solve equation (6.1.19) with the boundary condition (6.2.4). We now rewrite (6.1.19) as

$$\frac{f}{2}\frac{\mathrm{d}^2 f}{\mathrm{d}\eta^2} + \frac{\mathrm{d}^3 f}{\mathrm{d}\eta^3} = \frac{\mathrm{i}R}{\tilde{\alpha}\delta^2}(z_3 z_1^\star - z_3^\star z_1), \tag{6.3.3}$$

with the boundary conditions

$$\frac{\mathrm{d}f(\eta=0)}{\mathrm{d}\eta} = -\frac{\mathrm{i}\varsigma}{\tilde{\alpha}}(z_3(0)-z_3^\star(0)), \quad f(0) = \frac{2R\varsigma}{\delta}(z^\star(0)+z_2(0)), \quad \frac{\mathrm{d}f(\eta\to\infty)}{\mathrm{d}\eta} \to 1. \quad (6.3.4)$$

We solve this equation using MATLAB's BVP4C solver to obtain the modified mean flow. This solution is then used to update the initial mean flow approximation. The iterative process continues until the solution converges to the desired level of accuracy. Specifically, convergence is achieved when the difference between the current and previous displacement thicknesses is on the order of 10^{-7}. At this level of accuracy, the value of $f''_{\eta\eta}(0)$ remains unchanged, ensuring that the solution has reached a stable and accurate state.

6.4 Modified Basic Flow Solutions-Blasius

In this section, we present the basic flow solutions and analyse the modified mean flow for various values of ς. To facilitate direct comparisons with the results of Lessen & Gangwani (1976), we deviate from the analysis in Chapter 4 by setting $\delta = 1$. With this choice, we obtain a critical Reynolds number of $R_{crit} = 303.50$ for the Blasius mean flow. For the analysis that follows, we will use $R = 300$ as our reference Reynolds number. This selection is useful because it allows us to determine whether an increase in wall wave amplitude leads to destabilisation by starting with a flow that is initially stable. To extend the analysis to Reynolds numbers other than $R = 300$, we adopt the scalings introduced by Lessen & Gangwani (1976):

$$\varsigma_{\mathrm{d}} = \varsigma\left(\frac{300}{R}\right), \quad \tilde{\alpha}_{\mathrm{d}} = \tilde{\alpha}\left(\frac{R}{300}\right). \quad (6.4.1)$$

The scalings given by (6.4.1) indicate that as we move downstream (corresponding to an increase in R), the influence of wall waviness on the linear stability of the boundary layer becomes less significant. This implies that the boundary layer becomes less sensitive to wall irregularities further downstream. Additionally, as R increases, the wavelength of the wall waviness becomes

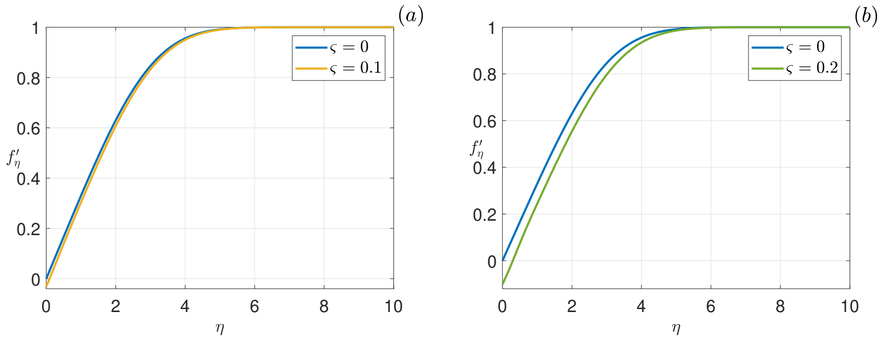

Figure 6.1: Comparison of the modified streamwise velocity profile with the Blasius solution. The Blasius velocity profile corresponds to $\varsigma = 0$, while the modified profiles are shown for $R = 300$ and $\tilde{\alpha} = 1$ at (a) $\varsigma = 0.1$ and (b) $\varsigma = 0.2$.

shorter, meaning the flow encounters more frequent surface oscillations. These shorter wavelengths result in more rapid changes in surface geometry as we move downstream. Overall, these scalings are valuable because they enable us to analyse the linear stability characteristics of the boundary layer at various locations along the surface, providing a consistent framework for understanding how wall waviness influences the flow stability at different Reynolds numbers.

From Figure 6.1, it is evident that the streamwise velocity at the wall, $f'_\eta(0)$, becomes negative as ς increases. This behaviour is a direct consequence of the inhomogeneous boundary conditions imposed by the wall waviness. Additionally, the modified velocity profile shifts to the right, with the magnitude of the shift increasing as ς increases, indicating a thickening of the boundary layer. These results are consistent with the findings presented by Lessen & Gangwani (1976).

In Figure 6.2, we compare the curvature of the modified mean flow with the Blasius mean flow. When ς is non-zero, a point of inflection appears in the modified mean flow, becoming more pronounced as ς increases. The presence of an inflection point in the mean flow is expected to influence the linear stability characteristics of the flow. Additionally, we observe that the curvature at the wall is zero for all values of ς. This contrasts with the findings of Lessen & Gangwani (1976), who predicted a point of inflection in the modified mean flow but also reported non-zero curvature at the wall. We argue that this is incorrect, as non-zero curvature at the wall would violate the boundary conditions.

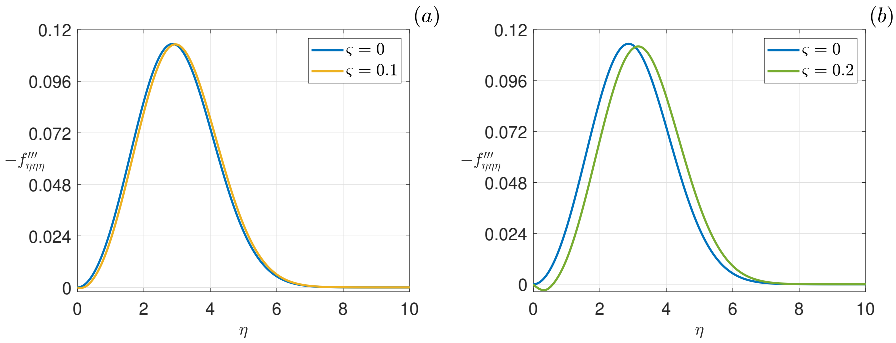

Figure 6.2: Comparison of the curvature of the modified mean flow with the Blasius mean flow. The Blasius mean flow corresponds to $\varsigma = 0$, while the modified mean flow curvatures are presented for $R = 300$ and $\tilde{\alpha} = 1$ at (a) $\varsigma = 0.1$ and (b) $\varsigma = 0.2$.

6.5 Linear Stability-Blasius

We proceed by analysing the linear stability of the modified mean flow for various values of ς. This analysis is conducted using the numerical methods outlined in Chapter 4. We begin by analysing how the sign of α_i changes with increasing ς. The results of this analysis are summarised in Table 6.1.

Table 6.1: The values of α for various values of ς were $\omega = 0.05$, $R = 300$ and $\tilde{\alpha} = 1$.

ς	α
0	$0.1327 + 0.0022i$
0.05	$0.1341 + 0.0018i$
0.1	$0.1380 + 0.0008i$
0.15	$0.1436 - 0.0004i$
0.2	$0.1502 - 0.0011i$

From Table 6.1, we observe that α_i undergoes a sign change, becoming negative as ς increases. This behaviour suggests that the flow is becoming destabilised. These findings are in direct agreement with the results presented by Lessen & Gangwani (1976), who performed a temporal stability analysis and showed that the wave speed c becomes positive with increasing

ς, further indicating destabilisation. To further support our claim that surface waviness has a destabilising influence on boundary layer flows induced by an external oncoming flow, we present the growth rates for various values of ς at the reference Reynolds number $R = 300$.

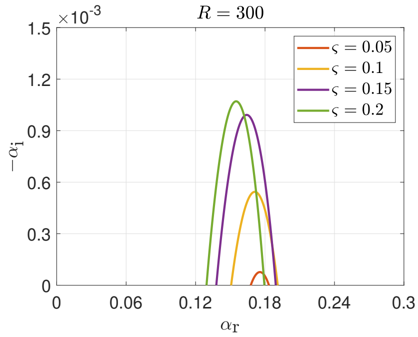

Figure 6.3: The growth rate, defined as $-\alpha_i$, is illustrated against α_r for a range of values ς were $R = 300$ and $\tilde{\alpha} = 1$.

We find that the amplitude of the growth rate increases significantly with increasing ς, indicating destabilisation, as shown in Figure 6.3. Additionally, no positive growth rates are observed when $\varsigma = 0$, consistent with the flow being stable at this amplitude. Utilising the scalings given by (6.4.1), we conducted a similar analysis for $R = 600$. As expected, we find that the flow is unstable at all amplitudes, with $\alpha_i < 0$ for all values of ς. In Figure 6.4, we present the growth rates for the two wavenumbers $\tilde{\alpha} = 1$ and $\tilde{\alpha} = 1/2$. In both cases, we observe a significant increase in the amplitude of the growth rate, further supporting our claim that surface waviness leads to flow destabilisation.

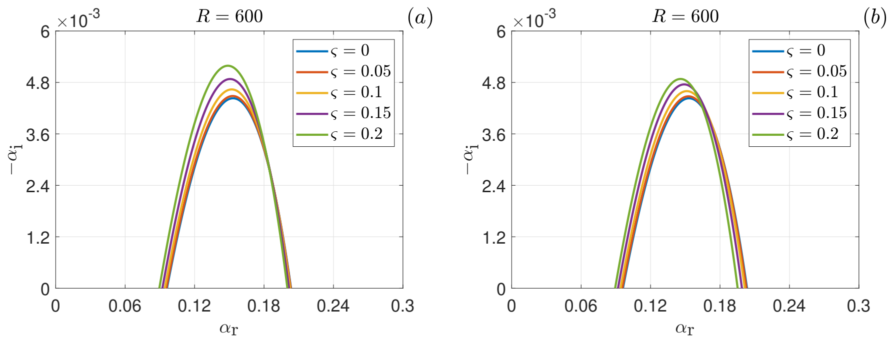

Figure 6.4: The growth rate, defined as $-\alpha_i$, is illustrated against α_r for a range of values ς were $R = 600$ for (a) $\tilde{\alpha} = 1$ and (b) $\tilde{\alpha} = 1/2$.

6.6 Modified Basic Flow Solutions-Sakiadis

Before analysing how surface waviness affects the boundary layer induced by a surface translating at a constant velocity, we first address the changes in the boundary conditions. Due to the constant surface velocity, the system described by (6.1.1) is now solved subject to the following conditions

$$u^*(y^* = h^*(x^*)) = U_w^*, \quad v^*(y^* = h^*(x^*)) = 0, \quad u^*(y^* \to \infty) \to 0.$$

We note that while the boundary conditions used to solve (6.1.12) remain unchanged, the conditions for solving (6.1.19) are different, as discussed in §3.1. To derive these new conditions, the Taylor expansion used in §6.2 now becomes:

$$U_m(0) + h\frac{\mathrm{d}U_m(0)}{\mathrm{d}y} + \tilde{u}(0) + h\frac{\mathrm{d}\tilde{u}(0)}{\mathrm{d}y} + \cdots = 1.$$

Taking the average over one wall wavelength yields the following

$$U_m(0) = -\overline{h\frac{\mathrm{d}\tilde{u}(0)}{\mathrm{d}y}} + 1.$$

Similarly we obtain

$$V_m(0) = -\overline{h\frac{\mathrm{d}\tilde{v}(0)}{\mathrm{d}y}}.$$

In terms of the similarity variables the boundary conditions used to solve (6.1.19) are now given by

$$\frac{\mathrm{d}f(0)}{\mathrm{d}\eta} = -\overline{h\frac{\mathrm{d}\tilde{u}(0)}{\mathrm{d}y}} + 1, \quad f(0) = \frac{2R}{\delta}\overline{h\frac{\mathrm{d}\tilde{v}(0)}{\mathrm{d}y}}, \quad \frac{\mathrm{d}f(\eta \to \infty)}{\mathrm{d}\eta} \to 0.$$

Therefore we obtain

$$\frac{\mathrm{d}f(\eta=0)}{\mathrm{d}\eta} = -\frac{\varsigma \mathrm{i}}{\tilde{\alpha}}\left(\frac{\mathrm{d}^2\hat{v}(0)}{\mathrm{d}y^2} - \frac{\mathrm{d}^2\hat{v}^\star(0)}{\mathrm{d}y^2}\right) + 1, \quad f(0) = \frac{2R\varsigma}{\delta}\left(\frac{\mathrm{d}\hat{v}^\star(0)}{\mathrm{d}y} + \frac{\mathrm{d}\hat{v}(0)}{\mathrm{d}y}\right),$$
$$\frac{\mathrm{d}f(\eta\to\infty)}{\mathrm{d}\eta} \to 0. \quad (6.6.1)$$

Therefore to obtain the modfied mean flow we solve (6.1.12) with the conditions (6.2.2) and (6.2.3), using the Sakiadis mean flow. This provides the necessary information used to solve (6.1.19) with the condition (6.6.1) where we solve the equations iteratively using the procedure outlined in §6.3. On setting $\delta = 1$, one finds that the critical Reynolds number for this flow configuration is $R_{crit} = 2205.29$. In Chapter 4, we demonstrated that an increase in the roughness parameter leads to an increase in the critical Reynolds number, indicating stabilisation of the flow. Therefore, we select $R = 2300$ as a reference point for the following analysis. This choice allows us to determine whether an increase in ς leads to stabilisation, given that the flow is unstable at $R = 2300$. We begin by analysing how surface waviness modifies the mean flow.

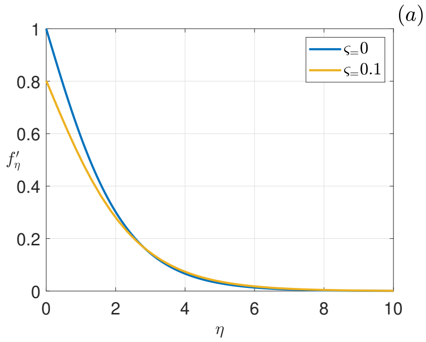

Figure 6.5: A comparison of the modified streamwise velocity profile with the Sakiadis velocity profile for $R = 2300$ and $\tilde{\alpha} = 1$, where the case $\varsigma = 0$ corresponds to the Sakiadis solution. Results are shown for (a) $\varsigma = 0.1$ and (b) $\varsigma = 0.15$.

In Figure 6.5, we compare the modified mean flow with the Sakiadis mean flow. It is evident that increasing ς results in a decrease in the streamwise velocity component at the wall, $f'_\eta(0)$. This observation is consistent with the results discussed in §3.2 and §3.3.

We were unable to obtain solutions for $\varsigma = 0.2$. This difficulty arises because ς is related to the Reynolds number R as shown in equation (6.4.1), where ς^* is expressed in terms of the displacement thickness δ^*. As we move downstream (corresponding to an increase in R), the boundary layer becomes less sensitive to wall irregularities. In contrast, at lower Reynolds numbers the boundary layer is more sensitive to these irregularities. Furthermore, in Section §3.3, we obtained $|\overline{f''_{\eta\eta}}(0)| = 0.2413$ for $a = 0.2$ (see Table 3.1). Using the methods presented here, we obtained a similar value of $|f''_{\eta\eta}(0)| = 0.2487$ for $\varsigma = 0.15$. This suggests that $|f''_{\eta\eta}(0)|$ approaches zero for smaller values of the surface waviness amplitude when the amplitude is expressed in terms of δ^*. Based on these findings, it is reasonable to conclude that our analysis is limited to the case of $\varsigma = 0.15$ for this particular Reynolds number.

6.7 Linear Stability - Sakiadis

In this section, we analyse the linear stability of the modified mean flow solutions for the boundary layer induced by the translation of a wavy surface for various values of ς. To determine the onset of linear instability, we once again apply the numerical methods described in Chapter 4. We begin by analysing the sign of α_i to determine the stability characteristics at the reference Reynolds number. The results of this analysis are summarised in Table 6.2.

Table 6.2: The values of α for various values of ς were $\omega = 0.1$, $R = 2300$ and $\tilde{\alpha} = 1$.

ς	α
0	$0.1356 - 0.0001\text{i}$
0.05	$0.1462 - 0.0000\text{i}$
0.1	$0.1718 + 0.0011\text{i}$
0.15	$0.2035 + 0.0041\text{i}$

We observe that α_i changes sign and becomes positive as ς increases, indicating that the flow has stabilised. Due to this stabilisation, we were unable to obtain positive growth rates for this particular Reynolds number. To further investigate the linear stability characteristics of this flow configuration, we analyse the growth rates for $R = 3500$ and for the two wavenumbers $\tilde{\alpha} = 1$ and $\tilde{\alpha} = 1/2$. In this analysis, we utilise the scalings given by (6.4.1). As discussed in §6.4, an increase in R makes the boundary layer less sensitive to wall irregularities. Consequently, we were able to obtain solutions for $\varsigma = 0.2$.

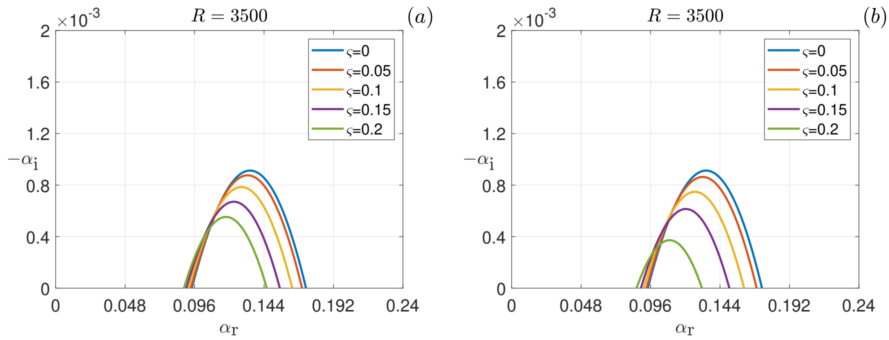

Figure 6.6: The growth rate, defined as $-\alpha_i$, is illustrated against α_r for a range of values ς were $R = 3500$ for (a) $\tilde{\alpha} = 1$ and (b) $\tilde{\alpha} = 1/2$.

In Figure 6.6, we present the growth rates for various values of ς for the wavenumbers $\tilde{\alpha} = 1$ and $\tilde{\alpha} = 1/2$. In both cases, we observe a reduction in the amplitude of the growth rate, indicating stabilisation of the flow. These results agree qualitatively with those discussed in §4.4, as shown in Figure 4.1. Based on the analysis conducted here, surface roughness can be exploited for laminar flow control in boundary layers induced by surface translation. However, the opposite behaviour is observed for boundary layers induced by an external oncoming flow interacting with a fixed plate, where the presence of a wavy surface leads to destabilisation.

In this study, we solved the two-dimensional boundary layer equations in the presence of small-amplitude surface waviness, considering two distinct cases. We first analysed how surface roughness affects boundary layers induced by an external oncoming flow, aiming to reproduce the results of Lessen & Gangwani (1976). To compute the response of these boundary layers to surface waviness, we solved the steady Orr-Sommerfeld equation subject to inhomogeneous boundary conditions. The resulting perturbations were used to evaluate the Reynolds stress, which modifies the mean flow. The modified mean flow was then obtained by solving the Reynolds-averaged boundary layer equations numerically. In this case, we successfully reproduced the basic flow solutions of Lessen & Gangwani (1976) and demonstrated that the modified streamwise velocity at the wall becomes negative for $\varsigma > 0$. This behavior arises directly from the inhomogeneous boundary conditions. Additionally, an increase in boundary layer thickness is observed. We also examined the curvature of the modified mean flow and observed a point of inflection, consistent with the findings of Lessen & Gangwani (1976). However, we found their prediction of non-zero curvature at the wall for to be incorrect, as it would violate the boundary conditions. Our linear stability analysis, using the methods from Chapter 4, showed that the imaginary part of the disturbance wavenumber α_{i} becomes negative as ς increases for a Reynolds number of $R = 300$, suggesting destabilisation. This conclusion was further supported by an increase in the amplitude of the growth rates. A similar trend was observed for $R = 600$. We thus demonstrated that surface waviness has a destabilising effect on boundary layers induced by an external oncoming flow, in agreement with the results of Lessen & Gangwani (1976).

In the second case, we analysed how surface waviness affects the boundary layer induced by a surface translating at a constant velocity in a quiescent fluid. We showed that an increase in ς leads to a decrease in the streamwise velocity component at the wall, consistent with the results presented in §3.2 and §3.3. Our linear stability analysis at a Reynolds number of $R = 2300$ revealed that α_{i} becomes positive with increasing ς, indicating stabilisation. This conclusion was reinforced by analysing the growth rates for $R = 3500$ and observing a decrease in the growth rates for the two wavenumbers $\tilde{\alpha} = 1$ and $\tilde{\alpha} = 1/2$. These findings demonstrate that surface waviness has a stabilising influence on boundary layers induced by a translating surface. The results are in qualitative agreement with those presented in §4.4. These results provide further evidence that surface roughness can be exploited for laminar flow control in boundary layers induced by surface translation.

Chapter 7

Discussions, Conclusions and Future Directions

We have assessed the onset of instability of the flow induced by the translation of a rough surface. This flow is susceptible to disturbances in the form of TS waves. Our analysis, both numerical and analytical, reveals that this flow is stabilised in the presence of surface roughness.

In a similar fashion to Garrett *et al.* (2016), who considered an associated study concentrating on flows over rotating disks, we find that in the instances when the roughness profile is sinusoidal in nature then the base flow profiles are periodic in the streamwise direction. Ensuring that our analysis is conducted sufficiently far enough downstream of the leading edge, a suitable averaging procedure has been adopted to arrive at basic states that are then invariant in the streamwise direction. This approach is analogous to that presented by Garrett *et al.* (2016) although our findings suggest that there are, perhaps, some shortcomings in the base flow results presented in that study.

We have considered the linear stability characteristics of our averaged base flow profiles via three different means. In the first instance, we adopted a standard Orr-Sommerfeld, LSA, approach. Our findings show that as the value of the surface roughness parameter increases, disturbance growth rates decrease, critical Reynolds numbers increase, and that the total mechanical energy of the system decreases. These findings support the conclusion that for flows generated by the translation of a moving wall, surface roughness has the effect of delaying the onset of instability.

Our second approach, the large Reynolds number asymptotic analysis presented in Chapter 5, produces excellent results when compared to our numerical findings. This lower branch study supports the conclusion that the presence of surface roughness inhibits the growth of the TS instability waves. Our analysis shows that the relevant asymptotic scalings for this problem are different to those of the Blasius boundary layer problem. This finding is consistent with the analysis of Tsou *et al.* (1966) who demonstrated that the critical layer for these surface translation problems moves closer to the wall when compared to problems where the boundary-layer has been generated by the presence of an oncoming flow.

In the third instance we adopted a quasi-spatial approach motivated by the quasi-steady studies of Morgan & Davies (2020*b*). Our findings once again suggest that an increase in the roughness parameter leads to flow stabilisation. In fact, the results from this quasi-spatial analysis show an even greater level of flow stabilisation, both in terms of growth rates and critical Reynolds numbers, when compared to our LSA findings presented in §4.5. Although we have not explored a Floquet-type (periodic in space, not time) analysis here we are confident, given the results presented by Morgan and coworkers, that our quasi-spatial results would very closely reproduce the findings owing from such an analysis.

In Chapter 6 we analysed the linear stability of the steady flow by considering an alternative approach motivated by the study of Lessen & Gangwani (1976). Once again we adopt a suitable averaging procedure, however the methods used to obtain the basic flow solutions differ. Our findings reveal that an increase in the roughness parameter leads to a decrease in the disturbance growth rates for selected values of the Reynolds number which suggests flow stabilisation. Using this approach we also considered how surfaces roughness influences the boundary layer induced by an external oncoming flow. Our findings show that an increase in the roughness parameter leads to an increase in the disturbance growth rates which suggests destabilisation in agreement with the findings of Lessen & Gangwani (1976).

Our findings, that surface roughness acts to delay the onset of linear instability in boundary-layer flows that are induced by surface motion, are qualitatively consistent with the results presented by, for example, Cooper *et al.* (2015), Garrett *et al.* (2016), Alveroglu *et al.* (2016), and Özkan *et al.* (2017).

Each of the aforementioned studies considers variants of the rotating disk boundary-layer problem whereby the fluid motion is induced by the rotation of a rough disk. The problem we have considered here is in some sense similar, in that the fluid motion is being induced by the translation of the rough surface. Having said that, our findings are opposed to the results presented by, for example, Levchenko & Solov'ev (1972), Kachanov *et al.* (1974), and Lessen & Gangwani (1976), who considered the presence of surface roughness in boundary layers that are induced by the presence of an external oncoming flow. Our results, therefore, suggest that surface roughness could be exploited for laminar flow control purposes for specific classes of boundary-layer flows, those induced by surface translation/rotation. Clearly, this hypothesis can only truly be tested with detailed experimental investigations. Having said that, our finding of double periodicity of the base flow quantities is already qualitatively supported by the experimental findings of Le Palec *et al.* (1990). It remains to compare the results from our linear stability analyses with findings from experiments.

Thus far we have only modeled the rough surface using a simple sinusoidal wave. Since any dependence in the streamwise coordinate is lost upon averaging over one wall wavelength we could model the rough surface to be any combination of sinusoidal waves provided the function remains oscillatory, see Harris (2013). By doing this we could develop a roughness model that better represents surfaces that are observed in either the natural world or an industrial setting. Using the notation introduced in Chapter 2, Harris (2013) analysed a square wave represented by the function

$$s^*(x^*) = A^* \sum_{n=1}^{N} \frac{1}{2n-1} \sin\left(\frac{(2n-1)\pi x^*}{\gamma^*}\right). \tag{7.0.1}$$

The corresponding surface, when $N = 3$, is shown in Figure 7.1.

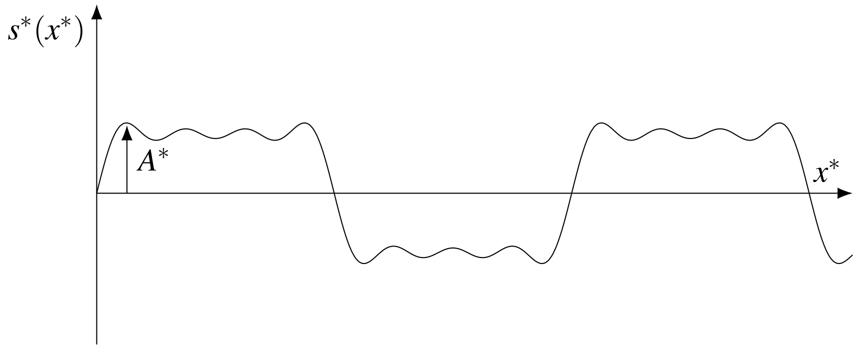

Figure 7.1: Schematic diagram illustrating the variation of the periodic surface $s^*(x^*)$, defined by equation (7.0.1), as a function of the streamwise coordinate for $N = 3$.

Note that in this instance $\sigma_0 = \sigma(\xi = 0) \neq 1$. Similar to the approach in Garrett *et al.* (2016), Harris (2013) applied the function (7.0.1) and solved the resulting equations using the commercial NAG routine D03PEF. This routine solves PDEs by employing the method of lines, converting the PDEs into a system of ODEs in the wall-normal direction, which are then solved using a backward difference method. However, substituting the sinusoidal function with the square wave described by (7.0.1) significantly increased the computation time and reduced the reliability of the NAG routine. As a result, full datasets could not be obtained due to frequent crashes, and any results produced were inconclusive. Consequently, Harris (2013) opted to use the simpler sinusoidal profile as a model for roughness.

We successfully obtained solutions using the Keller-Box method, but restricted our analysis to the case where $N = 3$ and $a \leq 0.15$. Increasing these values caused the scheme to fail to converge. We argue that this failure is not due to flow separation. For instance, for the simple sinusoidal profile, we obtained $|\overline{f''_{\eta\eta}}(0)| = 0.2960$ in the case when $a = 0.15$ (see Table 3.1), whereas for the surface described by equation (7.0.1) with $N = 3$, we obtained $|\overline{f''_{\eta\eta}}(0)| =$

0.3530 for the same corresponding value of a (see Table C.1). This indicates that $|\overline{f''_{\eta\eta}}(0)|$ approaches zero more slowly for the square wave profile. However, for larger values of N, the gradient of the square wave at the origin tends to an infinite value, which causes the scheme to fail to converge at this point and all other points where infinite positive (or negative) gradients appear in the wall profile. Once again, we observed that surface roughness delays the onset of linear instability. A summary of these results is provided in C. The function can be easily modified to represent a triangle wave or a sawtooth wave, as long as it remains oscillatory. Furthermore, the analysis could be extended to include randomized surface roughness, such as a Fourier series with a randomized phase spectrum, as described in Lu *et al.* (2020).

Thus far, we have employed the parallel flow approximation to analyse the onset of linear instability for flows generated by the translation of rough surfaces. This approach simplifies the analysis by neglecting the streamwise variation of the mean flow thus reducing both the complexity and dimensionality of the governing system of linear disturbance equations. An alternative approach to analysing the onset of linear instability is to use the parabolised stability equations (PSE). This method accounts for the streamwise variation of the mean flow (i.e., non-parallel effects) Bertolotti *et al.* (1992). The PSE approach also captures the evolution of boundary layer disturbances, an idea first introduced by Floryan & Saric (1982). In this method, the solution is obtained by marching in the streamwise direction, with the scheme initialized using solutions from a local analysis. To derive the PSE equations, the perturbations are decomposed as follows:

$$[\tilde{u}(x,t),\tilde{v}(x,t),\tilde{p}(x,t)] = [\hat{u}(x,y),\hat{v}(x,y),\hat{p}(x,y)]\exp\left[\mathrm{i}\left(\int_{x_0}^{x}\alpha(\tilde{x})\mathrm{d}x+\beta z-\omega t\right)\right],$$

where α is now a slowly varying function of x, distinguishing this approach from the Orr-Sommerfeld formulation.

The PSE method has been successfully applied to study how surface roughness affects boundary layers induced by an external oncoming flow, see, for example Wie & Malik (1998). Therefore, we are confident that PSE can be used to analyse flows induced by the translation of rough surfaces. After performing a PSE analysis, a natural next step is to conduct a BiGlobal stability analysis. BiGlobal analyses assumes homogeneity in the third spatial dimension and considers perturbations of the form:

$$\tilde{q}(x,t) = \hat{q}(x,y)e^{\mathrm{i}(\beta z - \omega t)}.$$

Substituting this expression into the linearized Navier-Stokes equations results in a two -dimensional eigenvalue problem. While we will not delve into the details here, a comprehensive summary of BiGlobal approaches can be found in the work of Theofilis (2003). Finally, a global stability analysis can be explored by conducting time-independent simulations of the Navier-Stokes equations. In particular, Morgan (2018) examined the rough rotating disk boundary layer investigated by Garrett *et al.* (2016) and argued that such simulations allow for the direct imposition of radially anisotropic surface roughness without modifying the base flow or relying on periodic surface modeling. It is important to emphasize that the techniques discussed above — PSE, BiGlobal anlyses, and global analyses — should be combined with experimental data to achieve a comprehensive understanding of the flow induced by the translation of a rough surface.

As discussed previously, surface roughness can potentially be exploited for laminar flow control in boundary layer flows induced by surface translation or rotation. However, this is not the case for boundary layers induced by an external oncoming flow. A natural extension of the work presented in this thesis would be to analyse a continuously moving surface within a parallel free stream, incorporating the effects of surface roughness. Abdelhafez (1985) investigated this particular flow configuration for a smooth boundary. Later, Lin & Huang (1994) extended this work by examining the flow and heat transfer over plane surfaces moving parallel or in reverse to the free stream. Including surface roughness in such flow configurations would enhance our understanding of how wall irregularities affect boundary layer stability more broadly.

Appendix A

Non-Constant Wall Velocity

The work presented in this thesis has focused on the class of boundary layer flows induced by translation where the wall velocity varies. This generalized case has numerous industrial applications, such as the production of thin sheets and fibers across a range of materials (see Hanevy *et al.* (2024)). Using the notation introduced in Chapter 2, the boundary layer equations governing this class of flows are given by

$$\frac{\partial u_0}{\partial X} + \frac{\partial v_0}{\partial \hat{Y}} = 0, \tag{A.0.1a}$$

$$u_0 \frac{\partial u_0}{\partial X} + v_0 \frac{\partial u_0}{\partial \hat{Y}} + \frac{\sigma'_X}{\sigma} u_0^2 = \sigma^2 \frac{\partial^2 u_0}{\partial \hat{Y}^2}, \tag{A.0.1b}$$

where the system is solved subject to the conditions

$$u_0(\hat{Y} = 0) = \frac{U_w(X)}{\sigma(X)}, \quad v_0(\hat{Y} = 0) = 0, \quad u_0(\hat{Y} \to \infty) \to 0. \tag{A.0.2}$$

In a similar fashion to the work presented in §3.4 we assume (A.0.1) admits self similar solutions and introduce the following similarity coordinate

$$\tau = \frac{\hat{Y}}{g}\sqrt{\frac{U_w}{X\sigma}}$$

and the streamfunction $\psi = g\sqrt{U_w X}/\sigma f(\tau)$, where g is a function of X to be determined. Given the above we obtain the following velocity components

$$\begin{aligned} u_0 &= \frac{\partial \psi}{\partial \hat{Y}} = \left(\frac{U_w}{\sigma}\right) f'_\tau, \\ v_0 &= -\frac{\partial \psi}{\partial X} = g\sqrt{\frac{U_w X}{\sigma}}(\tau f'_\eta H_- - f H_+). \end{aligned}$$

Upon substitution into (A.0.1) yields

$$Xg^2[-H_+ f f''_{\tau\tau} + U_w^{-1}(U_w)'_X (f'_\tau)^2] = \sigma^2 f'''_{\tau\tau\tau}.$$

To determine self similarity it must be the case that

$$Xg^2 H_+ = c_1\sigma^2, \tag{A.0.3a}$$

$$Xg^2 U_w^{-1}(U_w)'_X = c_2\sigma^2, \tag{A.0.3b}$$

where the constants c_1 and c_2 ensure self similarity. Rearranging (A.0.3b) yields

$$g^2 = c_2\sigma^2 U_w[X(U_w)'_X]^{-1}.$$

Substituting into (A.0.3a) yields the following ODE

$$U_w \frac{\mathrm{d}^2 U_w}{\mathrm{d}X^2} + \gamma \left(\frac{\mathrm{d}U_w}{\mathrm{d}X} \right)^2 - SU_w \frac{\mathrm{d}U_w}{\mathrm{d}X} = 0, \tag{A.0.4}$$

where $S = [\ln(\sigma)]'_X$ and $\gamma = 2(c_1 - c_2/c_2)$. We observe that the case $c_1 = 0$ corresponds to $\gamma = -2$, for which no real solutions exist. This outcome is analogous to the Falkner-Skan problem in the limit as $m \to -1$, where the flow cannot be determined in a diverging channel due to the rapid deceleration of the free-stream velocity. In contrast, the case $c_2 = 0$ corresponds to $\gamma \to \infty$, where it is clear that U_w remains constant (see §3.4). Therefore, the class of boundary layer flows discussed here generalizes the boundary layer flows induced by translation with constant wall velocity. Considering the ODE described by (A.0.4), two cases arise. For the first case, when $\gamma = -1$, substituting $R = [\ln(U_w)]'_X$ into (A.0.4) gives

$$\frac{\mathrm{d}R}{\mathrm{d}X} - SR = 0.$$

Therefore $R = k\sigma$ where k is a constant of integration and it follows that

$$(U_w)'_X = kU_w\sigma. \tag{A.0.5}$$

For the case $\gamma \neq -1$, substitution of $R = (1+\gamma)U_w^{1+\gamma}[\ln(U_w)]'_X$ leads to

$$(U_w)'_X = \frac{k\sigma}{(1+\gamma)U_w^{\gamma}}. \tag{A.0.6}$$

We can rewrite the ODE as follows

$$W'_X = k\sigma, \tag{A.0.7}$$

where $W = U_w^{1+\gamma}$. To determine self similar solutions we choose to specify either the wall velocity, U_w and calculate s or specify s and determine the required form of U_w. If we fix s we can determine U_w like so

$$U_w = \begin{cases} Ce^{k\mathcal{I}} & \gamma = -1 \\ (C + k\mathcal{I})^{\frac{1}{1+\gamma}} & \gamma \neq -1, \end{cases}$$

where C is a constant of integration and

$$\mathcal{I} = \int \sigma(X)\,\mathrm{d}X$$

Thus, for any fixed s, the form of U_w for any γ can be determined by integrating σ. When $\gamma \geq -1$, it is evident that the surface is accelerating, whereas for $\gamma < -1$, the surface is decelerating. This class of boundary layer flows is particularly useful for modeling deforming surfaces, such as surface thinning or thickening Hanevy *et al.* (2024). Additionally, when $c_1 > 0$, defining $F(\zeta) = \sqrt{c_1} f(\tau)$ with $\zeta = \sqrt{c_1}\tau$ leads to $F'_\zeta = f'_\tau$, resulting in the following ODE

$$F'''_{\zeta\zeta\zeta} + FF''_{\zeta\zeta} - \left(\frac{2}{2+\gamma}\right)(F'_\zeta)^2 = 0, \tag{A.0.8}$$

which is solved subject to

$$F(\zeta = 0) = 0, \quad F'_\zeta(\zeta = 0) = 1, \quad F'_\zeta(\zeta \to \infty) \to 0, \tag{A.0.9}$$

where we note that (A.0.8) admits analytical solutions for the two cases $\gamma = 0$ and $\gamma = -4$, see Hanevy *et al.* (2024). By introducing a non-constant velocity, we can analyse a broader range of boundary layer flows, making the results applicable to various industrial processes.

Appendix B

External Free Stream

We now analyse the inviscid flow outside the boundary layer for cases where an external oncoming flow interacts with a fixed rough plate. This analysis aims to determine the appropriate matching condition between the boundary layer flow and the inviscid outer flow. The system (2.1.1) is solved with the wall conditions $(u^*, v^*) \cdot \hat{\mathbf{n}} = (u^*, v^*) \cdot \hat{\mathbf{t}} = 0$, which ensure no penetration and no slip along the surface. Recall the following equations:

$$
\begin{aligned}
\frac{\partial u^*}{\partial X^*} + \frac{\partial \tilde{v}^*}{\partial Y^*} &= 0, \\
u^* \frac{\partial u^*}{\partial X^*} + \tilde{v}^* \frac{\partial u^*}{\partial Y^*} &= -\frac{1}{\rho^*} \frac{\partial p^*}{\partial X^*} + \nu^* \mathscr{L}_1^* u^* + \frac{(s^*)'_X}{\rho^*} \frac{\partial p^*}{\partial Y^*}, \\
u^* \frac{\partial \tilde{v}^*}{\partial X^*} + \tilde{v}^* \frac{\partial \tilde{v}^*}{\partial Y^*} + (s^*)''_{X^*X^*} u^{*2} &= -\frac{(1 + (s^*)'^2_{X^*})}{\rho^*} \frac{\partial p^*}{\partial Y^*} + \nu^* \mathscr{L}_1^* \tilde{v}^* + \frac{(s^*)'_{X^*}}{\rho^*} \frac{\partial p^*}{\partial X^*} + \nu^* \mathscr{L}_2^* u^*,
\end{aligned}
$$

where

$$
\begin{aligned}
\mathscr{L}_1^* &= \frac{\partial^2}{\partial X^{*2}} - (s^*)''_{X^*X^*} \frac{\partial}{\partial Y^*} - 2(s^*)'_{X^*} \frac{\partial^2}{\partial X^* \partial Y^*} + (1 + (s^*)'^2_{X^*}) \frac{\partial}{\partial Y^{*2}}, \\
\mathscr{L}_2^* &= 2(s^*)''_{X^*X^*} \left(\frac{\partial}{\partial X^*} - (s^*)'_{X^*} \frac{\partial}{\partial Y^*} \right) + (s^*)'''_{X^*X^*X^*}.
\end{aligned}
$$

The problem is non-dimensionalised by introducing the following scalings

$$(X,Y,s) = \frac{(X^*,Y^*,s^*)}{L^*}, \quad (u,\tilde{v}) = \frac{(u^*,\tilde{v}^*)}{U_\infty^*}, \quad p = \frac{p^*}{\rho^* U_\infty^{*2}},$$

where in this instance U_∞^* is the external free stream velocity. Therefore we obtain

$$\begin{aligned}
\frac{\partial u}{\partial X} + \frac{\partial v}{\partial Y} &= 0, \\
u\frac{\partial u}{\partial X} + v\frac{\partial u}{\partial Y} &= -\frac{\partial p}{\partial X} + \frac{1}{Re}\mathscr{L}_1 u + s'_X\frac{\partial p}{\partial Y}, \\
u\frac{\partial v}{\partial X} + v\frac{\partial v}{\partial Y} + (s)''_{XX}u^2 &= -(1+(s)'^2_X)\frac{\partial p}{\partial Y} + \frac{1}{Re}\mathscr{L}_1 v + s'_X\frac{\partial p}{\partial X} + \frac{1}{Re}\mathscr{L}_2 u.
\end{aligned}$$

To examine the potential flow solution outside the boundary layer in the presence of the wavy surface, we consider the limit as $Re \to \infty$. In this limit, the inviscid flow approximation applies, yielding:

$$\begin{aligned}
\frac{\partial u}{\partial X} + \frac{\partial v}{\partial Y} &= 0, \\
u\frac{\partial u}{\partial X} + v\frac{\partial u}{\partial Y} &= -\frac{\partial p}{\partial X} + s'_X\frac{\partial p}{\partial Y}, \\
u\frac{\partial v}{\partial X} + v\frac{\partial v}{\partial Y} + (s)''_{XX}u^2 &= -(1+(s)'^2_X)\frac{\partial p}{\partial Y} + s'_X\frac{\partial p}{\partial X}.
\end{aligned}$$

Introducing the streamfunction, $u = \partial\psi/\partial Y$, $v = -\partial\psi/\partial X$ and writing the partial derivatives as subscripts the continuity equation is automatically satisfied and we obtain

$$\psi_Y\psi_{XY} - \psi_X\psi_{YY} = -p_X + s'_X p_Y$$

$$-\psi_Y\psi_{XX} + \psi_X\psi_{XY} + s''_{XX}(\psi_Y)^2 = -(1+(s'_X)^2)p_Y + s'_X p_X.$$

For small $a \ll 1$ we can wite ψ and p like so

$$q(x,y) = q^0(x,y) + aq^1(x,y),$$

where s is $\mathcal{O}(a)$. At $\mathcal{O}(1)$ we have that

$$-\psi_Y^0\psi_{XX}^0 + \psi_X^0\psi_{XY}^0 = -p_Y^0, \tag{B.0.1a}$$
$$\psi_Y^0\psi_{XY}^0 - \psi_X^0\psi_{YY}^0 = -p_X^0. \tag{B.0.1b}$$

At $\mathcal{O}(a)$ we have that

$$-\psi_Y^0\psi_{XX}^1 - \psi_Y^1\psi_{XX}^0 + \psi_X^0\psi_{XY}^1 + \psi_X^1\psi_{XY}^0 + (s_{XX}^1)^2(\psi_Y^0)^2 = -p_Y^1 + s_X^1 p_X^0, \tag{B.0.2a}$$
$$\psi_Y^0\psi_{XY}^1 + \psi_Y^1\psi_{XY}^0 - \psi_X^0\psi_{YY}^1 - \psi_X^1\psi_{YY}^0 = -p_X^1 + s_X^1 p_Y^0. \tag{B.0.2b}$$

The derivative of (B.0.1a) with respect to X minus the derivative of (B.0.1b) with respect to Y yields

$$\psi_X^0(\psi_{XX}^0 + \psi_{YY}^0)_Y - \psi_Y^0(\psi_{XX}^0 + \psi_{YY}^0)_X = 0. \tag{B.0.3}$$

Now the boundary conditions are given by

$$u(Y=0) = v(Y=0), \quad u(Y \to \infty) \to 1.$$

Therefore

$$-\psi_X^0(Y=0) = 0, \quad \psi_Y^0(y \to \infty) \to 1.$$

Notice (B.0.3) is satisfied when $\psi_{XX}^0 + \psi_{YY}^0 = c$, so we try $\psi^0 = aX + bY$ which implies that

$$\psi_{XX}^0 + \psi_{YY}^0 = 0. \tag{B.0.4}$$

We notice that $\psi_X^0 = a$, however we need $\psi_X^0(Y=0) = 0$ which implies $a = 0$. Also $\psi_Y^0 = b$, but we require $\psi_Y^0(Y \to \infty) \to 1$, therefore $b = 1$ and thus

$$\psi^0 = Y. \tag{B.0.5}$$

Given the above it is easy to see that $p_Y^0 = p_X^0 = 0$ which implies that p^0 is constant. Equations (B.0.2a) and (B.0.2b) now become

$$-\psi_{XX}^1 + s_{XX}^1 = -p_Y^1, \tag{B.0.6a}$$

$$\psi_{XY}^1 = -p_X^1. \tag{B.0.6b}$$

Differentiating (B.0.6b) with respect Y minus the derivative of (B.0.6a) with respect to X yields

$$\psi_{XYY}^1 + \psi_{XXX}^1 - s_{XXX}^1 = 0. \tag{B.0.7}$$

We solve (B.0.7) via the Fourier transform where

$$\mathcal{F}(\psi(X)) = \int_{-\infty}^{\infty} \psi(X) e^{-\mathrm{i}tX}\,\mathrm{d}X = \hat{\psi}(t),$$
$$\mathcal{F}^{-1}(\hat{\psi}(t)) = \frac{1}{2\pi}\int_{-\infty}^{\infty} \hat{\psi}(t) e^{\mathrm{i}tX}\,\mathrm{d}t = \psi(X).$$

Notice that $\mathcal{F}(\psi_X) = \mathrm{i}t\mathcal{F}(\psi)$. Taking the Fourier transform of (B.0.7) gives

$$\hat{\psi}_{YY}^1 - t^2\hat{\psi}^1 = -t^2\hat{s}, \tag{B.0.8}$$

where the solution is given by

$$\hat{\psi}^1 = \hat{s} + A(t)e^{|t|Y} + B(t)e^{-|t|Y}. \tag{B.0.9}$$

Taking the Fourier transform of $\psi^1_X(Y=0)=0$ yields $\hat{\psi}^1(Y=0)=0$ therefore

$$\hat{s}+A(t)+B(t)=0. \tag{B.0.10}$$

Taking the Fourier transform of $\psi^1_Y(Y\to\infty)\to 0$ yields $\hat{\psi}^1_Y(Y\to\infty)\to 0$ therefore

$$A(t)|t|e^{|t|Y}-B(t)|t|e^{-|t|Y}\to 0, \tag{B.0.11}$$

as $Y\to\infty$. It must be the case that $A(t)=0$. Therefore it is easy to see that

$$\hat{\psi}^1=\hat{s}-\hat{s}e^{-|t|Y}. \tag{B.0.12}$$

Taking the inverse Fourier transform of the above gives

$$\psi^1(X,Y)=\mathcal{F}^{-1}(\hat{\psi}^1)=\mathcal{F}^{-1}(\hat{s}-\hat{s}e^{-|t|Y}),$$

which yields

$$\begin{aligned}
\psi^1(X,Y)&=s(X)-\mathcal{F}^{-1}(\hat{s}e^{-|t|Y})\\
&=s(X)-\frac{1}{2\pi}\int_{-\infty}^{\infty}\hat{s}(t)e^{-|t|Y}e^{\mathrm{i}tX}\mathrm{d}t\\
&=s(X)-\frac{1}{2\pi}\int_{-\infty}^{\infty}\left(\int_{-\infty}^{\infty}s(\tilde{X})e^{-\mathrm{i}t\tilde{X}}\,\mathrm{d}\tilde{X}\right)e^{-|t|Y}e^{\mathrm{i}tX}\,\mathrm{d}t\\
&=s(X)-\frac{1}{2\pi}\int_{-\infty}^{\infty}s(\tilde{X})\left(\int_{-\infty}^{\infty}e^{-\mathrm{i}t\tilde{X}-|t|Y+\mathrm{i}tX}\,\mathrm{d}t\right)\mathrm{d}\tilde{X}.
\end{aligned}$$

Now

$$\int_{-\infty}^{\infty}e^{-\mathrm{i}t\tilde{X}-|t|Y+\mathrm{i}tX}\,\mathrm{d}t=\frac{2Y}{Y^2+(X-\tilde{X})^2}$$

Therefore

$$\psi^1(X,Y) = s(X) - \frac{1}{2\pi}\int_{-\infty}^{\infty} s(\tilde{X})\frac{2Y}{Y^2+(X-\tilde{X})^2}\,\mathrm{d}\tilde{X}. \tag{B.0.13}$$

Therefore ψ is given by

$$\psi(X,Y) = Y + a\left[s(X) - \frac{1}{2\pi}\int_{-\infty}^{\infty} s(\tilde{X})\frac{2Y}{Y^2+(X-\tilde{X})^2}\,\mathrm{d}\tilde{X}\right]. \tag{B.0.14}$$

Now the X component of the inviscid velocity is given by $u = \partial\psi/\partial Y$ which yields

$$U_0(X) = 1 + a\left[-\frac{1}{2\pi}\int_{-\infty}^{\infty} s(\tilde{X})\left(\frac{2}{Y^2+(X-\tilde{X})^2} - \frac{4Y^2}{(Y^2+(X-\tilde{X})^2)^2}\right)\mathrm{d}\tilde{X}\right].$$

To obtain the velocity at the surface we take the limit as $Y \to 0$ therefore

$$U_0(X) = 1 + a\left[-\frac{1}{\pi}\int_{-\infty}^{\infty}\frac{s(\tilde{X})}{(X-\tilde{X})^2}\,\mathrm{d}\tilde{X}\right].$$

Since $s(X) = 0$ for $X < 0$ we have that

$$U_0(X) = 1 + a\left[-\frac{1}{\pi}\int_{0}^{\infty}\frac{s(\tilde{X})}{(X-\tilde{X})^2}\,\mathrm{d}\tilde{X}\right].$$

Integrating by parts yields

$$U_0(X) = 1 + a\left[\frac{s(0)}{\pi X} + \frac{1}{\pi}\int_{0}^{\infty}\frac{s_{\tilde{X}}(\tilde{X})}{\tilde{X}-X}\,\mathrm{d}\tilde{X}\right].$$

The above analysis is valid for any function $s(X)$ for which $s(0) = s'_X(0) = 0$ as per Ghosh Moulic & Yao (1989) therefore

$$U_0(X) = 1 + a\left[\frac{1}{\pi}\int_{0}^{\infty}\frac{s_{\tilde{X}}(\tilde{X})}{\tilde{X}-X}\,\mathrm{d}\tilde{X}\right]. \tag{B.0.15}$$

This matching condition accounts for the adjustment to the inviscid flow velocity caused by the presence of a wavy surface. When the surface is flat, the integral term vanishes, resulting in $U_0 = 1$, which corresponds to the uniform free stream velocity. This condition ensures a consistent transition between the boundary layer flow and the inviscid outer flow. In the context of boundary layer analysis, the streamwise velocity $U_0(X)$ serves as the outer boundary condition for solving the boundary layer equations. The integral term captures the effect of surface roughness on the mean flow, providing a means to analyse how variations in the surface profile influence the boundary layer characteristics. This approach ensures that the viscous flow within the boundary layer matches smoothly with the inviscid flow outside, accurately reflecting the impact of surface roughness on the overall flow behavior.

Appendix C

The Square Wave

We begin by analysing the averaged flow solutions for various values of the roughness parameter where the surface is now described by the function (7.0.1). Once again we truncate the domain at the location $\xi = 1.5$ given that the base flow is doubly periodic with a period equal to 2. In this case we capture one complete cycle of periodicity between $\xi_0 = 0.5$ and $\xi_1 = 1.5$. Similar to the discussions in Chapter 3 the base flow becomes periodic at a suitable distance downstream from the point $\xi = 0$. Therefore we take an ensemble average of the base flow quantities at equally spaced locations between ξ_0 and ξ_1. The solutions are presented below.

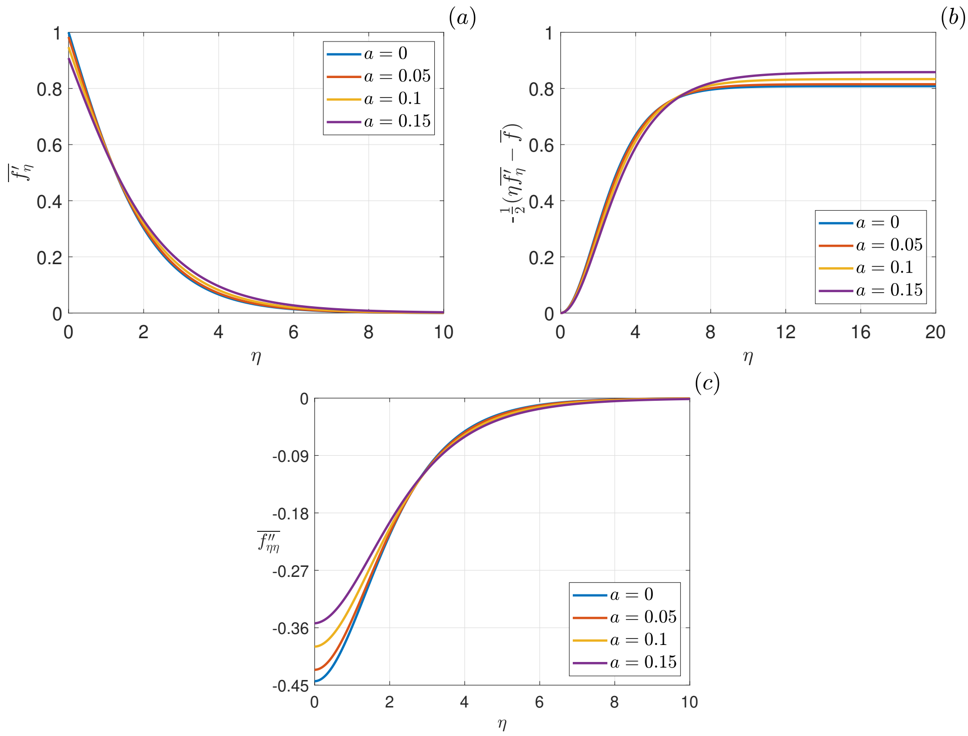

Figure C.1: In (a) and (b) we illustrate the averaged streamwise and scaled wall-normal velocity profiles, respectively, for a range of values of the roughness parameter. In (c) we illustrate the variation of the averaged shear profiles with the boundary-layer coordinate for the same range of values of a.

From the above Figure we observe that an increase in the roughness parameter leads to a decrease in the streamwise velocity component. Again we observe that the flow converges to the free-stream further from the wall indicating the boundary layer has thickened in the presence of surface roughness. We also illustrate the scaled wall-normal velocity $\sqrt{\xi}v_0$, and upon increasing a we find that the constant large-η value of this flow component increases in value. Finally we observe that the absolute value of the shear at the wall decreases in the presence of increasing levels of surface roughness where the results are summarized below.

Table C.1: Numerical values of the basic flow parameters for a range of values of the roughness parameter a.

a	$\overline{f'_\eta}(0)$	$\lvert\overline{f''_{\eta\eta}}(0)\rvert$	$\overline{\delta}$
0	1	0.4437	1.6161
0.05	0.9833	0.4259	1.6300
0.1	0.9471	0.3896	1.6664
0.15	0.9081	0.3530	1.7238

We now analyse the linear stability by solving (4.1.7) subject the conditions (4.1.9). In Figure C.2 we present the growth rates for a range of values of the roughness parameter a at a fixed Reynolds number $R = R_{crit} + 1000$. We find that the amplitude of the growth rate is significantly reduced which suggests stabilisation. We also observe that the area encompassed by the neutral curve is reduced upon increasing stabilisation where the results are summarised below, see Table C.2.

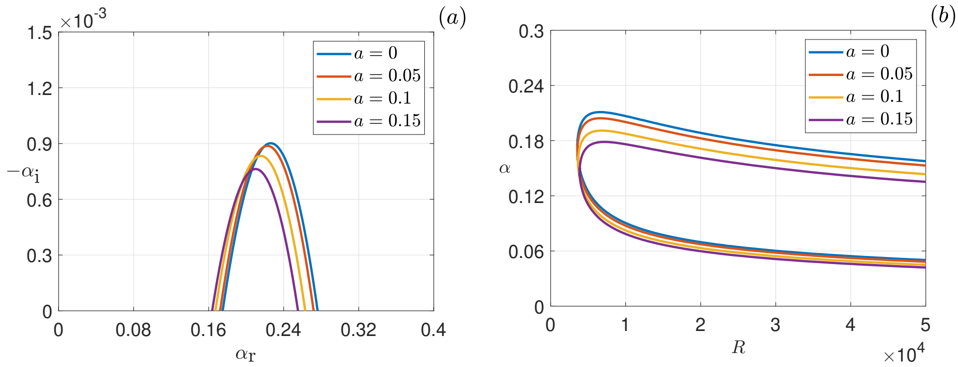

Figure C.2: In (a) the growth rate, defined as $-\alpha_{\mathrm{i}}$, is illustrated against α_{r} for a range of values of the roughness parameter a at a fixed value of the Reynolds number $R = R_{\mathrm{crit}} + 1000$. In (b) the curves of neutral stability, all the points where $\alpha_{\mathrm{i}} = 0$, are illustrated for a range of values of the roughness parameter a.

Table C.2: Critical values for the onset of linear instability for various values of the roughness parameter.

a	R_{crit}	α_{crit}	ω_{crit}
0	3564.01	0.2367	0.1736
0.05	3568.46	0.2330	0.1680
0.1	3666.91	0.2254	0.1569
0.15	3874.13	0.2190	0.1467

We now present the lower branch asymptotics for selected values of the roughness parameter, see Figure C.3. Once again we observe excellent agreement with the two sets of solutions. To conclude, we have shown that if the roughness is modeled by (7.0.1) then again we delay the onset of linear instability. Although we have not complimented the analysis with the quasi-spatial approach, we are confident, given the results presented here, that conducting a quasi-spatial approach would lead to qualitatively similar behaviour.

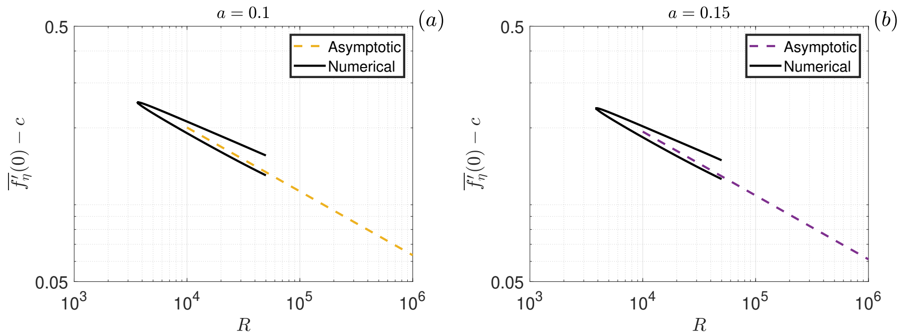

Figure C.3: In (a) a comparison between the asymptotic and numerical results in the case when $a = 0.1$. In (b) a comparison between the asymptotic and numerical results in the case when $a = 0.15$. Comparing the asymptotic and numerical results for (a) $a = 0.1$ and (b) $a = 0.15$. The large Reynolds number asymptotic solution is given by the dashed curve.

List of References

ABDELHAFEZ, TALAT A 1985 Skin friction and heat transfer on a continuous flat surface moving in a parallel free stream. *International Journal of Heat and Mass Transfer* **28** (6), 1234–1237.

ABROMOWITZ, MILTON & STEGUN, IRENE A 1972 Handbook of mathematical functions.

ALVEROGLU, BURHAN, SEGALINI, ANTONIO & GARRETT, STEPHEN J 2016 The effect of surface roughness on the convective instability of the bek family of boundary-layer flows. *European Journal of Mechanics-B/Fluids* **56**, 178–187.

APPELQUIST, ELLINOR & IMAYAMA, SHINTARO 2017 Revisiting the stability analysis of the flow over a rotating disk. *Tech. Rep.*. KTH, School of Engineering Sciences (SCI), Centres, Linné Flow Center, FLOW.

BERTOLOTTI, FABIO P, HERBERT, TH & SPALART, PR 1992 Linear and nonlinear stability of the blasius boundary layer. *Journal of fluid mechanics* **242**, 441–474.

BLASIUS, HEINRICH 1907 *Grenzschichten in Flüssigkeiten mit kleiner Reibung*. Druck von BG Teubner.

CARDILLO, JAMES, CHEN, YI, ARAYA, GUILLERMO, NEWMAN, JENSEN, JANSEN, KENNETH & CASTILLO, LUCIANO 2013 Dns of a turbulent boundary layer with surface roughness. *Journal of Fluid Mechanics* **729**, 603–637.

CARPENTER, PETER 1997 The right sort of roughness. *Nature* **388** (6644), 713–714.

CHOI, KWING-SO 2006 The rough with the smooth. *Nature* **440** (7085), 754–754.

COOPER, A. J., HARRIS, J. H., GARRETT, S. J., ÖZKAN, M. & THOMAS, P. J. 2015 The effect of anisotropic and isotropic roughness on the convective stability of the rotating disk boundary layer. *Phys. Fluids* **27**, 014107.

DRAZIN, PHILIP G & REID, WILLIAM HILL 2004 *Hydrodynamic stability*. Cambridge university press.

ELBASHBESHY, EMA & BAZID, MAA 2004 The effect of temperature-dependent viscosity on heat transfer over a continuous moving surface with variable internal heat generation. *Applied mathematics and computation* **153** (3), 721–731.

ERICKSON, LE, FAN, LT & FOX, VG 1966 Heat and mass transfer on moving continuous flat plate with suction or injection. *Industrial & Engineering Chemistry Fundamentals* **5** (1), 19–25.

FLORYAN, JERZY M & SARIC, WILLIAM S 1982 Stability of gortler vortices in boundary layers. *AIAA journal* **20** (3), 316–324.

GARRETT, STEPHEN J, COOPER, AJ, HARRIS, JH, ÖZKAN, M, SEGALINI, ANTONIO & THOMAS, PJ 2016 On the stability of von kármán rotating-disk boundary layers with radial anisotropic surface roughness. *Physics of Fluids* **28** (1).

GASTER, MICHAEL 2016 Understanding the effects of surface roughness on the growth of disturbances. In *46th AIAA Fluid Dynamics Conference*, p. 4384.

GHOSH MOULIC, SANDIPAN & YAO, LS 1989 Mixed convection along a wavy surface. *J. Heat Transfer* .

GRIFFITHS, PT, STEPHEN, SO & KHAN, MAIR 2021 Stability of the flow due to a linear stretching sheet. *Physics of Fluids* **33** (8).

HALL, PHILIP 1986 An asymptotic investigation of the stationary modes of instability of the boundary layer on a rotating disc. *Proceedings of the Royal Society of London. A. Mathematical and Physical Sciences* **406** (1830), 93–106.

HANEVY, N, FERGUSON, J, TREVELYAN, P. M. J. & GRIFFITHS, P. T. 2024 Boundary-layer flows over deforming surfaces. *Physical Review Fluids* **9** (5), 054101.

HARRIS, JOSEPH H 2013 Stability of the flow over a rough, rotating disk. PhD thesis, University of Warwick.

HATTORI, YUNA 2023 Numerical simulations of sakiadis boundary-layer flow. *Physics of Fluids* **35** (12).

HEALEY, JJ 1995 On the neutral curve of the flat-plate boundary layer: comparison between experiment, orr–sommerfeld theory and asymptotic theory. *Journal of Fluid Mechanics* **288**, 59–73.

HOSSAIN, MA & POP, I 1996 Magnetohydrodynamic boundary layer flow and heat transfer on a continuous moving wavy surface. *Archives of Mechanics* **48** (5), 813–823.

ISHAK, ANUAR, YACOB, NOR AZIZAH & BACHOK, NORFIFAH 2011 Radiation effects on the thermal boundary layer flow over a moving plate with convective boundary condition. *Meccanica* **46**, 795–801.

KACHANOV, Y. S., KOZLOV, V. V. & LEVCHENKO, V. Y. 1974 Experimental study of laminar-boundary-layer stability on a wavy surface. *Izv. Sib. Otd. Akad. Nauk SSSR, Ser. Tekh. Nauk* **13** (3), 2–6.

KELLER, HERBERT B 1978 Numerical methods in boundary-layer theory. *Annual Review of Fluid Mechanics* **10** (1), 417–433.

LE PALEC, G, NARDIN, PH & RONDOT, D 1990 Study of laminar heat transfer over a sinusoidal-shaped rotating disk. *International journal of heat and mass transfer* **33** (6), 1183–1192.

LESSEN, MARTIN & GANGWANI, SANTU T 1976 Effect of small amplitude wall waviness upon the stability of the laminar boundary layer. *The Physics of Fluids* **19** (4), 510–513.

LEVCHENKO, V. Y. & SOLOV'EV, A. S. 1972 Boundary layer stability on a wave-periodic surface. *Fluid Dynamics* **7** (6), 884–888.

LIN, HSIAO-TSUNG & HUANG, SHIH-FENG 1994 Flow and heat transfer of plane surfaces moving in parallel and reversely to the free stream. *International journal of heat and mass transfer* **37** (2), 333–336.

LINGWOOD, R. J. 1995 Absolute instability of the boundary layer on a rotating disk. *J. Fluid Mech.,* **299**, 17–33.

LU, HUI, XU, MINGHAI, GONG, LIANG, DUAN, XINYUE & CHAI, JOHN C 2020 Effects of surface roughness in microchannel with passive heat transfer enhancement structures. *International Journal of Heat and Mass Transfer* **148**, 119070.

LUO, JISHENG & WU, XUESONG 2010 On the linear instability of a finite stokes layer: instantaneous versus floquet modes. *Physics of Fluids* **22** (5).

MALIK, MUJEEB R 1986 The neutral curve for stationary disturbances in rotating-disk flow. *Journal of Fluid Mechanics* **164**, 275–287.

MEHMOOD, AHMER, IQBAL, MUHAMMAD SALEEM, KHAN, SAJID & MUNAWAR, SUFIAN 2019*a* Entropy analysis in moving wavy surface boundary-layer. *Thermal Science* **23** (1), 233–241.

MEHMOOD, AHMER, USMAN, MUHAMMAD & WEIGAND, BERNHARD 2019*b* Heat and mass transfer phenomena due to a rotating non-isothermal wavy disk. *International Journal of Heat and Mass Transfer* **129**, 96–102.

MILLER, ROBERT, GARRETT, STEPHEN J, GRIFFITHS, PAUL T & HUSSAIN, ZAHIR 2018 Stability of the blasius boundary layer over a heated plate in a temperature-dependent viscosity flow. *Physical Review Fluids* **3** (11), 113902.

MORGAN, SCOTT 2018 Stability of periodically modulated rotating disk boundary layers. PhD thesis, Cardiff University.

MORGAN, S. & DAVIES, C. 2020*a* Linear stability eigenmodal analysis for steady and temporally periodic boundary-layer flow configurations using a velocity-vorticity formulation. *J. Comput. Phys.* **409**, 109325.

MORGAN, SCOTT & DAVIES, CHRISTOPHER 2020*b* Linear stability eigenmodal analysis for steady and temporally periodic boundary-layer flow configurations using a velocity-vorticity formulation. *Journal of Computational Physics* **409**, 109325.

MORGAN, S., DAVIES, C. & THOMAS, C. 2021*a* Control of stationary convective instabilities in the rotating disk boundary layer via time-periodic modulation. *J. Fluid Mech.* **925**, A20 1–29.

MORGAN, S., DAVIES, C. & THOMAS, C. 2021*b* Control of stationary convective instabilities in the rotating disk boundary layer via time-periodic modulation. *J. Fluid Mech.,* **925**, A20.

ORR, WILLIAM M'F 1907 The stability or instability of the steady motions of a perfect liquid and of a viscous liquid. part ii: A viscous liquid. In *Proceedings of the Royal Irish Academy. Section A: Mathematical and Physical Sciences*, , vol. 27, pp. 69–138. JSTOR.

ÖZKAN, MUSA, THOMAS, PETER J, COOPER, AJ & GARRETT, STEPHEN JOHN 2017 Comparison of the effects of surface roughness and confinement on rotor–stator cavity flow. *Engineering Applications of Computational Fluid Mechanics* **11** (1), 142–158.

POP, IOAN, GORLA, RAMA SUBBA REDDY & RASHIDI, MAJID 1992 The effect of variable viscosity on flow and heat transfer to a continuous moving flat plate. *International journal of engineering science* **30** (1), 1–6.

POP, I & NAKAMURA, S 1996 Laminar boundary layer flow of power-law fluids over wavy surfaces. *Acta mechanica* **115** (1-4), 55–65.

PRANDTL, LUDWIG 1905 Uber flussigkeitsbewegung bei sehr kleiner reibung. *Verhandl. 3rd Int. Math. Kongr. Heidelberg (1904), Leipzig* .

REES, D ANDREW S & POP, I 1995 Boundary layer flow and heat transfer on a continuous moving wavy surface. *Acta Mechanica* **112** (1-4), 149–158.

REYNOLDS, OSBORNE 1883 Xxix. an experimental investigation of the circumstances which determine whether the motion of water shall be direct or sinuous, and of the law of resistance in parallel channels. *Philosophical Transactions of the Royal society of London* **174**, 935–982.

RUBAN, ANATOLY, GAJJAR, JITESH & WALTON, ANDREW 2023 *Fluid Dynamics: Part 4: Hydrodynamic Stability Theory*. Oxford University Press.

SAKIADIS, BYRON C 1961*a* Boundary-layer behavior on continuous solid surfaces: I. boundary-layer equations for two-dimensional and axisymmetric flow. *AIChE Journal* **7** (1), 26–28.

SAKIADIS, BYRON C 1961*b* Boundary-layer behavior on continuous solid surfaces: Ii. the boundary layer on a continuous flat surface. *AiChE journal* **7** (2), 221–225.

SCHLICHTING, L 1933 Zur kntstehung der turbulenz bei der platten-stromung, nachrichten von der gesellschaft der wipgiˆ chaften zu ciotiingen. *Mathemiitisch-Physikalische Klasse* **1933**, 181–208.

SCHMID, P. J. & HENNINGSON, D. S. 2001 *Stability and transition in shear flows*. Berlin, Germany: Springer.

SCHUBAUER, GB & SKRAMSTAD, HK 1948 Naca rep. no. 909. *JOURNAL OF THE AERONAUTICAL SCIENCES* **14**.

SMITH, FRANK THOMAS 1979 On the non-parallel flow stability of the blasius boundary layer. *Proceedings of the Royal Society of London. A. Mathematical and Physical Sciences* **366** (1724), 91–109.

SOMMERFIELD, ARNOLD 1908 Ein beitrag zur hydrodynamischen erklarung der turbulenten flussigkeisbewegung. *Atti Congr. Int. Math. 4th* .

SOUNDALGEKAR, VM & MURTY, TV RAMANA 1989 Viscous dissipation effects on heat transfer in flow past a continuous moving plate. *Bull. Cal. Math. Soc.* **81**, 232–234.

SOUNDALGEKAR, VM & RAMANA MURTY, TV 1980 Heat transfer in flow past a continuous moving plate with variable temperature. *WaÈrme-und stoffuÈbertragung* **14** (2), 91–93.

SOUNDALGEKAR, VM, TAKHAR, HARMINDAR S, DAS, UN, DEKA, RUDRA K & SARMAH, A 2004 Effect of variable viscosity on boundary layer flow along a continuously moving plate with variable surface temperature. *Heat and Mass transfer* **40**, 421–424.

THEOFILIS, VASSILIOS 2003 Advances in global linear instability analysis of nonparallel and three-dimensional flows. *Progress in aerospace sciences* **39** (4), 249–315.

THOMAS, C., ALVEROĞLU, B., STEPHEN, S. O., AL-MALKI, M. A. S. & HUSSAIN, Z. 2023 Effect of slip on the linear stability of the rotating disk boundary layer. *Phys. Fluids* **35**, 084118.

TOLLMIEN, WALTER 1930 Über die entstehung der turbulenz. *Vorträge aus dem Gebiete der Aerodynamik und verwandter Gebiete: Aachen 1929* pp. 18–21.

TSOU, FK, SPARROW, EPHRAIM M & GOLDSTEIN, R JH 1967 Flow and heat transfer in the boundary layer on a continuous moving surface. *International Journal of Heat and Mass Transfer* **10** (2), 219–235.

TSOU, FK, SPARROW, EPHRAIM M & KURTZ, EF 1966 Hydrodynamic stability of the boundary layer on a continuous moving surface. *Journal of Fluid Mechanics* **26** (1), 145–161.

WATANABE, T, POP, I & GOTO, F 1995 Mhd stability of boundary layer flow over a moving flat plate. *Technische Mechanik-European Journal of Engineering Mechanics* **15** (4), 325–332.

WIE, YONG-SUN & MALIK, MUJEEB R 1998 Effect of surface waviness on boundary-layer transition in two-dimensional flow. *Computers & fluids* **27** (2), 157–181.

WU, WEN & PIOMELLI, UGO 2018 Effects of surface roughness on a separating turbulent boundary layer. *Journal of Fluid Mechanics* **841**, 552–580.

YAO, LS 1988 A note on prandtl's tranposition theorem. *Journal of Heat Transfer (Transcations of the ASME (American Society of Mechanical Engineers), Series C);(United States)* **110** (2).

YOON, M. S., HYUN, J. M. & PARK, J. S. 2007 Flow and heat transfer over a rotating disk with surface roughness. *Int. J. Heat Fluid Flow* **28**, 262–267.